Final version published as: Thiessen, E. J., Gibson, H. D., Regis, D., Pehrsson, S. J., Ashley, K. T., & Smit, M. A. (2020). The distinct metamorphic stages and structural styles of the 1.94–1.86 Ga Snowbird Orogen, Northwest Territories, Canada. Journal of Metamorphic Geology, 38(9), 963–992. https://doi.org/10.1111/jmg.12556.

The distinct metamorphic stages and structural styles of the 1.94 to 1.86 Ga Snowbird Orogen, Northwest Territories, Canada

[1]Thiessen, E.J., [1]Gibson, H.D., [2]Regis, D., [2]Pehrsson, S.J., [3]Ashley, K.T., and [4]Smit, M.A.

[1]Department of Earth Sciences, Simon Fraser University, 8888 University Drive, Burnaby, British Columbia, V5A 1S6, Canada, ericjamesthiessen@gmail.com
[2]Geological Survey of Canada, 601 Booth Street, Ottawa, Ontario, K1A 0E8, Canada
[3]Department of Geology and Environmental Science, University of Pittsburgh, 4107 O'Hara Street, Pittsburgh, Pennsylvania, United States
[4]Department of Earth, Ocean, and Atmospheric Sciences, University of British Columbia, 2020 2207 Main Mall, Vancouver, British Columbia V6T 1Z4, Canada

KEYWORDS

Lu-Hf garnet, Petrochronology, Zr in rutile and titanite thermometry, solid inclusion barometry, Snowbird tectonic zone

ABSTRACT

Paleoproterozoic orogenesis within the Archean southeastern Rae craton is related to the initial amalgamation of Laurentia. Characterizing the accompanying tectonic processes during this time has been complicated due to polymetamorphism, which results in the obscuring of the age record of the terranes involved. To improve the knowledge of the tectonic evolution of the South Rae Craton, petrologic and structural analyses are applied in conjunction with *in situ* trace element chemistry, inclusion barometry, U-Pb monazite and titanite, and Lu-Hf garnet chronology. The data robustly constrain Paleoproterozoic pressure-temperature-time paths of major deformational events along the southeastern Rae craton margin. D_1 occurred between 1.94 and 1.93 Ga in the Dodge-Snowbird domain, which included prograde burial of metasedimentary rocks, deposited at 2.2 to 2.0 Ga, and the development of migmatitic layering and east-southeast trending folds (S_1, F_1). Peak metamorphism is recorded in metasedimentary units at c. 1.93 Ga when rocks reached conditions of 9.0–10.5 kbar and 810–830 °C. Within the Dodge-Snowbird domain, D_2 imparted north-northeast trending open folds and associated axial planar cleavage (S_2, F_2) between 1.93 and 1.90 Ga during east-west compression that appears to have been synchronous with cooling and exhumation. Later D_2 deformation, localized within

the Wholdaia Lake shear zone (S_{T1}), developed in the footwall of this thrust-sense structure at 1873 ± 5 Ma at conditions of 9.5–11.0 kbar and 820–850 °C. The hanging wall Dodge-Snowbird domain had already cooled to below 300 °C by then, indicating a significant structural and metamorphic break across the domain's western boundary. A new phase of unroofing (D_3) involved pervasive amphibolite- to greenschist-facies extensional shearing (S_{T2}) within the Wholdaia Lake shear zone, which overprinted S_{T1} foliations between 1.87 and 1.86 Ga. Continued greenschist-facies shearing younger than 1.86 Ga likely ended by c. 1.83 Ga when lamprophyre dykes cut the structure, which was followed by cooling until c. 1.80 Ga. This work highlights the utility and application of multiple chronometers (zircon, monazite, titanite, garnet) along with structural and petrologic analysis that together can resolve precise orogenic cycles in polymetamorphic terranes that may otherwise be undetected. The time-resolved P-T-D histories derived here enable more robust interpretations regarding the nature and evolution of 1.9 Ga tectonism along the southeast Rae craton margin, which may be used to refine models for Laurentian terrane amalgamation.

1 INTRODUCTION

The Archean South Rae craton's polymetamorphic history is complicated and details of its Paleoproterozoic orogenic history during Laurentia's amalgamation are still lacking. Detailed modern analyses on the tectonic zones that bound this craton are needed to overcome this issue. One such example is the eastern flank of the South Rae craton (Figure 1), which is bounded by the c. 1000 km-long central segment of the Snowbird Tectonic Zone — a large mobile belt that preserves segments of highly-deformed amphibolite, granulite and eclogite-facies rocks dated at 2.5 and 1.9 Ga (e.g., Baldwin, Bowring, Williams, & Williams, 2004; Dumond, Williams, Baldwin, & Jercinovic, 2017; Mahan,

Goncalves, Flowers, Williams, & Hoffman-Setka, 2008; Martel, van Breeman, Berman, & Pehrsson, 2008; Regan et al., 2014; Thiessen et al., 2019). Paleoproterozoic crustal thickening and loading of this margin was demonstrated with the identification of metasedimentary units that were deposited at 2.2 to 2.0 Ga on exhumed high-grade Archean basement and subsequently buried to 6–8 kbar at 840 °C between 1.94 and 1.90 Ga (e.g., Ashton, Hartlaub, Bethune, Heaman, & Niebergail, 2013; Ashton, Knox, Bethune, & Rayner, 2007b; Martel et al., 2008; Shiels, Partin, & Eglington, 2016; Thiessen, Gibson, Regis, & Pehrsson, 2018). Following peak metamorphism, deformation on multiple crustal-scale shear zones operated episodically between 1.9 and 1.8 Ga (Dumond, McLean, Williams, Jercinovic, & Bowring, 2008; Mahan, Williams, & Baldwin, 2003; Mahan, Goncalves, Williams, & Jercinovic, 2006a; Regan et al., 2014; Thiessen et al., 2018), which accommodated regional exhumation and attendant cooling. In spite of these insights, the nature of orogenesis associated with the 1.9 Ga high-grade event is debated and models still include a range of options, from far-field stress and mafic underplating promoting intracontinental reworking (e.g., Mahan et al., 2008; Regan et al., 2014) to convergent margin processes (Berman, Davis, & Pehrsson, 2007; Hoffman, 1988; Martel et al., 2008).

Constraining the tectonic processes involved in the 1.9 Ga metamorphism, as well as older processes in the region requires age estimates for the resulting high-grade assemblages and corresponding structures. However, complications arise because the dehydrated Neoarchean basement rocks generally preserve an incomplete, or absent, pressure-temperature-time-deformation (P-T-t-D) record related to younger Paleoproterozoic reworking (e.g., Mahan et al., 2006a, 2006b; Dumond et al., 2008, 2017). However, this 1.9 Ga history is more reliably recorded in the hydrated young supracrustal sedimentary rocks (e.g., Bethune, Berman, Rayner, & Ashton, 2013).

Accordingly, in this study we apply an integrated multi-method chronological approach to two 2.2 to 2.0 Ga metasedimentary rocks and a Neoarchean mafic granulite. The results are used to constrain

the P-T-t histories of multiple deformation (D) episodes that provide a clearer picture of the metamorphic (prograde burial to exhumation) and structural evolution along the southeastern Rae craton margin between 1.94 and 1.86 Ga. To allow age determinations to be confidently linked to P-T conditions and deformation episodes, we combine geochronology (*in situ* U-Pb monazite and titanite, Lu-Hf garnet), with documented field relationships and microstructures, as well as results from thermobarometry (isochemical phase diagram analysis, quartz and apatite in garnet barometry, Ti in zircon and Zr in titanite and rutile thermometry). These data, combined with those from previous studies along the southeast Rae craton margin, provide insight into the regional trends in P-T-t-D relationships, as well as new constraints on the history of Paleoproterozoic orogenesis that involved crustal thickening, exhumation and subsequent orogenic collapse.

2 GEOLOGICAL CONTEXT

2.1 South Rae Craton

The South Rae craton (Figure 1) is dominantly comprised of 2.7 to 2.6 Ga plutonic rocks, as well as ortho- and paragneiss (Davis, Pehrsson, & Percival, 2015, Regis, Martel, Davis, & Pehrsson, 2017b) that have been subjected to multiple tectonic events between 2.7 and 1.8 Ga. The Archean basement was variably reworked or intruded between 2.6 and 2.5 Ga (e.g., Dumond, Goncalves, Williams, & Jercinovic, 2010; Mahan et al., 2008; Martel et al., 2008), 2.5 and 2.2 Ga (Berman et al., 2013a; Hartlaub et al., 2005; Hartlaub, Heaman, Chacko, & Ashton, 2007), 2.11 Ga (Thiessen et al., 2019), and 2.0 and 1.85 Ga (Baldwin et al., 2004; Bethune et al., 2013; Mahan et al., 2006a, 2006b; Martel et al., 2008; McDonough, McNicoll, Schetselaar, & Grover, 2000). Metasedimentary sequences deposited

after c. 2.2 to 2.0 Ga and unconformably overlay Archean basement, are documented along the craton's margins (Figure 1) and were subsequently deformed and metamorphosed together with their basement at c. 1.9 Ga (Martel et al., 2008). Prior to final cratonization, the South Rae was affected by the c. 2.0 to 1.9 Ga Taltson Orogen along its western margin (McDonough et al., 2000) and the c. 1.9 Ga Snowbird Orogen along its eastern margin (Berman et al., 2007), the latter of which is suggested to be an early phase of microcontinent accretion of the Trans-Hudson Orogen (Corrigan, 2012). Additional far-field effects from the collision of the Sask and Superior cratons to the composite Rae-Hearne cratons (Western Churchill Province) occurred between c. 1.87 to 1.80 Ga (Corrigan, 2012).

The South Rae is subdivided into multiple lithotectonic domains (Figure 1) that are distinguished by protolith and metamorphic ages (e.g., Ashton, Rayner, Heaman, & Creaser, 2014; Davis et al., 2015). Several domains were studied independently in Saskatchewan and Northwest Territories. Some have since been determined to have shared affinity (e.g., Ashton et al., 2007b; Davis et al., 2015); within the southeastern Rae craton these include the composite Dodge-Snowbird domain and the Train-Firedrake domain (Figs. 1, 2). Crustal-scale shear zones delineate the boundaries between these domains and were active between 1.9 and 1.8 Ga. Domain bounding structures such as the Legs Lake shear zone (Mahan et al., 2003), Cora Lake shear zone (Regan et al., 2014) and Wholdaia Lake shear zone (WLsz, Thiessen et al., 2018) strike north-northeast (Figure 2) and accommodated exhumation of the high-grade southeast Rae margin between 1.90 to 1.85 Ga. A younger structure that strikes northeast, the Grease River shear zone (Dumond et al., 2008; Lafrance and Sibbald, 1997; Mahan & Williams, 2005), separates the Tantato domain from the Beaverlodge, Train-Firedrake and Dodge-Snowbird domains and dextrally offsets the Chipman domain by ~110 km (Mahan & Williams, 2005). The samples studied here derive from the WLsz and the Dodge-Snowbird domain within its hanging wall.

2.2 The Dodge-Snowbird domain and bounding shear zones

The Dodge-Snowbird domain (Figure 2) consists of Neoarchean ortho- and paragneiss unconformably overlain by, and subsequently infolded with, a 2.2 to 2.0 Ga metasedimentary sequence comprised of pelite, psammite, quartzite, calc-silicate and amphibolite herein called the Snowbird metasediments (Ashton et al., 2017a; Martel et al., 2008; Thiessen et al., 2018). Ages for the Snowbird metasediments (Figure 2a) have been obtained west of Snowbird Lake (1c in Figure 2a, Martel et al., 2008), southeast of Wholdaia Lake (sample 15ET273b of Thiessen et al., 2018), and at Grollier Lake (Ashton et al., 2017a; Ply, 2016). Based on similarity in rock type and maximum depositional ages, these metasediments have been correlated with the upper Murmac Bay Group within the Beaverlodge and eastern Zemlak domains farther west (Figure 1) (Ashton et al., 2013; Bethune et al., 2013; Shiels et al., 2016).

Within the Snowbird metasediments, two deformation events (D_1, D_2) control the regional map pattern, although at least five deformation events are recorded locally (e.g., Knox, Card, & Ashton, 2011). The first structure (S_1, Figures 2a–b) is a regional gneissosity that strikes broadly east-southeast, defined by amphibolite to granulite-facies compositional layering and subparallel leucosome lenses that are axial planar to north-northeast vergent isoclinal recumbent folds (F_1, Knox et al., 2011; Martel et al., 2008; Williams and Jercinovic, 2012). This S_1 fabric is folded by open to tight F_2 folds (Figure 2b) that developed a north-northeast striking, steeply dipping axial planar foliation (S_2). P-T-t-D studies of these structures (samples 1a & 1b in Figure 2a) led Martel et al. (2008) to interpret monazite included in garnet as recording prograde metamorphic conditions at 1921 ± 4 Ma synchronous with development of S_1. Matrix monazite in the samples were interpreted to represent retrograde conditions at 1904 ± 9 Ma coeval with upright north-northeast trending folds (F_2) and axial planar S_2 development. Similarly,

Williams and Jercinovic (2012) analyzed monazite in paragneiss near Snowbird Lake (near sample 1c in Figure 2a) and determined that prograde garnet growth occurred at 1.94 to 1.92 Ga (mostly high-Y crystals) synchronous with S_1, whereas peak metamorphic conditions occurred at 1.90 Ga (mostly low-Y crystals) coeval with S_2.

The Dodge-Snowbird domain is separated from the Train-Firedrake domain to the west by the WLsz (Figure 2a), a 300-km-long, up to 20-km-wide, greenschist- to granulite-facies, crustal-scale shear zone that accommodated extensional exhumation (D_3) between c. 1.90 and 1.86 Ga (Thiessen et al., 2018). Curvilinear magnetic patterns within bounding wall rock domains have been realigned in a dextral sense into the linear patterns of the WLsz (Thiessen et al., 2018). These observations indicate that S_1 and S_2 of the Dodge-Snowbird domain predate the transposed foliations of the WLsz. The shear zone is subdivided into two subdomains (Figures 2b–d) that are inferred to have accommodated dextral, normal-oblique shear; 1) granulite-facies, Grt+Cpx+Opx-bearing (abbreviations according to Whitney and Evans, 2010), mafic and felsic orthogneiss and mylonite that strikes north-northeast and dips southeast ~60° (S_{T1}) and, 2) penetratively transposed, greenschist- to amphibolite-facies, Hbl+Bt-bearing ortho- and paragneiss and mylonite that strikes north-northeast and dips southeast ~85° (S_{T2}) and contains a 10 to 60° southwest-plunging mineral stretching lineation. Although S_{T1} and S_{T2} are described as distinct domains, S_{T2} overprints S_{T1} locally (Thiessen et al., 2018). Segments of the WLsz were reoriented in a clockwise manner (Figure 2a) along structures that contain greenschist-facies mylonite, which are parallel to the Grease River shear zone and are presumably younger than S_{T2} (Thiessen et al., 2018).

The eastern margin of the Dodge-Snowbird domain is bound by the north-northeast striking Striding mylonite belt (Hanmer, Williams, & Kopf, 1995), which consists of highly sheared rocks that progressively transpose S_1 foliations (Figure 2a) with a sinistral sense of shear (Martel et al., 2008).

There has been no systematic study of the Striding mylonite belt to date. However, considering its location on the western margin of the Chipman domain, it may be analogous to the Cora Lake shear zone in Saskatchewan (Figure 2a; Thiessen et al., 2018), which has extension-related, oblique-sinistral shear sense between 1.89 and 1.88 Ga (Regan et al., 2014). The southern Striding mylonite belt and southeast margin of the Dodge-Snowbird domain are truncated by the dextral strike-slip Grease River shear zone (Figure 2a).

2.3 The Beaverlodge, Zemlak and Tantato domains

In the greenschist- to amphibolite-facies west-central Beaverlodge domain, prograde, high-Y monazite growth at 1.94 to 1.93 Ga within the metasedimentary upper Murmac Bay Group is linked to development of east-southeast striking foliation (S_1) and similarly trending folds (Bethune et al., 2013). Identical prograde ages are found in similar granulite-facies rocks in the eastern Beaverlodge domain (Knox, 2012). Three metamorphic zircon crystals from these units yielded c. 1.93 to 1.90 Ga (Ashton, Rayner, & Bethune, 2009; Shiels et al., 2016) and one population from the eastern Beaverlodge domain yielded a more precise date of 1907 ± 5 Ma (Ashton et al., 2007b). These rocks also contain 1.91 to 1.90 Ga monazite associated with stable garnet or cordierite growth after garnet within northeast striking structures (S_2) and are attributed to decompression (Bethune et al., 2013; Knox, 2012). Thus, P-T-t-D data from the upper Murmac Bay Group show prograde metamorphism associated with east-southeast fabric (S_1) development between 1.94 and 1.93 Ga, metamorphic zircon growth at 1.91 Ga and exhumation-related metamorphism associated with northeast trending structures (S_2 & F_2) between 1.91 and 1.90 Ga (Bethune et al., 2013).

Shallow fabrics within the Tantato domain (Figure 2) are roughly parallel to S_1, yet are Archean in age (Dumond et al., 2010). By contrast, folds, axial planar foliations and smaller shear zones that are parallel to S_2 formed at c. 1.90 Ga at 8–12 kbar at 600–900 °C (Dumond, Goncalves, Williams, & Jercinovic, 2015; Flowers, Bowring, Mahan, & Williams, 2006a; Flowers, Bowring, Mahan, Williams, & Williams, 2008; Mahan et al., 2006a, 2008; Regan et al., 2014). Furthermore, in the eastern Tantato domain, the high-strain Cora Lake and Legs Lake shear zones transpose their wall rocks into north-northeast trending gneiss and mylonite belts (Figure 2), which are roughly parallel to the WLsz. The Cora Lake shear zone developed a north-northeast trending and steeply north-west dipping mylonite zone with associated upright folds and axial planar foliations (parallel to S_2) at c. 1.90 Ga and reached conditions of 8-10 kbar and 700–800 °C (Regan et al., 2014). After peak metamorphism, 1.89–1.88 Ga normal-oblique sinistral deformation commenced, which aided exhumation with an extensional component possibly related to D_3.

A similar P-T-t history is documented in the Chipman domain and the Legs Lake shear zone with the exception that thrust-sense rather than normal-sense exhumation is interpreted therein (Mahan et al., 2003, 2006a). Peak P-T conditions of 10–11 kbar and 800–900 °C were followed by decompression (Mahan et al., 2006a, 2008) sometime between 1.94 and 1.88 Ga (Flowers et al., 2006a, 2008; Mahan et al., 2006a) related to thrust-sense, west-over-east movement on the Legs Lake shear zone. Decompression and thrust-sense deformation continued at c. 1.85 Ga as recorded by monazite associated with hydration reactions (Mahan et al., 2006a).

2.4 Geological setting and sample descriptions

Three samples were selected (Figure 2a) to better constrain the P-T-t-D and petrologic history of D_1, D_2, and D_3 in the southeast Rae craton margin through the examination of the WLsz and the Dodge-Snowbird domain. These samples consist of a metasedimentary rock from the western Dodge-Snowbird domain (15ET273b), a mafic granulite gneiss (15ET249b) from the S_{T1} portion of the WLsz and a paragneiss (15ET258b) from the S_{T2} portion of the WLsz. For clarity these samples are given modifiers, which are Sb^{Pg} for the paragneiss within the Dodge-Snowbird domain (15ET273b), $WLsz^{MG}$ for the mafic granulite within the WLsz (15ET249b) and $WLsz^{Pg}$ for the paragneiss within the WLsz.

2.4.1 Paragneiss - Sb^{Pg}

The Sb^{Pg} exhibits a schistose to gneissic texture with leucosome segregations (Figure 3, Thiessen et al., 2018). It contains a prominent foliation that strikes northwest and dips ~30° to the northeast (Figure 2b) and occurs on the limb of a km-scale folded package whose axial trace trends to the north-northeast, parallel to S_2 documented throughout the domain. Restoration of these folds indicates that this foliation had an original east-southeast strike sub-parallel to S_1 foliations (e.g., Martel et al., 2008). The penetrative schistose to gneissic foliation consists of mm- to cm-thick leucocratic quartzo-feldspathic domains alternating with thin (~mm-scale) mesocratic layers (Figure 3a). In thin section these mesocratic domains consist of $Grt+Sil_1+Kfs_1+Qz_1+Bt_1+Rt+Ilm$, whereas the leucocratic segregations are composed of Kfs_1+Qz_1 with lesser $Bt_1+Rt+Ilm$. Garnet porphyroblasts are ~4 mm in diameter (Figures 3b–e); cores (Grt_C) are poikiloblastic and are characterized by abundant fine-grained inclusions of $Qz+Ap+Kfs+Pl+Bt+Ilm+Rt+Mnz+Zrn$, whereas rims ($Grt_R$) are inclusion-poor ($Kfs_1+Sil_1+Rt+Mnz$) with Qz_1-filled lobate margins (Figures 3c–d). Matrix minerals consist of $Qz_1+Sil_1+Kfs_1$ with elongate

morphology defining a sub-mm scale penetrative foliation that wraps around garnet porphyroblasts (Figures 3b–c).

Microstructural observations indicative of dehydration melting *via* reactions such as Bt+Pl+Sil+Qz→Grt+Kfs+melt include (i) the presence of rounded quartz as embayments and lobate inclusions in Kfs_1+Grt_R domains (Figures 3c–d), and (ii) matrix Bt_1 with irregular and ragged margins (Figure 3f). Matrix rutile is coarse-grained (100–200 μm) and commonly euhedral. These textural relationships suggest the peak assemblage consists of melt(Qz_1+Kfs_1)+Grt_R+Sil_1+Bt_1+Rt. Retrograde phases (Figure 3f) include anhedral biotite (Bt_2), fibrolite (Sil_2), anhedral chlorite and muscovite within garnet fractures, on prismatic Sil_1 rims and in fine-grained recrystallized (Kfs_2+Qz_2) matrix domains. Ilmenite is present as a late phase rimming matrix rutile, yet also occurs as anhedral crystals parallel to the foliation. Three equilibrium metamorphic assemblages, within this hanging wall domain, can be defined based on the above information: Sb^{Pg}-M_1) an earlier assemblage locally preserved as inclusions in Grt_C domains; Sb^{Pg}-M_2) an assemblage consisting of melt(Qz_1+kfs_1)+Grt_R+Sil_1+Bt_1+Rt; and Sb^{Pg}-M_3) a late metamorphic assemblage consisting of Bt_2+Sil_2+Chl+Ms+Ilm.

Zircon U-Pb and trace element data for this sample indicate a maximum deposition age of 1983 ± 19 Ma (Thiessen et al., 2018). Metamorphic zircon with fir-tree zoning and flattened heavy rare earth element (HREE) signatures overgrow detrital cores at 1915 ± 4 Ma (MSWD = 2.7, Thiessen et al., 2017). These metamorphic zircon rims were previously analyzed for trace element concentrations, which included Ti (Thiessen et al., 2018). Titanium concentrations range between 5.8 and 12.6 ppm that correlate to interquartile range crystallization temperatures of 710–730 °C (average 721 ± 8 °C) calculated using the Ti-in-zircon thermometer of Watson, Wark, and Thomas (2006). In this study, Sb^{Pg} was subjected to *in situ* U-Pb monazite chronology, apatite and quartz-in-garnet barometry, garnet and rutile trace element analysis, and petrologic modelling.

2.4.2 Mafic Granulite - WLsz^{MG}

The WLsz^{MG} gneiss (Figure 4a) contains two texturally distinct high P-T metamorphic assemblages; WLsz^{MG}-M_1 is a coarse-grained, granoblastic domain that consists of Grt+Cpx+Qz±Pl within cm-scale pods, whereas, WLsz^{MG}-M_2 is a fine-grained, granoblastic domain of Grt+Cpx+Pl+Qz±Ttn±Ilm that defines a gneissic foliation (orientation of 027°/60°, Table S1) correlated to S_{T1} that envelops WLsz^{MG}-M_1 domains (Thiessen et al., 2018, 2019). Titanite occurs as a granoblastic minor phase in textural equilibrium with WLsz^{MG}-M_2 Grt+Cpx+Pl+Qz (Figure 4b). Titanite crystals are typically equidimensional, 100–200 μm across, do not display zoning in BSE (back scattered electron imaging) and share straight crystal boundaries with the WLsz^{MG}-M_2 phases Grt+Cpx+Pl; some are also fully encased in garnet (Figure 4c). Given these textural relationships, and the absence of titanite from older M_1 domains within this sample, titanite is interpreted as a neocrystallized phase coeval with the WLsz^{MG}-M_2 assemblage.

Zircon U-Pb age components include an igneous crystallization population at 2592 ± 16 Ma and a recrystallized metamorphic population at 1890 ± 33 Ma, the latter of which was interpreted to correlate with the timing of S_{T1} deformation (Thiessen et al., 2018). Garnet from the WLsz^{MG}-M_1 domain yielded Lu-Hf age of 2111 ± 3 Ma and P-T conditions of 12 ± 1 kbar and >700 °C (Thiessen et al., 2019). Garnet separates from the WLsz^{MG}-M_2 domain returned preliminary Lu-Hf data that indicated an age of 1870 ± 40 Ma, which was then interpreted to constrain the timing of P-T conditions of 8–11 kbar and >750 °C (Thiessen et al., 2019). In this study, new data were collected for the WLsz^{MG}-M_2 domain to improve the resolution of the P-T-t history pertaining to S_{T1} development. These consist of additional

Lu-Hf isotope data for garnet, *in situ* U-Pb and trace element data of titanite, apatite-in-garnet barometric data and calculated garnet mode isopleths utilizing the data in Thiessen et al. (2019).

2.4.3 Paragneiss - WLsz^{Pg}

Paragneiss, interpreted to be a lens of Snowbird metasedimentary rocks entrained in the northern portion of the WLsz (WLsz^{Pg}) was collected in order to determine ages for S_{T2} foliation development. The entirety of the S_{T2} subdomain is crosscut by felsic dykes (Figure 5b, Thiessen, Regis, & Gibson, 2017, 2018) that are variably folded and locally transposed into S_{T2}, and exhibit an axial planar foliation parallel to S_{T2} with a southwest plunging mineral stretching lineation. Even so, the dykes generally display a lower degree of strain or no strain, indicating emplacement during the latter stages of S_{T2} ductile deformation. Ages for dyke emplacement and crystallization range between 1871 ± 5 and 1864 ± 2 Ma (Thiessen et al., 2018).

WLsz^{Pg} contains cm-scale layering of leucosome and melanosome within the S_{T2} foliation domain (Figure 5a). Dextral shear sense indicators within gneiss and mylonite are prevalent and consist of winged porphyroclasts (Figures 5c–d) and C' shear bands (Figure 5e). Porphyroblastic garnet is 1–4 mm in diameter that exhibits both straight crystal boundaries and less commonly lobate margins filled with Qz_1 (Figures 5d–e). Matrix-hosted Bt_1 occurs as 50–100 µm long crystals both as inclusions in garnet (Figure 5d) and within strain shadows accompanied by intergranular ilmenite and is also associated with matrix Qz_1+Pl_1. Matrix-hosted Bt_1 commonly displays irregular margins indicative of partial breakdown. The Pl_1 and Qz_1 (Figures 5d–e) are dominant matrix phases that exhibit elongate ~500-µm elongate crystals that partly define the main foliation, including shear bands, and have serrated margins and subgrains indicative of dynamic recrystallization (Figure 5e). Rare sillimanite occurs as

prismatic grains (Figure 5d) or fibrolite and is extensively replaced by fine-grained Ms_1. Small mm-scale leucosome subdomains consist of $Grt+Qz_1+Pl_1+Bt_1$, where garnet is ~1 mm wide and is characterized by a patchy texture of lobate Qz_1+Pl_1.

Assemblages comprising sub-50 μm $Bt_2+Pl_2+Ms_1+Chl_1+Qz_2$ define the foliation and occur aligned parallel to sub-mm domains that envelop garnet porphyroblasts and locally replace $Grt+Sil+Bt_1+Pl_1+Qz_1$ (Figures 5d–e). Garnet is rimmed by thin domains of $Bt_2+Pl_2+Qz_2$ (Figure S3), recording retrogression during shearing and S_{T2} foliation development. Late overprinting phases include sub-mm randomly oriented Ms_2+Chl_2+Crd that in some cases fully replace garnet (Figure 5f).

Based on these observations, we define three phases of metamorphism; $WLsz^{Pg}$-M_1: A high-grade assemblage of $Grt+Sil+Bt_1+Pl_1+Qz_1$ where Pl_1+Qz_1 may define a former melt phase within leucosome subdomains, $WLsz^{Pg}$-M_2: a fine-grained S_{T2} foliation defining assemblage of $Bt_2+Pl_2+Ms_1+Chl_1+Qz_2$, and $WLsz^{Pg}$-M_3: randomly oriented Ms_2+Chl_2+Crd. Assemblage $WLsz^{Pg}$-M_2 correlates with the dextral strain preserved in $WLsz^{Pg}$, which defines the S_{T2} foliation. The transposition of assemblage $WLsz^{Pg}$-M_1 into S_{T2} obscures interpretation of the initial structural fabric or orientation. New *in situ* U-Pb monazite isotopic constraints were collected to date foliation development in this sample.

3 METHODS

3.1 Garnet major element determination

Garnet major element compositions were collected at the Pacific Centre for Isotopic and Geochemical Research at the University of British Columbia. Electron-probe micro-analyses (EPMA) were done on a

fully automated CAMECA SX-50 instrument, operating in the wavelength-dispersion mode with the following operating conditions: excitation voltage, 15 kV; beam current, 20 nA; peak count time, 20 s (Na peak count time, 60 s); background count-time, 10 s (Na background count time, 30 s); spot diameter, 5 μm. Data reduction was done using the 'PAP' $\phi(\rho Z)$ method (Pouchou & Pichoir 1985). For the elements considered, the following standards, X-ray lines and crystals were used: albite, Na$K\alpha$, TAP; pyrope, Mg$K\alpha$, TAP; pyrope, Al$K\alpha$, TAP; pyrope, Si$K\alpha$, TAP; pyrope, Ca$K\alpha$, PET; rutile, Ti$K\alpha$, PET; magnesiochromite, Cr$K\alpha$, LIF; synthetic rhodonite, Mn$K\alpha$, LIF; pyrope, Fe$K\alpha$, LIF.

3.2 Trace elements determination

Laser ablation inductively coupled mass spectrometry (LA-ICPMS) analyses of garnet and rutile (Tables S2–S3) were conducted by an ArF excimer laser ablation system (193 nm; Resolution M-50LR, ASI Australia) connected to a Quadrupole ICP-MS (Agilent 7700x) at the Pacific Centre for Isotopic and Geochemical Research at the University of British Columbia. Measurements were performed at a repetition rate of 8 Hz and using a spot size of 90 μm for garnet and 25 μm for rutile. Energy density on the sample was 4.50 J/cm^2. Ablation was carried out under a Helium atmosphere. Argon served as carrier gas and was admixed with N_2 for signal enhancement. Calibration was carried out using the silicate glass SRM NIST612 for garnet and USGS basalt reference material BCR2-G for rutile as external standard. Internal standardization was performed using ^{30}Si (from EPMA analyses) for garnet and ^{49}Ti for rutile (59.94 wt.%). Data reduction was performed using Igor Pro version 6.32 and Iolite version 2.5.

Rutile was analyzed in order to obtain temperature estimates by the method in Tomkins, Powell, and Ellis (2007). Matrix rutile varied in size substantially (10–200 μm), thus, Grt_R-hosted crystals and

the cores of >100 μm-wide grains from mineral separates were targeted specifically to avoid potential effects of the diffusive re-equilibration of Zr composition at high-temperature. Errors associated with calculated rutile temperatures are <10 °C (e.g., Watson et al., 2006).

3.3 Quartz and apatite in garnet barometry

Raman spectra of quartz and apatite inclusions in garnet from a standard 30 μm thin section were obtained at Virginia Polytechnic University. Measured inclusions range from 4 to 7 μm in diameter, are mostly spherical (<2:1 aspect ratio) and were located close to the center of the section (not exposed on either polished surface) away from visible cracks, grain boundaries and alteration. Unpolarized Raman spectra of quartz and apatite inclusions in garnet were obtained on a JY Horiba LabRAM HR800 Raman microprobe, with a high-resolution 800 mm focal-length spectrometer (1800 lines/mm grating) and a 514.57 nm argon laser (100 mW laser power at the source). High spatial (~1 μm) resolution was achieved using a 100x objective (NA = 0.90) and a confocal aperture set to 400, with a slit width of 150 μm. Spectra were centered on 360 cm^{-1} for quartz to allow for the collection of the three main Raman bands for quartz (~464, 206 and 127 cm^{-1}) and simultaneous collection of three Ar plasmalines (520.30, 266.29 and 116.04 cm^{-1}), which allows for drift correction. Apatite spectra were centered on 1000 cm^{-1} to allow for collection of the symmetric phosphate stretching mode at ~964 cm^{-1} and a neon calibration line at 918.66 cm^{-1}. Analyses were collected using a 30 s acquisition time, iterated for three collections. All Raman lines were fitted using Peakfit v. 4.12 from SYSTAT Software Inc., using a symmetric Gaussian-Loren model for fitting the calibration lines, the asymmetric Pearson IV model for fitting the quartz bands, and the Pearson VII Area model for fitting the apatite band.

Inclusion pressure was determined by measuring the frequency shift in the 464 cm^{-1} and 964 cm^{-1} bands for quartz and apatite, respectively. A Herkimer quartz standard was used for the ambient peak

position; because the ambient peak position of the phosphate stretching mode in apatite is sensitive to composition, inclusions exposed at the surface of the thin sections were analyzed and treated as the zero-pressure position (c.f., Barkoff, Ashley, & Steele-MacInnis, 2017). Inclusion pressures were calculated using polynomial regressions based on experimental data for the *P*-dependent Raman peak shifts (Schmidt & Ziemann, 2000; Schouwink et al., 2010).

Entrapment pressure (Table S4) was calculated using the approach described in Ashley, Steele-MacInnis, Bodnar, & Darling (2016) and Ashley, Barkoff, & Steele-MacInnis (2017), which is summarized here. Molar volume of the inclusion and host are calculated at room T and P (accounting for the residual pressure of the inclusion). The values representing the calculated inclusion pressure are used in the isotropic elastic model of Guiraud and Powell (2006). Molar volume of the inclusion and host are iterated across a pressure range at the assumed entrapment temperature until the elastic model equation is balanced. (Note that at the time of trapping, the inclusion pressure and externally applied pressure would be equal.) Ashley et al. (2016) conducted heating experiments that showed measured inclusion pressures for fully encapsulated quartz inclusions in garnet were significantly lower than inferred through elastic theory. This results in entrapment pressures being significantly overestimated. In response, we use the method described by Ashley et al. (2016) to correct for these overestimates in entrapment pressure. Heating experiments conducted by Ashley et al. (2017) shows the apatite-in-garnet system does not require a correction. We calculate entrapment P assuming pure garnet endmembers (almandine, spessartine, grossular and pyrope) and assume ideal mixing to account for mixing effects on calculated entrapment conditions. Solid solution in apatite was handled in the same way between the three anion ternary endmembers (fluor-, chlor-, and hydroxyl-apatite). Calculated entrapment pressures did not account for strain anisotropy, which is currently only applicable to alpha-quartz. However, it should be noted that the corrections used herein on dilated inclusions have been demonstrated in

Barkoff, Ashley, Guimarães Da silva, Mazdab, and Steele-MacInnis (2019) to reproduce known pressures on similar dilated inclusions.

3.4 Lu-Hf isotope analyses

Garnet and clinopyroxene populations from the $WLsz^{MG}$-M_2 assemblage were isolated from their respective metamorphic/textural domains first using a diamond blade and then extracted by hand-crushing and at Simon Fraser University in Burnaby, BC, Canada. These separates were collected from the same cm-scale $WLsz^{MG}$-M_2 domain from which two previous garnet separates were derived and subjected to Lu-Hf isotopic analyses (see Thiessen et al., 2019). Two clean mineral separates consisting of multigrain c. 0.5 mm garnet and clinopyroxene fragments were collected. Lutetium and hafnium isotope analyses were performed at the Pacific Centre for Isotopic and Geochemical Research, Department of Earth, Ocean and Atmospheric Sciences, University of British Columbia, Vancouver, BC, Canada. Data are presented in Table S5. Mineral separates were transferred to, and weighed in, screw-top PFA beakers, washed twice with de-ionized water, and bathed in 1 N HCl at room temperature for 1 h. A mixed ^{176}Lu-^{180}Hf tracer with matrix-equivalent Lu/Hf was admixed with the mineral and clinopyroxene aliquots. These analytes were then dissolved using sequential addition of HF-HNO_3-$HClO_4$ and HCl interspersed with full sample dry-down on a hotplate. This method effectively dissolves garnet while leaving behind Hf-bearing, refractory minerals such as zircon, which may carry Hf that did not equilibrate isotopically with the rock (Lagos et al., 2007). Garnet aliquots were kept as small as possible given the required amount of Hf needed for sufficiently precise analysis. This was done to minimize homogenization of different age components should these be present. The spike-equilibrated mineral aliquots were re-dissolved in 6 N HCl, diluted to 3 N HCl, and loaded onto

preconditioned 12 mL Teflon® columns containing Eichrom® Ln-Spec resin. Lutetium and hafnium were isolated using cation exchange chemistry modified from Münker, Weyer, Scherer, and Mezger (2001).

The Lu and Hf isotope measurements were done using a Nu Instruments *plasma HR* multi-collector ICPMS (MC-ICPMS). Analyte $^{176}Lu/^{175}Lu$ was determined following corrections for isobaric interference of ^{176}Yb after Blichert-Toft, Boyet, Télouk, and Albarède (2002). Mass bias correction for Hf was done assuming the exponential law and applying $^{179}Hf/^{177}Hf = 0.7325$. Hafnium isotope ratios are reported relative to JMC-475 ($^{176}Hf/^{177}Hf = 0.282163$; Blichert-Toft, Chauvel, & Albarède, 1997), for which the lab maintains a long-term external reproducibility of 0.4 εHf at the average concentration of typical garnet samples. External reproducibility (2SD) was estimated on the basis of the external reproducibility for JMC-475 measured at concentrations that bracketed those of the unknowns (10–40 ppb; Bizzarro, Baker, & Ulfbeck, 2003). Isochron regression and age calculation were done using Isoplot version 3.27 (Ludwig, 2005), applying 1.867×10^{-11} yr^{-1} for $\lambda^{176}Lu$ (Scherer, Münker, & Mezger, 2001; Söderlund, Patchett, Vervoort, & Isachsen, 2004). All uncertainties are reported at the 2SD-level.

3.5 U-Pb titanite geochronology and trace element analyses

Polished thin sections for $WLsz^{MG}$ were imaged using QEMSCAN at SGS Labs in Burnaby, British Columbia, which produced full section back scattered electron and qualitative SEM phase maps. Titanite crystals were analyzed *in situ* using a laser-ablation split-stream inductively coupled plasma mass spectrometer at the University of California Santa Barbara. This technique simultaneously collects both U-Pb isotopic and trace element data from the same volume of ablated material, which allows a direct comparison of isotopic age and trace element contents. A description of the analytical instruments,

procedures and operating conditions are the same as in Garber, Hacker, Kylander-Clark, Stearns, & Seward (2017). Data (Table S6) are presented in Tera-Wasserburg inverse concordia diagrams in order to better visualize how common-Pb components affect the distribution of data. Error ellipses on the concordia plots and the weighted mean uncertainties are reported in the text and figures at 95% confidence intervals unless otherwise stated. Concentrations of Zr in titanite were utilized with the equation of Hayden, Watson and Wark (2008) for thermometry. Errors associated with calculated temperatures are <20 °C.

3.6 U-Pb monazite geochronology

Monazite U-Pb dates were obtained using the sensitive high-resolution ion microprobe 2 (SHRIMP) at the J.C. Roddick Ion Microprobe facility at the Geological Survey of Canada. U–Pb analyses of monazite were performed *in situ* with selected targets cored from the two thin sections and mounted in epoxy together with laboratory standard monazites (primary standard: GSC monazite z8153, $^{206}Pb/^{238}U$ age = 511.6 Ma; $^{206}Pb/^{238}U$: 0.0826, secondary standards: GSC monazite z3345, $^{207}Pb/^{206}Pb$ age = 1821 Ma; GSC monazite and z2908, $^{207}Pb/^{206}Pb$ age = 1795 Ma, see Stern and Berman, 2001). Mount surfaces were polished and coated with 10 nm of high purity Au. Details of the SHRIMP analytical procedure are given by Rayner and Stern (2002), and analytical protocols for monazite are described in detail by Stern and Berman (2001). Analyses were conducted during one analytical session using an O_2- primary beam, with a kohler 50 aperture corresponding to a spot size of c. 12µm×9µm with a beam current of ~ 0.4 nA. The count rates of 12 isotopes of Ce, Y, U, Th, and Pb were sequentially measured over 5 scans. No fractionation correction was applied to the Pb-isotope data; common Pb correction utilized the Pb composition of the surface blank (Stern, 1997). For the analytical session error (1σ) in $^{206}Pb/^{238}U$ calibration is 1.38%, and the error (1σ) in $^{208}Pb/^{232}Th$ calibration is 1.15%. Isoplot (Ex.

version 3.00; Ludwig, 2003) was used to generate mean ages with related statistics. Error are plotted on all figures at the 95% confidence interval. All quoted ages in the text are calculated as the weighted mean of ^{204}Pb corrected $^{207}Pb/^{206}Pb$ ages, with associated uncertainty at the 95% confidence interval.

Full thin section elemental maps (for Ca) with monazite locations of samples Sb^{Pg} and $WLsz^{Pg}$ are shown in Figures S1–S2. The textural associations of monazite crystals encased in garnet are displayed in BSE images with corresponding monazite crystals labelled. Individual monazite crystals were imaged with BSE or elemental maps (Y, Th); the latter imaging and whole section maps were conducted at the University of Massachusetts, Amherst. Monazite crystal names (e.g., M1, M2) are also reported with the U-Pb data in Table 1 under the title "Grain #".

3.7 P-T modelling

Herein we utilize the pseudosection approach with the Na_2O-MgO-Al_2O_3-SiO_2-K_2O-CaO-TiO_2-MnO-FeO-H_2O system (with wt.% $H_20^{0.18}$, $SiO_2^{54.94}$, $Al_2O_3^{21.29}$, $CaO^{0.48}$, $MgO^{2.16}$, $FeO^{13.5}$, $Na_2O^{0.59}$, $K_2O^{5.17}$, $MnO^{0.27}$, $TiO_2^{1.41}$) to investigate the peak and post-peak metamorphic conditions of sample Sb^{Pg}. The modelled bulk-composition was derived from combining phase modal abundances derived from point counting (n = 730) of an entire thin section and quantitative mineral chemistry from EPMA analyses (Table S7). The EPMA data were recast into molecular mineral formula using a standard number of oxygen atoms per formula unit. Bulk rock Fe^{3+} is considered negligible since Fe^{3+}-bearing phases such as magnetite and epidote are absent. Pseudosections were calculated using Perple_X (version 6.8.4, Connolly, 1990, 2009) and the internally consistent thermodynamic dataset and equations of state for H_2O of Holland and Powell (1998, 2011). Minerals considered in the calculation were garnet, quartz, plagioclase, K-feldspar, clinopyroxene, orthopyroxene, amphibole, white mica, biotite, chlorite, spinel, staurolite, kyanite, sillimanite, andalusite, cordierite, rutile and ilmenite. Solution models used were

white mica (Auzanneau, Schmidt, Vielzeuf, & Connolly, 2010; Coggon and Holland, 2002), clinoamphibole (Diener, Powell, White, & Holland, 2007), clinopyroxene (Green, Holland, & Powell, 2007), orthopyroxene (Holland and Powell, 1996), granitic melt (Holland and Powell, 2001; White, Powell, & Holland, 2001), chlorite (Holland, Baker, & Powell, 1998), plagioclase (Newton, Charlu, & Kleppa, 1980), Ti-biotite (Tajcmanová, Connolly, & Cesare, 2009), K-feldspar (Thompson and Hovis, 1979) and garnet (White, Powell, Holland, & Worley, 2000). Fluid was considered as pure H_2O, and water content was calculated using stoichiometry and modal proportions of hydrated phases. Pure phases considered are quartz, cordierite, kyanite, sillimanite, andalusite, staurolite, rutile, ilmenite and spinel. Major element profiles in garnet crystals are weakly zoned to flat suggesting high-temperature diffusional resetting since initial growth. The lack of major element zonation allows for the calculated pseudosection to represent near-equilibrium conditions and does not require adjustments for zoned minerals (e.g., Mn from garnet cores) from bulk rock values.

Utilizing the methods and data from Thiessen et al. (2019), we calculated garnet mode isopleths for the $WLsz^{MG}$-M_2 assemblage (Figure S3) in order to better understand the samples petrologic evolution.

4 RESULTS

4.1 Snowbird paragneiss - Sb^{Pg}

4.1.1 Garnet major and trace element chemistry

The garnet porphyroblasts commonly lack significant zonation and generally have flat profiles for major elements across core and rim domains (Figure 6). Compositional ranges from core to rim are $Alm_{0.59-0.73}Prp_{0.18-0.25}Grs_{0.028-0.041}Sps_{0.02-0.03}$. Compositional maps (Figure 6) show increased Mn concentration for the outer 50 μm of garnet rims. Garnet preserves Y and REE zonation that includes a clear break between Grt_C and Grt_R (Figure 6). The inclusion-rich Grt_C domains are characterized by outward-increasing middle and heavy (M-H)REE concentrations; Y concentrations increase from c. 80 to 150 ppm, with similar increases observed for Gd and heavier REE. Inclusion-poor Grt_R displays a sharp outward decrease in Y, MREE and HREE concentrations.

4.1.2 Rutile trace element chemistry

Grt_C-hosted rutile (average 1040 ppm Zr) was targeted to constrain temperatures estimates for Sb^{Pg}-M_1, whereas larger matrix crystals, separates and Grt_R-hosted rutile (average 1730 ppm Zr) were used to estimate the temperature attained during Sb^{Pg}-M_2. Twenty-six *in situ* analyses were conducted on 26 rutile crystals included in Grt_C domains. Because the Zr-in-rutile temperatures are pressure sensitive, the interquartile Zr-temperatures from Grt_C-hosted rutile are assessed at a range of pressures between 4 and 12 kbar, which is a range that covers most typical crustal pressures. At 4 kbar the interquartile Zr-temperature range for Grt_C-hosted rutile is 670 to 813 °C, whereas at 12 kbar the range is 706 to 813 °C. The large Grt_R-hosted rutile grains and the grains from mineral separates yielded interquartile Zr-temperatures of 760 to 807 °C at 4 kbar and 804 to 849 °C at 12 kbar. The temperature band (steep positive slope in P-T space) derived from Grt_C-hosted rutile are combined with pressure estimates (shallow positive slope in P-T space) derived from quartz inclusion barometry, which together are plotted as yellow polygons (Figure 7a). The temperature band derived from Grt_R-hosted, and grain

mounted rutile separates are combined with pressure estimates derived from apatite inclusion barometry, which together are also plotted as a yellow polygon in P-T space (Figure 7a).

4.1.3 Quartz- and apatite-in-garnet barometry

Grt_C domains generally contain a central (Qz_a) and more distal (Qz_b) population of quartz inclusions. Additionally, a transitional zone between Grt_C and Grt_R hosts a population of apatite (Ap_c) inclusions (Figure 6). With the band of calculated rutile temperatures derived from within Grt_C, quartz entrapment pressures ranged between ~3 to 7 kbar for Qz_a and ~5 to 9 kbar for Qz_b (Figure 7a). Apatite entrapment pressures are plotted with the band of calculated rutile temperatures from Grt_R and the grain mounted rutile separates that yielded pressures between 7.5 and 10.0 kbar. These data are consistent with continued prograde burial and heating during garnet growth. However, since even the highest-pressure populations can be affected by later dilation, the P-T data broadly define minimum conditions. The combined inclusion barometry and rutile thermometry results are, thus, interpreted to represent Grt_C growth during two stages between 3 and 7 kbar and 5 and 9 kbar (and 660 to 800 °C), as well as Grt_R growth between 7.5 and 10 kbar at 775 to 880 °C.

4.1.4 Petrologic evolution and modelling

An equilibrium phase diagram (Figure 7a) was calculated to estimate peak P-T conditions and to constrain a retrograde P-T path that can be linked to geochronologic data below. Due to the high degree of melting experienced by this sample, the modelled subsolidus fields cannot be used to predict the prograde evolution without melt reintegration. The Sb^{Pg}-M_2 mineral assemblage of

melt(Qz_1+kfs_1)+Grt_R+Sil_1+Bt_1+Rt is predicted to have equilibrated at conditions between 810 and 830 °C and 7.0 to 10.5 kbar based on the observed stability of the major silicates Qz_1+Kfs_1+Grt_R+Sil_1+Bt_1. The consideration of rutile in the peak assemblage refines pressure estimates to between 9.0 and 10.5 kbar, which is consistent with independent P-T constraints from apatite-in-garnet barometry coupled with Zr-in-rutile thermometry. Compositional isopleths (not shown) for $X_{Grs}^{0.35}$, $X_{Prp}^{0.25}$ and $X_{Or}^{0.84}$ and mode percent isopleths for Grt^{28}, Kfs^{38}, Qz^{17}, Sil^{10} and Bt^{5} (Table S7) occur within, but nearly parallel to isotherms within the stability field for Sb^{Pg}-M_2. Therefore, isopleths support peak P-T conditions of 810 and 830 °C and 7.0 to 10.5 kbar, but do not provide more refined pressure estimates.

4.1.5 U-Pb and trace elements in Monazite

Sample Sb^{Pg} contains abundant monazite crystals that are typically equidimensional (c. 50 μm wide) with some straight crystal facets (Figure 8). Two distinct monazite populations are differentiated based on Y concentrations. The first population (Mnz-1) consists of high-Y crystals that are included in inclusion-poor Grt_R, in an inclusion-rich Grt_C, and as cores of monazite crystals within the matrix. They have relatively high-Y (810–4340 ppm) and low Th/U values (3–15). Microfractures in garnet intersect two crystals yet their chemistry and morphology are similar to pristine inclusions. The boundaries between Mnz-1 cores and subsequent low-Y rims are irregular and sharp suggestive of resorption prior to Mnz-2 growth. The second population (Mnz-2) consists of eleven low-Y matrix-hosted equidimensional to elongate whole crystals or rim domains that host cores of Mnz-1. This population has relatively low-Y (193–486 ppm) and slightly higher Th/U values (12–37) than the Mnz-1 population.

Twenty-four analyses on 15 monazite crystals yielded $^{207}Pb/^{206}Pb$ dates between 1943 to 1869 (Figure 8, Table 1). Mnz-1 analyses have an age range of 1943 to 1930 Ma. Nine concordant analyses on five crystals yielded a weighted-mean $^{207}Pb/^{206}Pb$ date of 1935 ± 5 Ma (MSWD = 1.5). Fifteen concordant analyses spanning 1931 to 1869 Ma from 11 Mnz-2 domains yielded a weighted-mean $^{207}Pb/^{206}Pb$ date with excess scatter of 1915 ± 9 Ma (MSWD = 4). The fourteen oldest Mnz-2 analyses form an age cluster that yielded a weighted-mean $^{207}Pb/^{206}Pb$ date of 1917 ± 8 Ma (MSWD =

4.2 Mafic granulite - $WLsz^{MG}$

4.2.1 Apatite in garnet barometry

Eleven apatite inclusions hosted in garnet porphyroblasts were analyzed. Barometric data are plotted between 790 and 890 °C based on a permissible temperature range indicated by stable mineral phases ($WLsz^{MG}$-M_2 Grt+Cpx+Pl+Qz) and their modal proportions determined from petrologic modelling of the sample (Thiessen et al., 2019). Barometric estimates are combined with the stated temperature range and together they are plotted as a polygon in P-T space (Figures 9a–b).

4.2.2 Lu-Hf Garnet and petrologic evolution

The two new Lu-Hf analyses of the $WLsz^{MG}$-M_2 garnet and clinopyroxene, coupled with the two prior analyses (Thiessen et al., 2019), yield an apparent age of 1873 ± 5 Ma (MSWD = 0.8; Figure 9c). Newly

calculated garnet mode isopleths for $WLsz^{MG}$-M_2 (Figure S3) have positive slopes that indicate garnet growth required an increase in pressure.

4.2.3 U-Pb and trace elements in Titanite

In order to use the trace element composition of titanite to inform the thermal history of $WLsz^{MG}$-M_2 we obtained isotopic ages that demonstrate that titanite grew at the same time as S_{T1} fabric development and garnet growth. Seventy *in situ* LA-ICP-MS analyses on 30 titanite crystals were performed within the same $WLsz^{MG}$-M_2 domain in which garnet and clinopyroxene were extracted for Lu-Hf analysis. These U-Pb titanite analyses yielded a cluster of concordant and near concordant data at ca. 2.0 to 1.9 Ga, as well as multiple discordant analyses (Figure 9d). Although largely concordant, the data indicate the presence of two inherited components, one having a primordial common-Pb composition and the other corresponding to a 2.6 Ga common-Pb composition (Figure 9d) consistent with a 2.6 Ga protolith age (Thiessen et al., 2018). No correlation was found between apparent concordia age, Zr concentration, Th/U, Al/(Al+Fe), REE compositions and textural location.

Two discordia arrays with distinct slopes can be identified by selecting data above $^{207}Pb/^{206}Pb$ values of 0.125. Near concordant data was iteratively added to the steeper array by selecting high to low $^{238}U/^{206}Pb$ values until the MSWD of the calculated regression was equal to one. The same technique was applied to the shallower array, iteratively adding low to high $^{238}U/^{206}Pb$ data until the MSWD of the calculated regression was equal to one. A linear regression (model-1, Vermeesch, 2018) through the shallow sloped array (n = 38) yielded a date of 1887 ± 26 Ma (MSWD = 1, p.o.f. = 0.45). A linear regression through the steeply sloped data (n = 53) returned an apparent age of 1881 ± 9 Ma (MSWD = 1, p.o.f. = 0.46).

Titanite contain a range of Zr values between 370 and 800 ppm. Utilizing these Zr concentrations with pressures consistent with prior petrologic modelling yielding between 9 and 12 kbar (Thiessen et al., 2019), an interquartile Zr-in-titanite temperature range between c. 820 and 870 °C is plotted. The derived P-T window is compared (Figure 9a) with apatite-in-garnet barometric estimates and previously reported less-precise P-T constraints (c. 8–11 kbar and >750 °C, Thiessen et al., 2019).

4.3 Paragneiss - WLsz^{Pg}

4.3.1 U-Pb and trace elements in monazite

The twenty-three *in situ* U-Pb analyses of ten monazite crystals yielded concordant dates from 1947 to 1895 Ma. Three distinct monazite populations can be differentiated based on Y and Th concentrations and Th/U values (Figure 10, Table 1). Mnz-1 is defined by irregular, patchy and oscillatory zones with high-Y (7266–10158 ppm) and Th/U values between 4–12. High-Y Mnz-1 crystals consist of core domains in four equidimensional to elongate (4:1 aspect ratio) crystals encased in Grt_C and one core domain in a matrix-hosted crystal. Boundaries between Mnz-1 cores and younger low-Y rims are sharp and irregular indicating some dissolution prior to later monazite growth.

The Mnz-2 population consists of low-Y matrix hosted core domains and a whole crystal encased in Grt_R. This population has relatively low-Y (874–2342 ppm) and similar Th/U values (2–11) compared with the Mnz-1 population. Clear core-rim relationships are visible in Th maps (Figure 10) that distinguish Mnz-2 from Mnz-3, where rims truncate core zones suggesting a second episode of dissolution and new growth. The Mnz-3 population consists of matrix hosted whole grains and rim

domains on Mnz-2 cores that have relatively similar-Y (172–1669) but higher Th/U (9–52) compared to Mnz-2.

Eight concordant analyses of Mnz-1 yielded $^{207}Pb/^{206}Pb$ dates between 1947 and 1927 Ma. These analyses yielded a weighted-mean $^{207}Pb/^{206}Pb$ date of 1936 ± 6 Ma (MSWD = 2.5). Five concordant Mnz-2 analyses yielded a weighted-mean $^{207}Pb/^{206}Pb$ date of 1925 ± 4 Ma (MSWD = 0.61). Ten Mnz-3 analyses yielded a weighted-mean $^{207}Pb/^{206}Pb$ date of 1906 ± 6 Ma (MSWD = 1.6).

5 DISCUSSION

5.1 P-T-t-D evolution of the Snowbird metasediments

5.1.1 D_1 – 1.94 to 1.93 Ga prograde evolution

Monazite (Mnz-1) from both Sb^{Pg} and $WLsz^{Pg}$ have a mean age of 1935 ± 5 Ma and 1936 ± 5 Ma respectively, have relatively high Y concentrations and have straight grain boundaries that indicate they are not detrital, but instead represent neoblasts. Their high Y and low Th concentrations indicate that they formed prior to garnet stability or during early garnet growth prior to melting. Grt_C domains in Sb^{Pg} show an outward zonation of increasing REE concentrations, which indicates breakdown of lower-grade REE phases such as allanite and epidote, and also would have aided in mnz-1 growth. Pressure and temperature constraints in Sb^{Pg} for Grt_C growth yield two stages of 3 to 7 kbar and 5 to 9 kbar between 660 and 800 °C based on combined Zr-in-rutile thermometry and quartz-in-garnet barometry of Qz_a and Qz_b populations (Figure 7). Because the Qz_a and Qz_b populations occur at increasing distance away from the garnet center, their entrapment likely occurred sequentially during burial on a prograde P-T path.

Because the high-grade Sb^{Pg}-M_2 assemblage of melt(Qz_1+Kfs_1)+Grt_R+Sil_1+Bt_1+Rt closely resembles the high-grade $WLsz^{Pg}$-M_1 mineral assemblage of Grt+Sil+Bt_1+Pl_1+Qz_1+Ilm±melt, and because Mnz-1 textural locations and U-Pb data are nearly identical in both samples, they are both interpreted to have undergone the same prograde P-T history. Thus, 1.94 to 1.93 Ga is interpreted to represent the interval in which early prograde, pre- to syn-Grt_C growth occurred, which was 20 to 60 Myr after sediment deposition at 1983 ± 19 Ma (Thiessen et al., 2018). A comparison with peak P-T conditions (Figure 7) establishes a burial rate of ~1km/Myr, which is consistent with global Paleoproterozoic burial rates (e.g., Nicoli, Moyen, & Stevens, 2016). Also, $WLsz^{Pg}$ is clearly similar to Sb^{Pg} and other Snowbird metasedimentary rocks (Ashton et al., 2017a; Martel et al., 2008) in terms of rock type, metamorphic assemblages, and petrographic and age components. Thus, $WLsz^{Pg}$ is interpreted to be derived from Snowbird metasedimentary rocks of the Dodge-Snowbird domain, which were reworked by the formation of S_{T2} in the WLsz.

Within the Snowbird metasediments farther east, 1.94 to 1.92 Ga monazite have been interpreted to record the prograde formation of an early east-southeast striking gneissic foliation (S_1) (Martel et al., 2008; Williams and Jercinovic, 2012). Together, our data in combination with prior work illustrates that D_1 (see Table 2) in the Dodge-Snowbird domain corresponds to east-southeast striking foliation development, folding (S_1, F_1) and prograde burial metamorphism that initiated at c. 1.94 Ga.

5.1.2 D_2 – 1.93 to 1.91 Ga peak metamorphism and initial cooling

Peak metamorphism in Sb^{Pg} was contemporaneous with biotite dehydration partial melting, leucosome development and melt-loss resulting in garnet-rich restitic melanosome (Figure 3). Petrologic modelling predicts peak metamorphic conditions of 810 to 830 °C and 9.0 to 10.5 kbar, which overlaps with

independent constraints from apatite-in-garnet barometry and Zr-in-rutile thermometry of 775 to 880 °C and 7.5 to 10.0 kbar (Figure 7). However, the transitional location of Ap_c inclusions between Grt_C-Grt_R suggests that entrapment probably took place at higher temperatures than for Qz_b, but probably lower than suprasolidus peak temperatures of 810 to 830 °C since apatite is predicted to dissolve during anatectic melt generation (e.g., Yakymchuk and Brown, 2014). The lowest pressure result for Ap_c inclusions within the melt-present peak assemblage field is 8.5 kbar, which is a reliable minimum peak pressure estimate for this sample and, therefore, the modelling results of 810 to 830 °C and 9.0 to 10.5 kbar for peak conditions are considered robust. Timing of peak metamorphism is best approximated by the garnet stable (low-Y and Th) Mnz-2 population in the $WLsz^{Pg}$ at 1925 ± 4 Ma. This age either dates subsolidus growth immediately prior to peak conditions or it dates garnet stable anatexis at peak conditions where the Mnz-2 crystals remained shielded from the melt phase.

In order to understand metamorphic zircon's role in the petrogenesis of Sb^{Pg}, equilibrium between metamorphic zircon neoblasts and garnet is assessed with the REE partitioning array approach of Taylor et al. (2017). We achieve this by the combination of zircon REE data from Thiessen et al. (2018) and garnet REE data from the current study. This approach allows the visualization of both the shape and abundance of REE distributions between zircon and garnet domains, which are then compared to experimental data sets. Zircon-garnet REE distribution data that share REE distribution slope and abundances of experimental data (e.g., Taylor et al., 2015) are, thus, considered to have grown in equilibrium (Taylor et al., 2017). If the natural and experimental data do not overlap, they are considered to be in disequilibrium. Domains included in the analysis are detrital zircon cores, metamorphic fir-tree zoned zircon rims, inclusion-rich Grt_C domains, and inclusion-poor Grt_R domains. Detrital zircon cores plot as a distinct 'data-cloud' away from the linear experimental REE arrays (Figure 11). Metamorphic zircon rims and averaged Grt_C REE distributions plot along a positive-sloped

REE array parallel to, but offset from, the experimental data of Taylor et al. (2015). However, the metamorphic zircon rims and averaged Grt_R REE distributions overlap the experimental data array of Taylor et al. (2015), which suggests equilibrium partitioning occurred between these two phases. Whether metamorphic zircon grew as a peritectic phase in the presence of melt at peak conditions or if it grew upon cooling and crystallization of melt is unclear from this data alone.

Other characteristics such as morphology, internal zonation and trace element signatures can aid in the interpretation of metamorphic zircon paragenesis. These zircons have small <50 μm, rounded, and resorbed detrital cores that are overgrown by internally fir-tree zoned, externally spherical to multi-faceted metamorphic neoblasts (Thiessen et al., 2018). This, in conjunction with their HREE depletion (Thiessen et al., 2018) and equilibrium with peritectic Grt_R domains (Figure 11), indicates that metamorphic zircon likely grew in the presence of anatectic melt (e.g., Corfu, Hanchar, Hoskin, & Kinny, 2003; Hoskin and Schaltegger, 2003) with stable garnet. The resorbed and rare detrital cores, however, suggest that Zr undersaturated anatectic melt at peak temperatures dissolved all but the largest precursor zircon grains and that subsequent zircon growth resulted from Zr saturation of the melt, potentially during cooling (e.g., Kelsey, Clark, & Hand, 2008; ; Kohn, Corrie, & Markley, 2015; Yakymchuk and Brown, 2014). Only minor cooling from peak conditions would have been necessary to promote melt crystallization since only ~30 °C separates the solidus from maximum predicted temperatures (Bt-out curve, Figure 7a). However, average interquartile Ti-in-zircon temperatures yield 721 ± 8 °C, which is substantially lower than the c. 810 °C modelled solidus temperature. This discrepancy may be due to unreliable temperature estimates derived using this technique (e.g., Gervais and Crowley, 2017; Hofmann, Baker, & Eiler, 2014) rather than errors introduced by the petrologic modelling and independent thermobarometry. Furthermore, garnet- and likely melt-stable Mnz-2 in Sb^{Pg} and Mnz-3 in $WLsz^{Pg}$ grew on resorbed pre- to syn-garnet monazite cores at 1917 ± 8 Ma (Sb^{Pg}) and

1906 ± 6 Ma ($WLsz^{Pg}$), which is slightly younger than near peak P-T Mnz-2 in $WLsz^{Pg}$ dated at 1925 ± 4 Ma, and is within error of metamorphic zircon in Sb^{Pg} that grew at 1915 ± 4 Ma (Thiessen et al., 2017). Monazite is also predicted to be unstable during the suprasolidus prograde path in most rocks with pelitic compositions (Kelsey et al., 2008; Yakymchuk, 2017; Yakymchuk, Clark, & White, 2017), thus, chemistry and internal zonations of Mnz-2 (Sb^{Pg}) and Mnz-3 ($WLsz^{Pg}$) are consistent with the interpretation of growth upon cooling and crystallization of anatectic melt.

Despite being caught up in the WLsz, sample $WLsz^{Pg}$ appears to have undergone a similar P-T-t cycle as Sb^{Pg}, thus, $WLsz^{Pg}$ is interpreted to preserve an older high-grade history that is distinct from its host S_{T2} domain. The lower-grade, greenschist to amphibolite-facies $WLsz^{Pg}$-M_2 assemblage consists of fine-grained, S_{T2} foliation defining $Bt_2+Pl_2+Ms_1+Chl_1+Qz_2$, where Pl_2 envelops garnet porphyroblasts (Figure S2) indicating garnet was actively breaking down at this time. Although Mnz-3 exhibits elongate crystals with asymmetric dextral tails (Figure S2) that are now parallel to the prominent S_{T2} foliation, Mnz-3 has low-Y concentrations, which suggests garnet was not actively breaking down during this monazite growth. Despite the apparent textural relation of this monazite to S_{T2}, petrologic evidence and other age data suggest Mnz-3 crystallized before the formation of S_{T2}. The Mnz-3 asymmetric dextral tails (Figure S2) are most likely later microstructural modifications of an originally more symmetrical overgrowth, rather than primary growth related to the finite strain preserved in S_{T2}. It is possible that Mnz-3 originally grew in a north-northeast orientation during S_2 and developed a shape-preferred orientation by rotating into parallelism with S_{T2}. Importantly, these relationships show that the textural location and apparent grain shape of accessory minerals do not necessarily provide enough evidence on their own to confidently ascribe ages to deformation microstructures.

5.1.3 D_2 – 1.91 to 1.89 Ga cooling and exhumation

Retrograde cooling is inferred (Figure 7b) when comparing the crystallization of near-peak metamorphic monazite (Mnz-2 - WLsz^{pg}) at 1925 ± 4 Ma, retrograde zircon, Mnz-2 (Sb^{pg} - 1915 ± 4 Ma 1917 ± 8 Ma) and Mnz-3 (WLsz^{pg} - 1906 ± 6 Ma) with $^{40}Ar/^{39}Ar$ dates of biotite that yield 1911 to 1896 Ma cooling ages (Regis & Kellett, 2018). These broadly coeval ages correspond to a transition from high- (~810 °C modelled solidus) to low-temperature (~300 °C for biotite, McDougall & Harrison, 1999) conditions and suggest rapid cooling of the Snowbird domain between c. 1.93 and 1.90 Ga. This cooling likely accompanied decompression within the sillimanite stability field since kyanite is not observed in the sample. This is supported by the presence of late muscovite, sillimanite (fibrolite), biotite, and ilmenite in the Sb^{Pg}-M_3 retrograde assemblage. Other metamorphic U-Pb zircon ages from Snowbird metasedimentary rocks in the Dodge-Snowbird domain yield 1910 ± 7 Ma (Martel et al., 2008) and c. 1910 Ma (Ashton et al., 2017a), which are coeval (within error) with the zircon age of 1915 ± 4 Ma (Thiessen et al., 2017), further supporting the interpretation that anatexis and subsequent cooling and decompression was broadly synchronous across the entirety of the domain.

The north-northeast striking axial planar foliation (S_2) that developed in association with km-scale folding (F_2) of the Dodge-Snowbird domain (Figure 2) has been dated by low-Y monazite at 1904 ± 9 Ma (Martel et al., 2008) and c. 1900 Ma (Williams and Jercinovic, 2012). These ages are within error of our Sb^{pg} Mnz-2 population (1917 ± 8 Ma) and the WLsz^{pg} Mnz-3 population (1906 ± 6 Ma), and are consistent with crystallization after substantial garnet growth. In the WLsz^{pg}, it is plausible that Mnz-2 grew during north-northeast striking foliation development (S_2) as part of regional east-west directed compression and folding (Figure 12), whereas Mnz-3 may represent a local heating and monazite growth episode. Since this F_2 folding occurred coevally with exhumation (Figure 7), but prior to

extension documented by the WLsz, we consider this an early phase of unroofing resulting from combined uplift and erosion.

5.2 P-T-t-D evolution of the Wholdaia Lake shear zone

A new Lu-Hf date of 1873 ± 5 Ma (Figure 9c) significantly improves the precision of the Lu-Hf date that was previously determined for the $WLsz^{MG}$-M_2 assemblage in this particular domain (1870 ± 40 Ma; Thiessen et al., 2019). The new Lu-Hf date is within error of the U-Pb ages for titanite (1881 ± 9 Ma) and recrystallized zircon (1890 ± 33 Ma) from the same $WLsz^{MG}$-M_2 assemblage (Thiessen et al., 2018). Zirconium-in-titanite thermometry, coupled with apatite-in-garnet barometry compared with prior petrologic modelling (Figure 9a), indicates P-T conditions of 9.5 to 11.0 kbar and 820 to 850 °C for the $WLsz^{MG}$-M_2 assemblage. The simplest explanation is that the Lu-Hf date of 1873 ± 5 Ma represents an age for $WLsz^{MG}$-M_2 garnet that was either newly formed, or that developed by complete recrystallization, and chemical and isotope re-equilibration of the coarse $WLsz^{MG}$-M_1 garnet that is still found in low-strain enclaves M_1 (2111 ± 3 Ma; Thiessen et al., 2019).

It remains possible that $WLsz^{MG}$-M_2 garnet is older than the Lu-Hf date of 1873 ± 5 Ma and that this date represents diffusive re-equilibration of the Lu-Hf isotope systematics during and after $WLsz^{MG}$-M_2. Ascribing this to diffusive loss of Hf is not tenable since early investigations into Lu-Hf closure systematics of garnet (Scherer, Cameron, & Blichert-Toft, 2000; Smit, Scherer, & Mezger, 2013) indicate that for the given grain size (c. 0.5 mm) and an estimated conservative average cooling rate of 10–20 °C/Myr—calculated assuming coeval cooling of $WLsz^{MG}$-M_2 with the WLsz footwall (Train-Firedrake domain)—whole-grain loss of radiogenic Hf would require temperatures of c. 900 °C. This result is strikingly similar to the high estimates one would obtain using recent experimentally

determined Hf diffusion parameters (930–950 °C; Bloch et al., 2020). Although these rocks never attained such temperatures, the faster diffusivity of Lu and attendant age skewing also needs to be considered. For the given grains, experimentally determined Lu diffusivities indicate that Lu concentrations may be re-equilibrated on the grain-scale above 820–860°C, which is essentially the estimated peak temperature for $WLsz^{MG}$-M_2; it may even occur at lower temperatures, if results from Lu diffusion experiments done at 1 atm can be extrapolated to geologically relevant pressures (Bloch et al., 2020). Although garnet likely underwent some degree of diffusive Lu exchange with its matrix during and following $WLsz^{MG}$-M_2, it still remains questionable whether this actually changed the average Lu concentration of $WLsz^{MG}$-M_2 garnet and, by extension, the bulk-grain Lu/Hf values and Lu-Hf age. If bulk-grain Lu/Hf values were affected, the effects are expected to be larger in $WLsz^{MG}$-M_2 garnet rather than $WLsz^{MG}$-M_1 garnet purely by merit of its order-of-magnitude smaller grain size. However, $WLsz^{MG}$-M_2 garnet shows similar if not identical average Lu concentrations, as well as a similar range in Lu concentrations as the $WLsz^{MG}$-M_1 garnet grains (Thiessen et al., 2019). It cannot be excluded that the composition of $WLsz^{MG}$-M_2 garnet was different to begin with and that diffusive exchange caused a net change in this composition such that it coincidentally became similar to that of $WLsz^{MG}$-M_1. It is, however, much more plausible that Lu concentrations of $WLsz^{MG}$-M_1 and $WLsz^{MG}$-M_2 garnet were initially similar—both reflecting the equilibrium partitioning of Lu during equilibration with the assemblage in which they occur—and that Lu diffusion relaxed some of the zoning, having no resolvable net effect on grain-average Lu concentration and bulk-grain Lu content.

This would be expected if 1) Lu diffusivity in natural garnet is much slower than experiments suggest, perhaps operating by a different mechanism, 2) there was no strong core-versus-rim zoning and Lu partition coefficients are not as temperature-sensitive in the temperature regime of diffusive Lu exchange as they are expected and modelled to be, or 3) Lu diffusive transport was strongly matrix-

diffusion limited. The latter could be indicated by the fact that strong changes (increases) in Lu concentration are only observed at resorbed rims of large $WLsz^{MG}$-M_1 garnet grains, where garnet dissolution caused Lu to accumulate and, by law of equilibrium element partitioning, forced local re-uptake of Lu into the remaining garnet. Regardless which of these applied, it would appear that bulk-grain Lu contents of $WLsz^{MG}$-M_2 garnet, and hence the Lu-Hf age obtained for this material, most likely represents an initial state and that the age of 1873 ± 5 Ma represents the garnet-growth stage of $WLsz^{MG}$-M_2.

The data from the various $WLsz^{MG}$-M_2 phases, together provide a robust P-T-t-D constraint for the development of the S_{T1} gneissosity. These new data combined with the modelled garnet mode isopleths (Figure S3) for $WLsz^{MG}$-M_2 demonstrate that high-grade conditions and garnet growth at 1873 ± 5 Ma must have involved burial in order to generate the $WLsz^{MG}$-M_2 assemblage. This new data differs from the prior interpretation that S_{T1} in the WLsz, which has ambiguous kinematic relationships, underwent high-grade conditions associated with extensional exhumation processes (e.g., Thiessen et al., 2018).

5.3 Juxtaposition of crustal domains

The data indicate that the P-T-t-D history of rocks within the WLsz differs from that of the Dodge-Snowbird domain. Formation of S_2 and F_2 in the latter occurred at c. 1.93–1.90 Ga at peak conditions of 9.0 to 10.5 kbar and 810 to 830 °C (this work; Martel et al., 2008) and cooled through temperatures of ~300 °C ($^{40}Ar/^{39}Ar$ biotite) by 1891 ± 7 Ma (Regis and Kellett, 2018). By contrast, $WLsz^{MG}$ deformation and metamorphism reached 9.5 to 11 kbar and 820 to 850 °C at 1873 ± 5 Ma indicating a significant P-T break (>30 km depth and >500 °C) across the eastern WLsz at 1873 Ma.

Also, the prograde, peak and exhumation related cycle documented in the Dodge-Snowbird domain is not recorded in $WLsz^{MG}$. The sample instead records high-grade deformation well after substantial unroofing of the hanging wall Dodge-Snowbird domain.

A model that could explain the differences between these domains is provided in Figure 12. It is suggested that burial-related S_{T1} in the $WLsz^{MG}$ represents footwall deformation in a thrust-sense structure that is now the site of the WLsz. Distributed, compression related (S_2 & F_2) exhumation (uplift and erosion) in the hanging wall Dodge-Snowbird domain between 1.93 and 1.87 Ga would be contemporaneous with burial and high-grade footwall metamorphism in $WLsz^{MG}$-M_2 at 1873 ± 5 Ma. This high-grade S_{T1} footwall was retrogressed to Hbl-Bt-bearing mylonite within the extensional S_{T2} of the WLsz, which was subsequently crosscut by numerous 1.87 to 1.86 Ga felsic dykes (Thiessen et al., 2017, 2018). Thus, substantial exhumation of ~10 kbar rocks to mid crustal levels is documented during D_2 in the Dodge-Snowbird domain at 1.91 Ga and during D_3 within the WLsz between 1.87 and 1.86 Ga.

Exhumation of the footwall to the WLsz, the Train-Firedrake domain (Figure 13), resulted in the formation of voluminous granodiorite migmatite at 1.84 to 1.81 Ga (Ashton, Card, Heaman, & Coolican, 1999; Ashton et al., 2009; Davis et al., 2015; Regis et al., 2017b), which postdates the 1.87 to 1.86 Ga transtensional strain documented within S_{T2}. Although these processes are not reflected in the age record of the WLsz, magnetic patterns within the migmatite-bearing Train-Firedrake domain deflect dextrally into the western margin of the WLsz. This would imply strain accommodation by this shear zone persisted after c. 1.86 Ga. A lower age bracket for this deformation is provided by hornblende and biotite $^{40}Ar/^{39}Ar$ ages (c. 1.84 to 1.78 Ga; Regis and Kellett, 2018), which date cooling and exhumation in the footwall after migmatization was complete. It remains unclear whether the T-t curve of the WLsz

merges with the rapid unroofing experienced by the hanging wall or with slower unroofing documented in the footwall (Figure 7b).

5.4 Regional extent of the Snowbird Orogen in the Southeast Rae craton

5.4.1 Beaverlodge and Zemlak domains

Our data illustrate the development of S_1 and S_2 between c. 1.94 to 1.90 Ga within the Dodge-Snowbird domain, which matches P-T-t-D constraints documented in the 2.2 to 2.0 Ga upper Murmac Bay Group within the Beaverlodge and eastern Zemlak domains (Figure 13) ~100–200 km to the southwest (Figure 1). Although a single clockwise P-T loop occurred between 1.94 to 1.90 Ga, the orthogonal relationship between S_1 and S_2 suggests that two distinct compressional stress regimes acted on the southeast Rae cratonic margin prior to extensional unroofing. These two orthogonal stresses have been suggested to result from northeast-vergent Taltson orogenesis and followed by northwest-vergent Snowbird orogenesis (Bethune et al., 2013; Card, Bethune, Davis, Rayner, & Ashton, 2014; Martel et al., 2008). Our results coupled with regional considerations are broadly consistent with this two-sided orogenic model since the uniformity of the prograde clockwise P-T-t-D histories along this margin could be argued to reflect near-synchronicity between these two orogenic stages. It is also plausible that the difference in orientation bewteen D_1 and D_2 represents a switch in boundary conditions derived from a single orogenic episode along the southeastern Rae margin. This latter scenario is plausible in that there is little evidence for 1.94 to 1.90 Ga burial metamorphism immediately west of our study area towards the Taltson Orogen (see Berman et al., 2013a; Davis et al., 2015; Regis et al., 2017b). Furthermore, 2.4 to 2.3 Ga cooling ages ($^{40}Ar/^{39}Ar$ Bt and Hbl) are preserved within 50 km east of the Taltson Orogen's

magmatic belt (Nolan and Porter domains, Figure 1) in the South Rae of Northwest Territories (Banks, 1980; Koster and Baadsgaard, 1970; Lowdon, Stockwell, Tipper, & Wanless, 1963; Regis and Kellett, 2018). This suggests that Taltson related reworking of the southwestern Rae margin was spatially restricted and may not have been the driver of S_1 deformation at 1.94 to 1.93 Ga within the Dodge-Snowbird or even the Beaverlodge or Zemlak domains.

5.4.2 Tantato domain

Despite abundant evidence for an orogenic cycle along the southeast Rae craton margin between 1.94 and 1.89 Ga (e.g., Berman et al., 2007; Bethune et al., 2013; Martel et al., 2008; this work), interpretations from the Tantato domain are that 1.9 Ga metamorphism therein (D_2) relates to far-field stress and mafic underplating in an intracontinental setting (e.g., Dumond et al., 2015, 2017; Flowers et al., 2006a, 2008; Regan et al., 2014, 2017a, 2017b). Since high P-T conditions at 1.9 Ga are documented within the Tantato, Dodge-Snowbird and Beaverlodge domains (Figure 13), we suggest these domains have a shared orogenic history at 1.9 Ga. Considering the majority of evidence for D_1 burial at 1.9 Ga is derived from younger c. 2.0 Ga metasedimentary units (e.g., Bethune et al., 2013; Martel et al., 2008; this work), the apparent lack of a 1.9 Ga D_1 burial history in the Tantato domain may be due to the absence of these young metasedimentary rocks that best record this event. Combined with other studies farther north (e.g., Berman, Davis, Aspler, & Chiarenzelli, 2002a; Berman, Davis, Ryan, Tella, & Brown, 2002b; Berman, Rayner, Sanborn-Barrie, & Whalen, 2013b; Mills et al., 2007; Regis et al., 2019; Sanborn-Barrie, Carr, & Thériault, 2001; Sanborn-Barrie, Camacho, & Berman, 2019), high P-T burial metamorphism appears to have affected the eastern Rae craton margin for over 1000 km at c. 1.9 Ga, which supports a Rae-Hearne collisional model at 1.9 Ga. Thus, we consider the collisional model to

provide a more feasible explanation than those invoking far-field stress and intracontinental orogenesis at 1.9 Ga (e.g., Mahan et al., 2008; Regan et al., 2014). If the Tantato domain underwent the same orogenic cycle as the broader southeast Rae craton margin (as we suggest it did), its younger exhumation, similar to the Train-Firedrake domain (Figure 13), remains a distinct characteristic.

5.4.3 Exhumation structures

The exhumation accommodating shear zones internal to the southeast Rae margin (WLsz, Cora Lake shear zone, and possibly the Striding mylonite belt) document compression at c. 1.90 Ga followed by extensional deformation at c. 1.88 to 1.86 Ga. However, the outermost craton bounding structure, the Legs Lake shear zone of the Snowbird Tectonic Zone, has documented thrust-sense (west over east) kinematics at c. 1.85 Ga and possibly older (Mahan et al., 2003, 2006b). This illustrates that the extensional collapse of the Snowbird Orogen, or the Snowbird phase of the Trans-Hudson orogeny, was centered on the highest-pressure domains immediately prior to 1.85 Ga when a switch to far-field regional convergence (e.g., Rivers, 2009) affected the eastern edge of the craton margin. This convergence may be attributed to the <1.87 Ga closure of ocean domains and beginning of collision between the Superior and Sask to the composite Hearne-Rae cratons as is interpreted 1700 km farther north in the Rae craton (e.g., Berman et al., 2002b; Carson et al., 2004; Pehrsson, Berman, & Davis, 2013; Wodicka, St-Onge, Corrigan, Scott, & Whalen, 2014), which together suggests a complex polyorogenic hinterland of the Trans-Hudson Orogen. This raises the question of whether other domains in the South Rae 250 km farther west of the Snowbird Tectonic Zone (e.g., Regis et al., 2017b), which exhumed between c. 1.9 and 1.8 Ga (Regis and Kellett, 2018), underwent burial and thickening related

to c. 1.93 and/or 1.85 convergence or if they only experienced unroofing related to collapse of the Snowbird Orogen.

6 CONCLUSIONS

The Paleoproterozoic orogenic and exhumation history along the southeastern Rae craton margin in Northwest Territories is complex due to multiple overprinting thermotectonic events. In order to better understand 1.9 Ga orogenesis along this margin we use combined field analysis, new structural and prior regional observations, and microstructural, geochemical and geochronologic analysis. D_1 occurred between 1.94 and 1.93 Ga and involves burial of metasedimentary rocks within the Dodge-Snowbird domain (deposited at 2.2–2.0 Ga), prograde metamorphism and development of east-southeast trending structures (S_1, F_1). Peak P-T conditions within these metasedimentary units occurred at c. 1.93 Ga when rocks reached pressures of c. 8 to 10 kbar and temperatures of 830 °C. D_2 involved the development of north-northeast trending open folds and associated axial planar cleavage (S_2, F_2) between 1.93 and 1.90 Ga. Compression during D_2 appears to have been synchronous with exhumation and cooling in the Dodge-Snowbird domain based on petrologic modelling presented herein. Later progression of D_2 is documented in the north-northeast striking WLsz as a thrust-sense gneissic foliation (S_{T1}) at 1873 ± 5 Ma at conditions of 10 to 11 kbar and 835 to 865 °C, which occurred after the hanging wall Dodge-Snowbird domain had already cooled to below 300 °C. Further exhumation and greenschist to amphibolite facies extensional shearing (D_3) occurred between 1.87 and 1.86 Ga and was followed by footwall unroofing until c. 1.80 Ga.

Our work suggests that metamorphism along the southeast Rae craton may not be simply divided into a 1.93 Ga Taltson orogenic phase and a 1.90 Ga Snowbird orogenic phase (e.g., Bethune et al.,

2013). Rather, the distinct metamorphic and structural events between 1.94 and 1.85 Ga can be interpreted as the result of a single, longer-lived Snowbird orogenic cycle that corresponds with burial, peak metamorphic, extensional and exhumation events with changing boundary conditions. This analysis is supported by the clockwise P-T loop recorded in this work and along ~1000 km of the southeast Rae craton margin as well as old cooling ages within the southwest Rae craton basement adjacent to the Taltson orogen. The sinistral transpressional strain and presence of an arc, as may be predicted by the collision model (e.g., Berman et al., 2007), could be tested further by conducting additional integrated analysis of the terranes and their bounding shear zones. Likewise, such research may enable further assessment of the effects of any far-field stress on the overall system, especially when applied to the regions proximal to the possible locus of these stresses (e.g., Taltson Orogen, Great Slave Lake shear zone); this may also provide insight into the apparent lack of coeval reworking within supposed intervening crustal blocks.

ACKNOWLEDGMENTS

Funding was provided by a Geo Mapping for Energy and Minerals 2 National Resources Canada bursary and by the Northwest Territories Geological Survey to Thiessen, by a Natural Sciences and Engineering Research Council grant to Gibson (03808), a Natural Sciences and Engineering Research Council grant (04080) and the Canadian Foundation of Innovation and BC Knowledge Development Fund (229814) to Smit. Thank you to Mike Williams and Mike Jercinovic for providing elemental monazite maps, to Andrew Kylander-Clark for helping acquire titanite data and to Jamie Cutts for assistance with collecting Lu-Hf isotope ratios. An earlier version of this manuscript benefited from constructive comments by Kathryn Bethune and Greg Dumond and from discussions with Brendan Dyck and David Corrigan. We thank reviewers Kevin Mahan and Félix Gervais for

greatly improving the clarity of the discussion and our arguments. We also acknowledge editor Donna Whitney for efficient handling of this manuscript.

CONFLICT OF INTEREST

All authors declare no conflicts of interest.

REFERENCES

Allmendinger, R.W., Cardozo, N., & Fisher, D. (2012). Structural geology algorithms: Vectors and tensors in structural geology. Cambridge University Press.

Ashley, K.T., Barkoff, D.W., & Steele-MacInnis, M. (2017). Barometric constraints based on apatite inclusions in garnet. *American Mineralogist*, 102(4), 743–749.

Ashley, K.T., Steele-MacInnis, M., Bodnar, R.J., & Darling, R.S. (2016). Quartz-in-garnet inclusion barometry under fire: Reducing uncertainty from model estimates. *Geology*, 44(9), 699–702.

Ashton, K., Knox, B., Card, C., Rayner, N., Davis, B., Heaman, L., & Creaser, R. (2017a). Synthesis of U-Pb and Sm-Nd geochronological results from the Dodge Domain, southeastern Rae Province: *in* Summary of Investigations 2017, Volume 2, Saskatchewan Geological Survey, Saskatchewan Ministry of the Economy, Miscellaneous Report 2017-4.2, Paper A-12, 31p.

Ashton, K., Knox, B., Rayner, N., Creaser, R., & Bethune, K. (2017b). New U-Pb and Sm-Nd results from the Tantato Domain, southeastern Rae Province, Saskatchewan: *in* Summary of Investigations 2017, Volume 2, Saskatchewan Geological Survey, Saskatchewan Ministry of the Economy, Miscellaneous Report 2017-4.2, Paper A-14, 27p.

Ashton, K.E., Knox, B., Bethune, K.M., & Rayner, N. (2007b). Geochronological update and basement geology along the northern margin of the Athabasca Basin east of Fond-du-Lac (NTS 74O/06 and /07), southeastern Beaverlodge-southwestern Tantato domains, Rae 40 Province. In: Summary of Investigations 2007, vol. 2, Sask. Geol. Surv., Sask. Energy and Resources, Misc. Rep. 2007-4.2, CD-ROM, Paper A-9, 22p.

Ashton, K.E., (2009). Compilation bedrock geology, Tazin Lake, NTS area 74N; Saskatchewan Ministry and Resources, Map 246A (1:250 000 scale map).

Ashton, K.E., Card, C.D., Davis, W., & Heaman, L.M. (2007a). New U-Pb zircon age dates from the Tazin Lake map area (NTS 74N): in Summary of Investigations 2007, Volume 2, Saskatchewan Geological Survey, Saskatchewan Ministry of Energy and Resources, Misc. Rep. 2007-4.2, CD-ROM, Paper A-11, 8p.

Ashton, K.E., Card, C.D., Heaman, L.M., & Coolican, J. (1999). Rae Northeast: Analytical update and new field results from the north-central Train Lake Domain: *in* Summary of Investigations 1999, Volume 2, Saskatchewan Geological Survey, Sask. Energy Mines, Misc. Rep. 99-4.2.

Ashton, K.E., Hartlaub, R.P., Bethune, K.M., Heaman, L.M., & Niebergail, G. (2013). New depositional age constraints for the Murmac Bay group of the southern Rae Province, Canada: *Precambrian Research*, 232, 70–88.

Ashton, K.E., Rayner, N.M., & Bethune, K.M. (2009). Meso- and Neoarchean granitic magmatism, Paleoproterozoic (2.37 Ga and 1.93 Ga) metamorphism and 2.17 Ga provenance ages in a Murmac Bay Group pelite; U-Pb SHRIMP ages from the Uranium City area; *in* Summary of Investigations 2009, Volume 2, Saskatchewan Geological Survey, Sask. Ministry of Energy and Resources, Misc. Rep. 2009-4.2, Paper A-5, 9p.

Ashton, K.E., Rayner, N.M., Heaman, L.M., & Creaser, R.A. (2014). New Sm-Nd and U-Pb Ages from the Zemlak and South-Central Beaverlodge Domains: A Case for Amalgamated Taltson Basement Complex and Proto-Rae Cratonic Blocks within the Rae Province of Northwestern Saskatchewan; *in* Summary of Investigations 2014, Volume 2, Saskatchewan Geological Survey, Sask. Ministry of the Economy, Misc. Rep. 2014-4.2, Paper A-6, 28p.

Auzanneau, E., Schmidt, M.W., Vielzeuf, D., & Connolly, J.A.D. (2010). Titanium in phengite: a geobarometer for high temperature eclogites. *Contributions to Mineralogy and Petrology*, 159, 1–24.

Baldwin, J.A., Bowring, S.A., & Williams, M.L. (2003). Petrological and geochronological constraints on high pressure, high temperature metamorphism in the Snowbird tectonic zone, Canada. *Journal of Metamorphic Geology*, 21, 81–98.

Baldwin, J.A., Bowring, S.A., Williams, M.L., & Williams, I.S. (2004). Eclogites of the Snowbird tectonic zone: Petrological and U-Pb geochronological evidence for Paleoproterozoic high-pressure metamorphism in the western Canadian Shield. *Contributions to Mineralogy and Petrology*, 147, 528–548.

Banks, C.S. (1980). Geochronology, general geology and structure of Hill Island Lake-Tazin Lake areas; unpublished MSc thesis, University of Alberta, Canada.

Barkoff, D.W., Ashley, K.T., & Steele-MacInnis, M. (2017). Pressures of skarn mineralization at Casting Copper, Nevada, USA, based on apatite inclusions in garnet. *Geology*, 45(10), 947–950.

Barkoff, D.W., Ashley, K.T., Guimarães Da silva, R., Mazdab, F.K., & Steele-MacInnis, M. (2019). Thermobarometry of Three Skarns in the Ludwig Area, Nevada, Based On Raman Spectroscopy and Elastic Modeling of Mineral Inclusions in Garnet. *The Canadian Mineralogist*, 57(1), 25–45.

Berman, R.G., Davis, W.J., & Pehrsson, S. (2007). The collisional Snowbird tectonic zone resurrected: growth of Laurentia during the 1.9 Ga accretionary phase of the Trans-Hudson orogeny. *Geology*, 35, 911–914.

Berman, R.G., Davis, W.J., Aspler, L.B., & Chiarenzelli, J.R. (2002a). SHRIMP U-Pb ages of multiple metamorphic events in the Angikuni Lake area, western Churchill Province, Nunavut: Radiogenic and Isotopic Studies, Report 15; Geological Survey of Canada, Current Research 2002-F3, 9p.

Berman, R.G., Davis, W.J., Ryan, J.J., Tella, S., & Brown, N. (2002b). In situ SHRIMP U-Pb geochronology of Barrovian facies-series metasedimentary rocks in the Happy lake and Josephine River supracrustal belts: implications for the Paleoproterozoic architecture of the northern Hearne

domain, Nunavut: Radiogenic and Isotopic Studies, Report 15; Geological Survey of Canada, Current Research 2002-F4, 14p.

Berman, R.G., Pehrsson, S., Davis, W.J., Ryan, J.J., Qui, H., & Ashton, K.E. (2013a). The Arrowsmith orogeny: Geochronological and thermobarometric constraints on its extent and tectonic setting in the Rae craton, with implications for pre-Nuna supercontinent reconstruction. *Precambrian Research*, 232, 44–69.

Berman, R.G., Rayner, N., Sanborn-Barrie, M., & Whalen, J. (2013b). The tectonometamorphic evolution of Southampton Island, Nunavut: insight from in situ SHRIMP dating of monazite growth from lower amphibolite to granulite facies. *Precambrian Research*, 232, 140–166.

Bethune, K.M., Berman, R.G., Rayner, N., & Ashton, K.E. (2013). Structural, petrological and U-Pb SHRIMP geochronological study of the western Beaverlodge domain: Implications for crustal architecture, multi-stage orogenesis and the extent of the Taltson orogen in the SW Rae craton, Canadian Shield. *Precambrian Research*, 232, 89–118.

Bizzarro, M., Baker, J. A., & Ulfbeck, D. (2003). A new digestion and chemical separation technique for rapid and highly reproducible determination of Lu/Hf and Hf isotope ratios in geological materials by MC-ICP-MS. *Geostandards and Geoanalytical Research*, 27, 133–145.

Blichert-Toft, J., Boyet, M., Télouk, P., & Albarède, F. (2002). Sm-Nd and Lu-Hf in eucrites and the differentiation of the HED parent body. *Earth and planetary Science Letters*, 204, 167–181.

Blichert-Toft, J., Chauvel, C., & Albarède, F. (1997). Separation of Hf and Lu for high-precision isotope analysisof rock samples by magnetic sector-multiple collector ICP-MS. *Contributions to Mineralogy and Petrology*, 127, 248–260.

Bloch, E.M., Jollands, M.C., Devoir, A., Bouvier, A-S, Ibanez-Mejia, & Baumgartner, L.P. (2020). Multispecies diffusion of yttrium, rare earth elements and hafnium in garnet. *Journal of Petrology*, egaa055, https://doi.org/10.1093/petrology/egaa055

Bracciali, L., Parrish, R.R., Horstwood, M.S., Condon, D.J., & Najman, Y. (2013). U-Pb LA-(MC)-ICP-MS dating of rutile: New reference materials and applications to sedimentary provenance. *Chemical Geology*, 347, 82–101.

Card, C.D., Bethune, K.M., Davis, W.J., Rayner, N., & Ashton, K.E. (2014). The case for a distinct Taltson orogeny: Evidence from northwest Saskatchewan, Canada. *Precambrian Research*, 255, 245–265.

Cardozo, N., & Allmendinger, R.W. (2013). Spherical projections with OSXStereonet. *Computers & Geosciences*, 51, 193–205.

Carson, C.J., Berman, R.G., Stern, R.A., Sanborn-Barrie, M., Skulski, T., & Sandeman, H.A. (2004). Age constraints on the Paleoproterozoic tectonometamorphic history of the Committee Bay region, western Churchill Province, Canada: evidence from zircon and in situ monazite SHRIMP geochronology. *Canadian Journal of Earth Sciences*, 41, 1049–1076.

Coggon, R., & Holland, T.J.B. (2002). Mixing properties of phengitic micas and revised garnet-phengite thermobarometers. *Journal of Metamorphic Geology*, 20(7), 683–696.

Connolly, J.A.D. (1990). Multivariable phase diagrams: An algorithm based on generalized thermodynamics. *American Journal of Science*, 290, 666–718.

Connolly, J.A.D. (2009). The geodynamic equation of state: what and how. *Geochemistry, Geophysics, Geosystems*, 10.

Corfu, F., Hanchar, J.M., Hoskin, P.W., & Kinny, P. (2003). Atlas of zircon textures. *Reviews in mineralogy and geochemistry*, 53(1), 469–500.

Corrigan, D. (2012). Paleoproterozoic crustal evolution and tectonic processes: Insights from the LITHOPROBE program in the Trans-Hudson orogen, Canada: Chapter 4 In Tectonic Styles in Canada: The LITHOPROBE Perspective. Edited by J.A. Percival, F.A. Cook, and R.M., Clowes. Geological Association of Canada, Special Paper 49, pp. 237–284.

Davis, W.J., Pehrsson, S.J., & Percival, J.A. (2015). Results of a U-Pb zircon geochronology transect across the southern Rae craton, Northwest Territories, Canada: Geological Survey of Canada, Open File 7655.

Diener, J.F.A., Powell, R., White, R.W., & Holland, T.J.B. (2007). A new thermodynamic model for clino- and orthoamphiboles in the system Na_2O-CaO-FeO-MgO-Al_2O_3-SiO_2-H_2O-O. *Journal of Metamorphic Geology*, 25, 631–56.

Dumond, G., Goncalves, P., Williams, M.L., & Jercinovic, M.J. (2010). Subhorizontal fabric in exhumed continental lower crust and implications for lower crustal flow: Athabasca granulite terrane, western Canadian Shield. *Tectonics*, 29, 1–32.

Dumond, G., Goncalves, P., Williams, M.L., & Jercinovic, M.J. (2015). Monazite as a monitor of melting, garnet growth and feldspar recrystallization in continental lower crust. *Metamorphic Geology*, 33, 735–762.

Dumond, G., McLean, N., Williams, M.L., Jercinovic, M.J., & Bowring, S.A. (2008). High-resolution dating of granite petrogenesis and deformation in a lower crustal shear zone: Athabasca granulite terrane, western Canadian Shield. *Chemical Geology*, 254, 175–196.

Dumond, G., Williams, M.L., Baldwin, J.A., & Jercinovic, M.J. (2017). Backarc origin for Neoarchean ultrahigh-temperature metamorphism, eclogitization, and orogenic root growth. *Geology*, 45, 943–946.

Flowers, R.M., Bowring, S.A., Mahan, K.H., & Williams, M.L. (2006a). Timescales and significance of high-pressure, high-temperature metamorphism and mafic dyke anatexis, Snowbird tectonic zone, Canada. *Contribution to Mineralogy and Petrology*, 151, 558–581.

Flowers, R.M., Bowring, S.A., Mahan, K.H., Williams, M.L., & Williams, I.S. (2008). Stabilization and reactivation of cratonic lithosphere from the lower crustal record in the western Canadian shield. *Contributions to Mineralogy and Petrology*, 156, 529–549.

Flowers, R.M., Mahan, K.H., Bowring, S.A., Williams, M.L., Pringle, M.S., & Hodges, K.V. (2006b). Multistage exhumation and juxtaposition of lower continental crust in the western Canadian Shield: Linking high-resolution U-Pb and $^{40}Ar/^{39}Ar$ thermochronometry with pressure-temperature-deformation paths. *Tectonics*, 25.

Garber, J.M., Hacker, B.R., Kylander-Clark, A.R.C., Stearns, M., & Seward, G. (2017). Controls on trace element uptake in metamorphic titanite: implications for petrochronology. *Journal of Petrology*, 58(6), 1031–1057.

Gervais, F., & Crowley, J.L. (2017). Prograde and near-peak zircon growth in a migmatitic pelitic schist of the southeastern Canadian Cordillera. *Lithos*, 282, 65-81.

Green, E., Holland, T., Powell, R. (2007). An order-disorder model for omphacitic pyroxenes in the system jadeite-diopside-hedenbergite-acmite, with applications to eclogitic rocks. *American Mineralogist*, 92, 1181–9.

Guiraud, M., & Powell, R. (2006). P–V–T relationships and mineral equilibria in inclusions in minerals. *Earth and planetary Science Letters*, 244, 683–694.

Hanmer, S. (1993). unpublished structural data from Wholdaia Lake.

Hanmer, S., Williams, M., & Kopf, C. (1995). Modest movements, spectacular fabrics in an intracontinental deep-crustal strike-slip fault: Striding-Athabasca mylonite zone, NW Canadian Shield. *Journal of Structural Geology*, 17, 493–507.

Hartlaub, R.P., Chacko, T., Heaman, L.M., Creaser, R., Ashton, K.E., & Simonetti, A. (2005). Ancient (Paleo- to Mesoarchean) crust in the Rae Province, Canada: evidence from Sm-Nd and U-Pb constraints. *Precambrian Research*, 141, 137–153.

Hartlaub, R.P., Heaman, L.M., Ashton, K.E., & Chacko, T. (2004). The Archean Murmac Bay Group: evidence for a giant archean rift in the Rae Province, Canada. *Precambrian Research*, 131(3-4), 345–372.

Hartlaub, R.P., Heaman, L.M., Chacko, T., & Ashton, K.E. (2007). Circa 2.3-Ga magmatism of the Arrowsmith Orogeny, Uranium City Region, Churchill Craton, Canada. *Journal of Geology*, 115, 181–195.

Hayden, L.A., Watson, E.B., & Wark, D.A. (2008). A thermobarometer for sphene (titanite). *Contributions to Mineralogy and Petrology*, 155(4), 529–540.

Hoffman, P.F. (1988). United plates of America, the birth of a craton: Early Proterozoic assembly and growth of Laurentia. *Annual Review of Earth and planetary Sciences*, 16, 543–603.

Hofmann, A.E., Baker, M.B., & Eiler, J.M. (2014). Sub-micron-scale trace-element distributions in natural zircons of known provenance: implications for Ti-in-zircon thermometry. *Contributions to Mineralogy and Petrology*, 168:1057.

Holland, T., Baker, J., & Powell, R. (1998). Mixing properties and activity-composition relationships of chlorites in the system MgO-FeO-Al_2O_3-SiO_2-H_2O. *European Journal of Mineralogy*, 10, 395–406

Holland, T., & Powell, R. (1996). Thermodynamics of order-disorder in minerals. 2. Symmetric formalism applied to solid solutions. *American Mineralogist*, 81, 1425.

Holland, T., & Powell, R. (2001). Calculation of phase relations involving haplogranitic melts using an internally consistent thermodynamic dataset. *Journal of Petrology*, 42, 673–83

Holland, T.J.B., & Powell, R. (2011). An improved and extended internally consistent thermodynamic dataset for phases of petrological interest, involving a new equation of state for solids. *Journal of Metamorphic Geology*, 29, 333–383.

Holland, T.J.B., & Powell, R.T.J.B. (1998). An internally consistent thermodynamic data set for phases of petrological interest. *Journal of metamorphic Geology*, 16, 309–343.

Hoskin, P.W., & Schaltegger, U. (2003). The composition of zircon and igneous and metamorphic petrogenesis. *Reviews in mineralogy and geochemistry*, 53(1), 27–62.

Kelsey, D.E., Clark, C., & Hand, M. (2008). Thermobarometric modelling of zircon and monazite growth in melt-bearing systems: examples using model metapelitic and metapsammitic granulites. *Journal of Metamorphic Geology*, 26, 199–212.

Kiss, F., & Coyle, M. (2012). Aeromagnetic survey of the South Rae Craton, Northwest Territories: Geological Survey of Canada, Open File 7122-7125, scale 1:100 000.

Knox, B.R. (2012). A geological investigation of the south-central Beaverlodge Domain, southern Rae Province: with emphasis on the nature and timing of deformation and associated metamorphism; unpublished MSc thesis, University of Regina, Canada, 173p.

Knox. B., Card, C.D., & Ashton, K.E. (2011). Bedrock geology of the Grollier Lake area, southeastern Dodge Domain (parts of NTS 74P/11, /12, /13, and /14): in Summary of Investigations 2011, Volume 2, Saskatchewan Geological Survey, Sask. Ministry of Energy and Resources, Misc. Rep. 2011-4.2, Paper A-3, 13p

Kohn, M.J., Corrie, S.L., & Markley, C. (2015). The fall and rise of metamorphic zircon. *American Mineralogist*, 100, 897–908.

Koster, F., & Baadsgaard, H. (1970). On the geology and geochronology of northwestern Saskatchewan, I. Tazin Lake region. *Canadian Journal of Earth Sciences*, 7, 919–930.

Lafrance, B., & Sibbald, T.I.I., (1997). The Grease River Shear Zone: Proterozoic Overprinting of the Archean Tantato Domain: *in* Summary of Investigations 1997, Saskatchewan Geological Survey, Sask. Energy Mines, Misc. Rep. 97-4.

Lagos, M., Scherer, E. E., Tomaschek, F., Münker, C., Keiter, M., Berndt, M. J., & Ballhaus, C. (2007). High precision Lu-Hf geochronology of Eocene eclogite-facies rocks from Syros, Cyclades, Greece. *Chemical Geology*, 243, 16–35.

Lowdon, J.A., Stockwell, C.H., Tipper, H.W., & Wanless, R.K. (1963). Age Determinations and Geological Studies; Geological survey of Canada, Paper p. 62–17.

Ludwig, K.R. (2005). User's Manual for ISOPLOT/3.27. A geochronological toolkit for Microsoft Excel, Berkeley Geochronology Center, Special Publication 4, 1–71.

Ludwig, K.R. (2003). Isoplot 3.00: A geochronological toolkit for Microsoft Excel: Berkeley Geochronology Center Special Publication, 4, 1-70.

Mahan, K.H., & Williams, M.L. (2005). Reconstruction of a large deep-crustal terrane: Implications for the Snowbird tectonic zone and early growth of Laurentia. *Geology*, 33, 385–388.

Mahan, K.H., Goncalves, P., Flowers, R., Williams, M.L., & Hoffman-Setka, D. (2008). The role of heterogeneous strain in the development and preservation of a polymetamorphic record in high-P granulites, western Canadian Shield. *Journal of Metamorphic Geology*, 26, 669–694.

Mahan, K.H., Goncalves, P., Williams, M.L., & Jercinovic, M.J. (2006a). Dating metamorphic reactions and fluid flow: application to exhumation of high-P granulites in a crustal-scale shear zone, western Canadian Shield. *Journal of Metamorphic Geology*, 24, 193–217.

Mahan, K.H., Williams, M.L., & Baldwin, J.A. (2003). Contractional uplift of deep crustal rocks along the Legs Lake shear zone, western Churchill Province, Canadian Shield. *Canadian Journal of Earth Sciences*, 40, 1085–1110.

Mahan, K.H., Williams, M.L., Flowers, R.M., Jercinovic, M.J., Baldwin, J.A., & Bowring, S.A. (2006b). Geochronological constraints on the Legs Lake shear zone with implications for regional exhumation of lower continental crust, western Churchill Province, Canadian Shield. *Contributions to Mineralogy and Petrology*, 152, 223–242.

Martel, E., & Pierce, K. (2006). An ArcView 3.x digital geological atlas of the Snowbird Lake area, NTS 65D; Northwest Territories Geoscience Office, NWT Open File 2006-02. Digital files and 2 maps, scale 1:125000.

Martel, E., van Breemen, O., Berman, R.G., & Pehrsson, S. (2008). Geochronology and tectonometamorphic history of the Snowbird Lake area, Northwest Territories, Canada: New insights into the architecture and significance of the Snowbird tectonic zone. *Precambrian Research*, 161, 201–230.

McDonough, M.R., McNicoll, V.J., Schetselaar, E.M., & Grover, T.W. (2000). Geochronological and kinematic constraints on crustal shortening and escape in two-sided oblique-slip collisional and magmatic orogen, Paleoproterozoic Taltson magmatic zone, northeastern Alberta: In Ross, G. (Ed.), The Lithoprobe-Alberta Basement Transect. *Canadian Journal of Earth Sciences*, 37, 1549–1573.

McDougall, I., & Harrison, T.M. (1999). Geochronology and Thermochronology of the $^{40}Ar/^{39}Ar$ method: Second edition, Oxford University Press, New York, NY, 269p.

Mills, A.J., Berman, R.G., Davis, W.J., Tella, S., Roddick, C., & Carr, S.H.S. (2007). Thermobarometry and geochronology of the Uvauk complex, a polymetamorphic Neoarchean and Paleoproterozoic segment of the Snowbird tectonic zone, Nunavut, Canada. *Canadian Journal of Earth Sciences*, 44, 245–266.

Münker, C., Weyer, S., Scherer, E.E., & Mezger, K. (2001). Separation of high field strength elements (Nb, Ta, Zr, Hf) and Lu from rock samples for MC-ICPMS measurements. *Geochemistry, Geophysics, Geosystems*, 2.

Newton, R.C., Charlu, T.V., & Kleppa, O.J. (1980). Thermochemistry of the high structural state plagioclases. *Geochimica et Cosmochimica Acta*. 44, 933–941.

Nicoli, G., Moyen, J.F., & Stevens, G. (2016). Diversity of burial rates in convergent settings decreased as Earth aged. *Scientific reports*, 6, 1–10.

Pehrsson, S.J., Berman, R.G., & Davis, W.J. (2013). Paleoproterozoic orogenesis during Nuna aggregation: a case study of reworking of the Rae craton, Woodburn Lake, Nunavut. *Precambrian research*, 232, 167–188.

Ply, D. (2016). Resolving Paragneiss Provenance at Grollier Lake in the Athabasca Granulite Terrane, Western Canadian Shield [M.Sc. Thesis]: University of Arkansas, 44 p.

Pouchou, J.L., & Pichoir, F. (1985). PAP $\phi(\rho Z)$ procedure for improved quantitative microanalysis. *Microbeam Analysis*, 104–106.

Rayner, N.M., and Stern, R.A. (2002). Improved sample preparation method for SHRIMP analysis of delicate mineral grains exposed in thin sections: Natural Resources Canada, Geological Survey of Canada.

Regan, S.P., Williams, M.L., Chiarenzelli, J.R., Grohn, L., Mahan, K.H. & Gallagher, M. (2017a). Isotopic evidence for Neoarchean continuity across the Snowbird Tectonic Zone, western Churchill Province, Canada. *Precambrian Research*, 300, 201–222.

Regan, S.P., Williams, M.L., Leslie, S., Mahan, K.H., Jercinovic, M.J. & Holland, M.E. (2014). The Cora Lake shear zone, Athabasca granulite terrane, an intraplate response to far-field orogenic processes during the amalgamation of Laurentia. *Canadian Journal of Earth Sciences*, 51, 877–901.

Regan, S.P., Williams, M.L., Mahan, K.H., Dumond, G., Jercinovic, M.J., & Orlandini, O.F. (2017b). Neoarchean arc magmatism and subsequent collisional orogenesis along the eastern Rae domain, western Churchill Province: Implications for the early growth of Laurentia. *Precambrian Research*, 294, 151–174.

Regis, D., Acosta-Gongora, P., Davis, W.J., Knox, B., Pehrsson, S.J., Martel, E., & Hulbert, L. (2017a). Evidence for Neoarchean Ni-Cu-bearing mafic intrusions along a major lithospheric structure: A case study from the south Rae craton (Canada). *Precambrian Research*, 302, 312–339.

Regis, D., & Kellett, D.A. (2018). $^{40}Ar/^{39}Ar$ hornblende and biotite cooling ages for metamorphic rocks from the southern Rae craton, Northwest Territories: Geological Survey of Canada Open File 8438, 73 p.

Regis, D., Davis, W.J., Ryan, J.J., Berman, R.G., Pehrsson, S., Joyce, N.L., & Sandeman, H.A. (2019). Multiple burial-exhumation episodes revealed by accessory phases in high-pressure granulite-facies rock (Rae craton, Nunavut, Canada). *Contributions to Mineralogy and Petrology*, 174(41).

Regis, D., Martel, E., Davis, W.J., & Pehrsson, S.J. (2017b). U-Pb zircon geochronology of metaplutonic rocks across the southern Rae province, Northwest Territories: Geological Survey of Canada, Open File 8254.

Rivers, T. (2009) The Grenville Province as a large hot long-duration collisional orogen–insights from the spatial and thermal evolution of its orogenic fronts. *Geological Society, London, Special Publications*, 327, 405–444.

Roscoe, S.M., & Miller, A.R. (1986). Outliers of porphyritic alkaline volcanic rocks of the Christopher Island Formation at Snowbird Lake, N.W.T.: *in* Current Research, Part B, Geological Survey of Canada, Paper 86-1B, p. 679–683.

Sanborn-Barrie, M., Camacho, A., & Berman, R.G. (2019). High-pressure, ultrahigh-temperature 1.9 Ga metamorphism of the Kramanituar Complex, Snowbird Tectonic Zone, Rae Craton, Canada. *Contributions to Mineralogy and Petrology*, 174(14).

Sanborn-Barrie, M., Carr, S., & Thériault, R. (2001). Geochronological constraints on metamorphism, magmatism and exhumation of deep-crustal rocks of the Kramanituar Complex, with implications for the Paleoproterozoic evolution of the Archean western Churchill Province, Canada. *Contributions to Mineralogy and Petrology*, 141, 592–612.

Scherer, E.E., Cameron, K.L., & Blichert-Toft, J. (2000). Lu–Hf garnet geochronology: closure temperature relative to the Sm–Nd system and the effects of trace mineral inclusions. *Geochimica et Cosmochimica Acta*, 64(19), 3413-3432.

Scherer, E.E., Münker, C., & Mezger, K. (2001). Calibration of the Lutetium-Hafnium Clock. *Science*, 293, 683–687.

Schmidt, C., & Ziemann, M.A. (2000). In situ Raman spectroscopy of quartz: A pressure sensor for hydrothermal diamond-anvil cell experiments at elevated temperatures. *American Mineralogist*, 85(11-12), 1725–1734.

Schouwink, P., Miletich, R., Ullrich, A., Glasmacher, U.A., Trautmann, C., Neumann, R., & Kohn, B.P. (2010). Ion tracks in apatite at high pressures: the effect of crystallographic track orientation on

the elastic properties of fluorapatite under hydrostatic compression. *Physics and Chemistry of Minerals*, 37(6), 371–387.

Shiels, C., Partin, C.A., & Eglington, B.M. (2016). Provenance approaches in polydeformed metasedimentary successions: Determining nearest neighboring cratons during the deposition of the Paleoproterozoic Murmac Bay Group. *Lithosphere*, 8, 519–532.

Smit, M.A., Scherer, E.E., & Mezger, K. (2013). Lu-Hf and Sm-Nd garnet geochronology: Chronometric closure and implications for dating petrological processes. *Earth and planetary Science Letters*, 381, 222–233.

Söderlund, U., Patchett, P.J., Vervoort, J.D., & Isachsen, C.E. (2004). The ^{176}Lu decay constant determined by Lu–Hf and U–Pb isotope systematics of Precambrian mafic intrusions. *Earth and planetary Science Letters*, 219, 311–324.

Stern, R.A., & Berman, R.G. (2001). Monazite U–Pb and Th–Pb geochronology by ion microprobe, with an application to *in situ* dating of an Archean metasedimentary rock. *Chemical Geology*, 172(1-2), 113–130.

Stern, R.A. (1997). The GSC sensitive high resolution ion microprobe (SHRIMP): analytical techniques of zircon U–Th–Pb age determinations and performance evaluation. Geological Survey of Canada, Current Research.

Tajcmanová, L., Connolly, J.A.D., & Cesare, B. (2009). A thermodynamic model for titanium and ferric iron solution in biotite. *Journal of Metamorphic Geology*, 27, 153–64.

Taylor, F.C., Bostock, H.H., and Baer, A.J. (1970). Geology, Wholdaia Lake, District of McKenzie, Geological Survey of Canada, "A" Series Map 1199A, 1 sheet.

Taylor, R.J.M., Clark, C., Harley, S.L., Kylander-Clark, A.R.C., Hacker, B.R., & Kinny, P.D. (2017). Interpreting granulite facies events through rare earth element partitioning arrays. *Journal of Metamorphic Geology*, 35, 759–775.

Taylor, R.J.M., Harley, S.L., Hinton, R.W., Elphick, S., Clark, C., & Kelly, N.M. (2015). Experimental determination of REE partition coefficients between zircon, garnet and melt: a key to understanding high-T crustal processes. *Journal of Metamorphic Geology*, 33, 231–248.

Thiessen, E.J., Gibson, H.D., Regis, D., & Pehrsson, S.J. (2018). Deformation and extensional exhumation of 1.9 Ga high-pressure granulites along the Wholdaia Lake shear zone, south Rae craton, Northwest Territories, Canada. *Lithosphere*, 10, 641–661.

Thiessen, E.J., Gibson, H.D., Regis, D., Pehrsson, S.J., Cutts, J.A., & Smit, M.A. (2019). High-grade metamorphism flying under the radar of accessory minerals. *Geology*, 47(6), 568–572.

Thiessen, E.J., Regis, D., & Gibson, H.D. (2017). U-Pb zircon geochronology of the Paleoproterozoic Wholdaia Lake shear zone, south Rae craton, Northwest Territories: Geological Survey of Canada, Open File 8193, 27 p.

Thompson, J.B., & Hovis, G.L. (1979). Entropy of Mixing in Sanidine. *American Mineralogist*, 64, 57–65.

Tomkins, H.S., Powell, R., & Ellis, D.J. (2007). The pressure dependence of the zirconium-in-rutile thermometer. *Journal of Metamorphic Geology*, 25, 703–713.

Vermeesch, P. (2018). IsoplotR: a free and open toolbox for geochronology. Geoscience Frontiers, 9, 1479–1493.

Watson, E.B., Wark, D.A., & Thomas, J.B. (2006). Crystallization thermometers for zircon and rutile. *Contributions to Mineralogy and Petrology*, 151, 413.

White, R.W., Powell, R., Holland, T.J.B., & Worley, B.A. (2000). The effect of TiO_2 and Fe_2O_3 on metapelitic assemblages at greenschist and amphibolite facies conditions: mineral equilibria calculations in the system K_2O-FeO-MgO-Al_2O_3-SiO_2-H_2O-TiO_2-Fe_2O_3. *Journal of Metamorphic Geology*, 18, 497–511.

White, R.W., Powell, R., & Holland, T.J.B. (2001). Calculation of partial melting equilibria in the system Na_2O-CaO-K_2O-FeO-MgO-Al_2O_3-SiO_2-H_2O (NCKFMASH). *Journal of Metamorphic Geology*, 19(2), 139-153.

Whitney, D.L., & Evans, B.W. (2010). Abbreviations for names of rock-forming minerals. *American Mineralogist*, 95, 185–187.

Williams, M.L., & Jercinovic, M.J. (2002). Microprobe monazite geochronology: putting absolute time into microstructural analysis. *Journal of Structural Geology*, 24, 1013–1028.

Williams, M.L., & Jercinovic, M.J. (2012). Tectonic interpretation of metamorphic tectonites: integrating compositional mapping, microstructural analysis and in situ monazite dating. *Journal of Metamorphic Geology*, 30, 739–752.

Williams, M.L., Jercinovic, M.J., & Terry, M.P. (1999). Age mapping and dating of monazite on the electron microprobe: Deconvoluting multistage tectonic histories. *Geology*, 27, 1023–1026.

Wodicka, N., St-Onge, M.R., Corrigan, D., Scott, D.J., & Whalen, J.B. (2014). Did a proto-ocean basin form along the southeastern Rae cratonic margin? Evidence from U-Pb geochronology, geochemistry (Sm-Nd and whole-rock), and stratigraphy of the Paleoproterozoic Piling Group, northern Canada. *GSA Bulletin*, 126, 1625–1653.

Yakymchuk, C. (2017). Behaviour of apatite during partial melting of metapelites and consequences for prograde suprasolidus monazite growth. *Lithos*, 274, 412–426.

Yakymchuk, C., & Brown, M. (2014). Behaviour of zircon and monazite during crustal melting. *Journal of the Geological Society, London*, 171, 465–479.

Yakymchuk, C., Clark, C., & White, R.W. (2017). Phase relations, reaction sequences and petrochronology. *Reviews in Mineralogy and Geochemistry*, 83(1), 13–53.

Figure Captions

Figure 1. Precambrian geology of the western Canadian shield centered on the South Rae craton and highlighting Archean provinces, Proterozoic orogens and relevant Proterozoic basins. Dotted outline in top left image corresponds to larger map. Dashed outline on larger map corresponds to area shown in Figure 2. Thin black lines delineate tectonized domain boundaries. Abbreviations are TO = Taltson Orogen, SBO = Snowbird Orogen, THO = Trans-Hudson Orogen, BBfz = Black Bay fault zone, GRsz = Grease River shear zone, CLsz, Cora Lake shear zone, LLsz = Legs Lake shear zone, Csz = Chipman shear zone, AB = Alberta, SK = Saskatchewan, NWT = Northwest Territories, W = Wholdaia Lake, S = Snowbird Lake.

Figure 2. a) Simplified geology map of the southeastern Rae craton margin in Northwest Territories and Saskatchewan. New samples are yellow circles and prior samples discussed in text are blue circles (Ashton et al., 2017a; Martel et al., 2008; Ply, 2016). Boxes outline the area depicted in b and d. Abbreviations are WL = Wholdaia Lake, SbL = Snowbird Lake, SL = Selwyn Lake, KL = Kasba Lake, Smb = Striding mylonite belt, Csz = Chipman shear zone, GRsz = Grease River shear zone, CLsz = Cora Lake shear zone, LLsz = Legs Lake shear zone. b, d). First derivative magnetic anomaly maps (Kiss and Koyle, 2012) are superimposed with regional foliations (thin black solid and dashed lines) to provide structural context for the samples. Thick black lines delineate the S_{T1} and S_{T2} domains in the Wholdaia Lake shear zone (WLsz) as drawn by Thiessen et al. (2018). c) Poles to planes (gneissic and mylonite foliations) for S_{T1} and S_{T2} within WLsz are plotted on equal area lower hemisphere projections (with Stereonet 9.5, Allmendinger, Cardozo, & Fisher, 2012; Cardozo & Allmendinger, 2013) and contoured (kamb) with a spacing interval of 2. Data are from this study, Taylor, Bostock, and Baer (1970), Hanmer (unpublished data), and Martel and Pierce (2006).

Figure 3. a) Outcrop photograph of the Snowbird Paragneiss sample (Sb^{Pg}) highlighting leucosome parallel to a penetrative foliation developed in the melanosome defined by Qz_1+Kfs_1+Grt_R+Sil_1+Bt_1+Rt. b) Plane polarized photomicrograph showing the general textural relationships of the sample. The dashed box is the garnet porphyroblast highlighted in Figure 6. c) Plane polarized photomicrograph showing the S_1 foliation defined by sillimanite, biotite, K-feldspar and quartz that wrap around garnet. d) Inclusion-poor garnet rims with lobate quartz-filled margins suggesting a melt phase was present during garnet growth. e) Cross polarized photomicrograph showing major matrix phases quartz and K-feldspar, portions of which may have crystallized from melt. f) Large rutile and corroded biotite within the matrix.

Figure 4. a) Gneissic foliation highlighting the $WLsz^{MG}$-M_2 domain that defines S_{T1}. b) Photomicrograph in plane polarized light showing the general textural relationships within the $WLsz^{MG}$-M_2 assemblage. c) plane polarized light photomicrograph highlighting titanite crystals, some of which are fully encased by garnet and others share grain boundaries with garnet and clinopyroxene in the $WLsz^{MG}$-M_2 assemblage.

Figure 5. a) Outcrop of sample $WLsz^{Pg}$ (collected near head of hammer). The S_{T2} foliation is defined by compositional layering and leucosome. Hammer handle points to the north. b) Felsic dyke cutting the S_{T2} foliation dated at c. 1.87 Ga (Thiessen et al., 2017). c) Winged porphyroclasts illustrating dextral sense of shear (viewed looking down on outcrop) for S_{T2}. d) Plane polarized photomicrograph showing the general microstructures in $WLsz^{Pg}$ including resorbed garnet rims and rare sillimanite relicts. e) Cross-polarized photomicrograph of lower-grade phases defining S_{T2} that replace garnet and

exhibit dextral shear bands. f) Randomly oriented cordierite and muscovite that appear to have pseudomorphed a garnet porphyroblast.

Figure 6. a, d) Major and trace element zoning for the representative garnet porphyroblast from Sb^{Pg} in b, c, e, f. Major element profiles (a) and compositional maps (c, e, f) show only subtle major element zoning. The Si-map (e) and Ca-map (f) shows quartz and apatite inclusions in the garnet core. f) Mineral inclusions Qz_a, Qz_b and Ap_c were analyzed by Raman spectrometry to estimate entrapment pressures.

Figure 7. a) Equilibrium phase diagram for Sb^{Pg} highlighting a proposed P-T path. Phase assemblages are linked to a portion of the P-T-t cycle where Sb^{Pg}-M_1 represents early prograde growth (yellow line), Sb^{Pg}-M_2 is late prograde to peak (red field), and Sb^{Pg}-M_3 corresponds to the retrograde evolution (blue line). Yellow boxes represent mineral inclusion entrapment and rutile derived P-T estimates. b) Proposed temperature-time (T-t) paths for the hanging wall Dodge-Snowbird domain (Sb^{Pg} and $WLsz^{Pg}$), the Wholdaia Lake shear zone and the footwall Train-Firedrake domain with chronometers shown for reference. Two possible end-member T-t paths are shown for the WLsz that correspond to whether its cooling trajectory merged with that of its hanging wall or footwall. References for constraints used on deposition and cooling path: T2018 = Thiessen et al. (2018), R2017 = Regis et al., 2017b, R&K2018 = Regis and Kellett, (2018), and R&M1986 = Roscoe and Miller, (1986).

Figure 8. Monazite U-Pb ($^{207}Pb/^{206}Pb$) data, chemical maps and textural locations in Sb^{Pg}. A first order division of Mnz-1 and Mnz-2 populations is made using a distinct break in Y concentrations. At the far-right, a faceted Mnz-1 grain is situated within a Grt_C. The Mnz-1 population commonly occurs as

core domains or whole crystals within garnet and more rarely in the matrix. The Mnz-2 population commonly occurs as whole crystals or rim domains in the matrix. Spot size (black circles) is 10 μm in diameter. Images and textural locations of all monazite grains are presented in Figures S2–S3.

Figure 9. a) Equilibrium phase diagram and zone of phase mode isopleths for the stable $WLsz^{MG}$-M_2 assemblage from Thiessen et al. (2019). The new apatite-in-garnet barometric estimates and Zr-in-titanite temperature estimates are in yellow and blue, respectively. Phases in numbered fields are 1 = Grt+Cpx+Hbl+Pl+Rt+Ilm+Qz, 2 = Liq+Grt+Cpx+Hbl+Pl+Rt+Ilm+Qz, 3 = Liq+Grt+Cpx+Hbl+Pl+Ilm+Qz, 4 = Liq+Grt+Cpx+Hbl+Pl+Qz, 5 = Liq+Cpx+Pl+Ilm+Qz, 6 = Liq+Grt+Cpx+Opx+Pl+Ilm, 7 = Liq+Cpx+Opx+Pl+Ilm. b) QEMSCAN phase map showing representative apatite inclusions in garnet used for barometric analysis. c) Lu-Hf isochron for the $WLsz^{MG}$-M_2 assemblage. New analyses from this study are in yellow circles and prior analyses are in blue circles (Thiessen et al., 2019). d) Titanite U-Pb data plotted on an inverse (Tera-Wasserburg) concordia diagram highlighting two arrays that represent distinct common-Pb (Pb_C) reservoirs incorporated during crystallization. The 1881 ± 9 Ma age was calculated for the yellow array as a model-1 discordia regression with IsoplotR (Vermeesch, 2018) and corresponds with peak P-T conditions in the sample.

Figure 10. In the upper half of the figure, a first order division of monazite populations is based on Y concentrations. High-Y Mnz-1 typically occurs as whole crystals or core domains encased in garnet or as more rare core domains in the matrix. In the bottom half of the figure, low-Y Mnz-2 occurs mostly as core domains encased in younger Mnz-3 in the matrix. Mnz-3 occurs only in the matrix as a rimming phase or whole grains and has relatively high Th/U ratios. Spot size (black and yellow circles)

is 10 μm in diameter. Images and textural locations of all monazite grains are presented in Figures S1–S2.

Figure 11. Rare-earth element array plot showing the distribution of Yb (Zrn/Grt) and Yb/Gd (Zrn/Grt) for core and rim domains within zircon and garnet in Sb^{Pg}. The data are compared to experimentally determined equilibrium partitioning values (red circles) between zircon and garnet at 7 kbar (Taylor et al., 2015). The close overlap of experimental data with partition coefficients of metamorphic zircon rims and garnet rims suggests equilibrium between these phases.

Figure 12. Generalized structural evolution of the hanging wall Dodge-Snowbird domain and footwall Wholdaia Lake shear zone (view is looking to the southwest in order to visualize structures). Yellow circles represent samples that aid in visualizing the crustal movement during the distinct structural episodes. Note that although not depicted in the diagrams, erosion likely accompanied deformation of the D_2 stage in order to accommodate exhumation in this compressional regime.

Figure 13. Summary of geochronological data from crustal domains along the southeast Rae craton margin (data is from Ashton, 2009; Ashton, Card, Davis, & Heaman, 2007a; Ashton et al., 2007b, 2009, 2014, 2017a; Ashton, Knox, Rayner, Creaser, & Bethune, 2017b; Baldwin, Bowring, & Williams, 2003; Baldwin et al., 2004; Berman et al., 2013a; Bethune et al., 2013; Bracciali, Parrish, Horstwood, Condon, & Najman, 2013; Davis et al., 2015; Dumond et al., 2008, 2010, 2015; Flowers et al., 2006a, 2006b, 2008; Hartlaub, Heaman, Ashton, & Chacko, 2004; Mahan et al., 2006a, 2006b; Martel et al., 2008; Regis et al., 2017a, 2017b; Regis and Kellett, 2018; Regan et al., 2014, 2017a, 2017b; Shiels et

al., 2016; Thiessen et al., 2018, 2019; Williams and Jercinovic, 2002, 2012; Williams, Jercinovic, & Terry, 1999). D_1–D_3 are deformational events discussed herein and superimposed on the data.

Table Captions

Table 1. U-Pb SHRIMP monazite data

Table 2. Metamorphic assemblages and dated phases of samples with context of deformational stages

Table 1. U-Pb SHRIMP monazite data

Lab ID	Grain #	domain	U (ppm)	Th (ppm)	Th/U	Y (ppm)	err (%)	^{206}Pb* (ppm)	f(206)^{204} (%)	isotopic ratios									apparent ages (Ma)		
										^{208}Pb*/^{206}Pb*	err 1σ (%)	^{204}Pb/^{206}Pb*	err 1σ (%)	^{207}Pb*/^{235}U*	err 1σ (%)	^{206}Pb*/^{238}U*	err 1σ (%)	corr coef	^{207}Pb/^{206}Pb	err 1σ (Ma)	Disc. (%)
Snowbird Paragneiss (15ET273b) - NAD83 UTM zone 13 547899E 6718255N																					
11696-007.3	M24	2-m-w	1498	51506	35.5	253	9	436	0.234	10.4	0.34	1.5E-4	22	5.33	1.76	0.3385	1.65	0.9373	1869	11	-0.6
11696-007.2	M23	2-m-r	2703	43168	16.5	486	9	802	0.083	4.7	0.31	5.4E-5	22	5.52	1.57	0.3454	1.53	0.9736	1893	6	-1.2
11696-003.1	M14	2-m-w	1973	48677	25.5	287	9	576	0.116	7.2	0.31	7.6E-5	21	5.44	1.62	0.3401	1.57	0.9661	1897	8	0.6
11696-004.3	M16	2-m-w	2008	49520	25.5	247	9	598	0.186	7.4	0.37	1.2E-4	20	5.57	1.74	0.3467	1.65	0.9502	1904	10	-0.9
11696-001.2	M11	2-m-r	1324	45463	35.5	223	9	389	0.081	10.3	0.33	5.3E-5	30	5.50	1.79	0.3422	1.63	0.9102	1905	13	0.5
11696-007.1 dup	M23	2-m-r	1289	46059	36.9	243	9	373	0.157	11.0	0.35	1.0E-4	24	5.43	1.76	0.3373	1.67	0.9490	1906	10	2.0
11696-005.1	M19	2-m-w	1753	46214	27.2	193	9	498	0.165	8.0	0.31	1.1E-4	21	5.32	1.64	0.3307	1.57	0.9587	1907	8	3.9
11696-002.2	M12	2-m-r	1558	44537	29.5	227	9	468	0.161	8.5	0.30	1.0E-4	21	5.65	1.68	0.3500	1.61	0.9617	1911	8	-1.4
11696-005.2	M18	1-g-w	11632	40797	3.6	3289	10	3427	0.035	1.0	0.53	2.3E-5	17	5.54	2.44	0.3429	1.75	0.7184	1914	30	0.8
11696-004.4	M15	2-m-w	1642	44996	28.3	244	9	482	0.110	8.2	0.33	7.2E-5	23	5.53	1.92	0.3421	1.87	0.9738	1916	8	1.2
11696-004.2	M15	2-m-w	1679	45116	27.8	240	9	488	0.139	8.2	0.30	9.1E-5	20	5.48	1.62	0.3382	1.56	0.9647	1920	8	2.5
11696-005.3	M17	1-g-w	8301	44716	5.6	4031	9	2445	0.055	1.5	4.52	3.6E-5	17	5.56	1.70	0.3429	1.61	0.9433	1921	10	1.2
11696-001.1	M11	1-m-c	2930	41752	14.7	1346	9	885	0.103	4.3	0.27	6.7E-5	18	5.71	1.52	0.3517	1.49	0.9792	1922	6	-1.2
11696-004.1	M15	2-m-w	1574	40549	26.6	223	9	462	0.107	7.9	0.30	7.0E-5	22	5.55	1.62	0.3415	1.57	0.9665	1925	7	1.9
11696-006.2	M20	1-m-c	3425	22387	6.8	2849	9	991	0.098	2.0	1.22	6.4E-5	20	5.48	1.65	0.3370	1.48	0.9006	1925	13	3.2
11696-006.1	M20	2-m-r	3452	39238	11.7	266	9	1018	0.049	3.5	0.57	3.2E-5	23	5.59	1.68	0.3433	1.66	0.9869	1927	5	1.5
11696-002.1	M12	1-m-c	3491	43118	12.8	4338	9	1062	0.137	3.6	0.36	8.9E-5	19	5.77	1.61	0.3541	1.56	0.9686	1930	7	-1.5
11696-006.5	M20	2-m-r	2944	41155	14.4	261	9	845	0.077	4.4	0.29	5.0E-5	21	5.45	1.53	0.3341	1.50	0.9779	1930	6	4.3
11696-003.2	M13	2-m-w	2398	43628	18.8	313	9	711	0.183	5.5	0.39	1.2E-4	18	5.63	1.82	0.3451	1.60	0.8795	1931	16	1.2
11696-003.3	M13	2-m-w	3202	41370	13.4	272	8	971	0.077	3.8	0.33	5.0E-5	23	5.76	1.57	0.3529	1.53	0.9748	1931	6	-1.0
11696-007.1	M25	1-g-w	3905	41455	11.0	808	9	1142	0.026	3.2	0.27	1.7E-5	30	5.57	1.73	0.3404	1.71	0.9891	1936	5	2.8
11696-006.3	M21	1-g-w	13720	41991	3.2	1186	9	4070	0.026	0.9	0.42	1.7E-5	18	5.65	1.52	0.3453	1.52	0.9959	1937	2	1.5
11696-001.3	M11	1-m-c	3042	42118	14.3	2285	9	895	0.067	4.2	0.28	4.4E-5	21	5.62	1.72	0.3427	1.69	0.9844	1942	5	2.5
11696-006.4	M22	1-g-w	8898	31357	3.6	2208	9	2622	0.043	1.1	0.31	2.8E-5	18	5.63	1.77	0.3430	1.73	0.9767	1943	7	2.5
Wholdaia Lake shear zone Paragneiss (15ET258b) - NAD83 UTM zone 13 578775E 6763505N																					
11820-001.2	M1	3-m-r	4859	42704	9.1	1669	9	1440	0.041	2.6	0.26	2.7E-5	22	5.52	1.48	0.3451	1.46	0.9871	1895	4	-1.0
11820-005.1	M7	3-m-w	1324	66390	51.8	172	10	393	0.298	15.2	0.49	1.9E-4	17	5.55	1.71	0.3456	1.61	0.9418	1902	10	-0.7
11820-001.4	M1	3-m-r	3470	30289	9.0	1248	8	973	0.047	2.7	0.27	3.1E-5	21	5.24	1.47	0.3264	1.45	0.9855	1903	5	4.9
11820-005.3	M7	3-m-w	1309	62571	49.4	189	9	390	0.189	14.6	0.47	1.2E-4	19	5.58	1.69	0.3472	1.62	0.9534	1903	9	-1.1
11820-003.2	M3	3-m-r	3018	47118	16.1	1147	9	892	0.092	4.7	0.47	6.0E-5	22	5.54	1.59	0.3442	1.50	0.9432	1907	9	0.0
11820-002.2	M2	3-m-r	2830	43262	15.8	1317	9	828	0.072	4.6	0.50	4.7E-5	21	5.49	1.58	0.3405	1.50	0.9476	1909	9	1.2
11820-006.1	M8	3-m-r	3113	56808	18.9	688	10	925	0.090	5.5	0.25	5.9E-5	21	5.58	1.52	0.3458	1.48	0.9791	1913	6	-0.1
11820-006.2	M8	3-m-r	3142	62263	20.5	692	9	904	0.071	6.0	0.26	4.7E-5	21	5.42	1.71	0.3351	1.68	0.9825	1914	6	3.1
11820-005.2	M7	3-m-w	1461	56273	39.8	378	9	430	0.154	11.6	0.49	1.0E-4	20	5.54	1.64	0.3426	1.58	0.9609	1915	8	0.9
11820-006.3	M8	3-m-r	2953	66729	23.4	609	9	860	0.115	7.0	0.25	7.5E-5	20	5.48	1.54	0.3390	1.50	0.9746	1916	6	2.1
11820-004.4	M6	2-g-w	5257	54044	10.6	2342	9	1551	0.068	3.2	0.42	4.4E-5	21	5.58	1.48	0.3434	1.46	0.9846	1923	5	1.2
11820-002.1	M2	2-m-c	6980	13335	2.0	916	9	2026	0.019	0.6	0.43	1.2E-5	27	5.49	1.45	0.3380	1.44	0.9912	1924	3	2.8
11820-002.3	M2	2-m-c	6356	21919	3.6	874	9	1883	0.017	1.0	1.27	1.1E-5	28	5.61	1.68	0.3449	1.67	0.9936	1924	3	0.8
11820-006.6	M8	2-m-c	5266	39062	7.7	953	9	1523	0.040	2.3	1.19	2.6E-5	21	5.47	1.48	0.3367	1.46	0.9883	1925	4	3.2
11820-003.1	M3	2-m-c	4814	50311	10.8	1846	9	1422	0.076	3.2	0.28	4.9E-5	22	5.61	1.50	0.3438	1.47	0.9821	1932	5	1.6
11820-004.1	M4	1-g-w	3657	32005	9.0	9825	9	1109	0.081	2.5	0.90	5.3E-5	18	5.75	1.51	0.3532	1.49	0.9815	1927	5	-1.4
11820-001.3	M1	1-m-c	12980	44878	3.6	8155	9	3929	0.027	1.0	0.69	1.8E-5	20	5.75	1.61	0.3524	1.60	0.9959	1933	3	-0.8
11820-004.2	M4	1-g-w	5243	36540	7.2	9571	9	1569	0.048	1.9	1.75	3.1E-5	20	5.69	1.48	0.3484	1.46	0.9871	1933	4	0.4
11820-006.5	M10	1-g-c	3010	33814	11.6	9495	9	895	0.077	3.4	0.31	5.1E-5	20	5.65	1.70	0.3460	1.67	0.9828	1934	6	1.1
11820-006.4	M9	1-g-c	3706	34901	9.7	9116	8	1099	0.115	2.9	0.69	7.5E-5	20	5.65	1.94	0.3453	1.91	0.9843	1935	6	1.4
11820-001.1	M1	1-m-c	5823	46882	8.3	7266	9	1773	0.062	2.2	0.28	4.1E-5	17	5.81	1.46	0.3545	1.44	0.9891	1939	4	-1.0
11820-004.5	M5	1-g-c	3808	26087	7.1	10158	9	1123	0.016	2.1	0.53	1.0E-5	41	5.65	1.50	0.3433	1.48	0.9839	1946	5	2.6
11820-004.3	M5	1-g-c	3415	21339	6.5	9748	9	1039	0.057	1.9	0.37	3.7E-5	23	5.83	1.52	0.3541	1.49	0.9810	1947	5	-0.5

Lab ID follows the convention y.z; where y = grain number and z = spot number.
Grain # corresponds with images in supplementary file.
Uncertainties reported at 1s (%) and are calculated by numerical propagation of all known sources of error using Squid version 2.22. Errors in ages are 1s absolute in Ma.
$f(206)^{204}$ refers to mole percent of total ^{206}Pb that is due to common Pb, calculated using the ^{204}Pb-method; common Pb composition used is the surface blank
* refers to radiogenic Pb (corrected for common Pb)
Discordance relative to origin = 100 * (1-($^{206}Pb/^{238}U$ age)/($^{207}Pb/^{206}Pb$ age))
Calibration standard z8153; Age = 511.6 Ma; $^{206}Pb/^{238}U$ = 0.0826
Calibration secondary standards z3345; Age = 1821 Ma, and z2908; Age 1795 Ma
Domain notation: 1-3 = monazite domain, m = matrix hosted, g = encased in garnet, w = whole crystal, c = core, r = rim.

Table 2. Metamorphic assemblages and dated phases of samples with context of deformational stages

Samples	**Pre-D_1**	**D_1**	**D_2**		**D_3**	**post-D_3**
		1.94-1.93 Ga (S_1, F_1)	1.93-1.90 Ga (S_2, F_2)	1.87 Ga (S_{T1})	1.87-1.86 Ga (S_{T2})	<1.86 Ga
Sb^{Pg} (15ET273b)	Dep. Age <1.98 Ga	Sb^{Pg}-M_1 Sb^{Pg}-M_2 Mnz-1	Sb^{Pg}-M_3 Zrn, Mnz-2			
$WLsz^{MG}$ (15ET249b)	$WLsz^{MG}$-M_1 Grt-1 2.11 Ga			$WLsz^{MG}$-M_2 Grt, Ttn, Zrn		
$WLsz^{Pg}$ (15ET258b)	Dep. Age <2.0 Ga?	$WLsz^{Pg}$-M_1 Mnz-1	Mnz-2		$WLsz^{Pg}$-M_2 Zrn (dykes)	$WLsz^{Pg}$-M_3

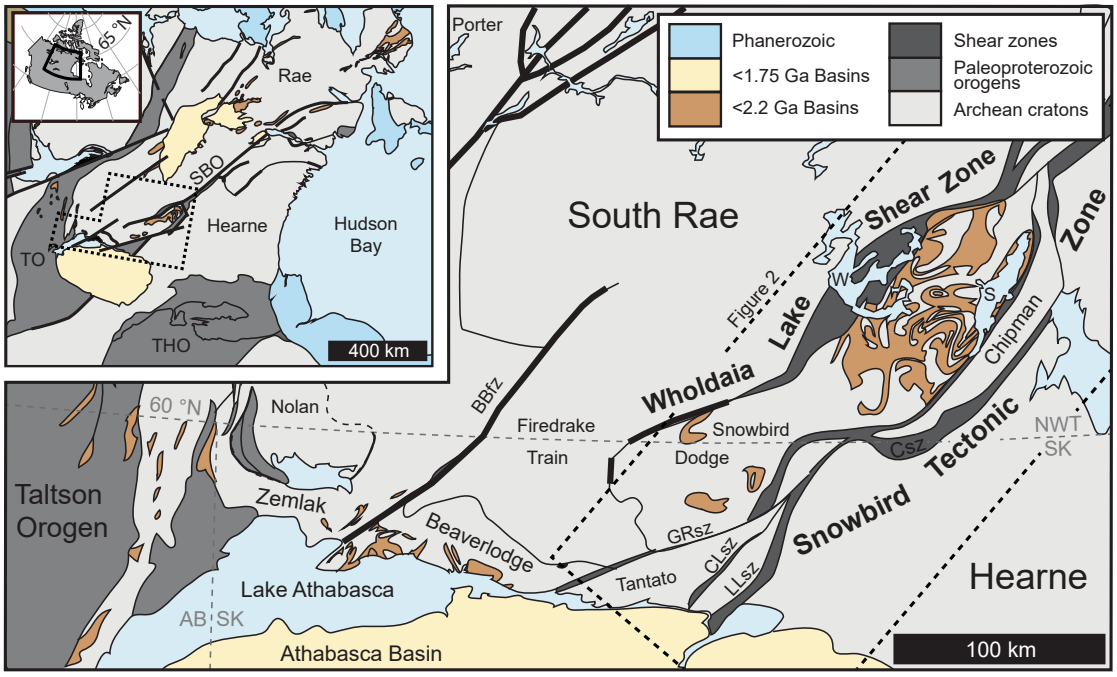
65 °N
Rae
SBO
Hearne
Hudson Bay
TO
THO
400 km
Porter
Phanerozoic
<1.75 Ga Basins
<2.2 Ga Basins
Shear zones
Paleoproterozoic orogens
Archean cratons
South Rae
Shear Zone
Zone
Figure 2
W
S
Lake
Wholdaia
Chipman
BBfz
60 °N
Nolan
Firedrake
Train
Snowbird
Dodge
Csz
Tectonic
NWT
SK
Taltson
Orogen
Zemlak
Beaverlodge
GRsz
CLsz
LLsz
Snowbird
Tantato
Hearne
Lake Athabasca
AB
SK
Athabasca Basin
100 km

Figure 1

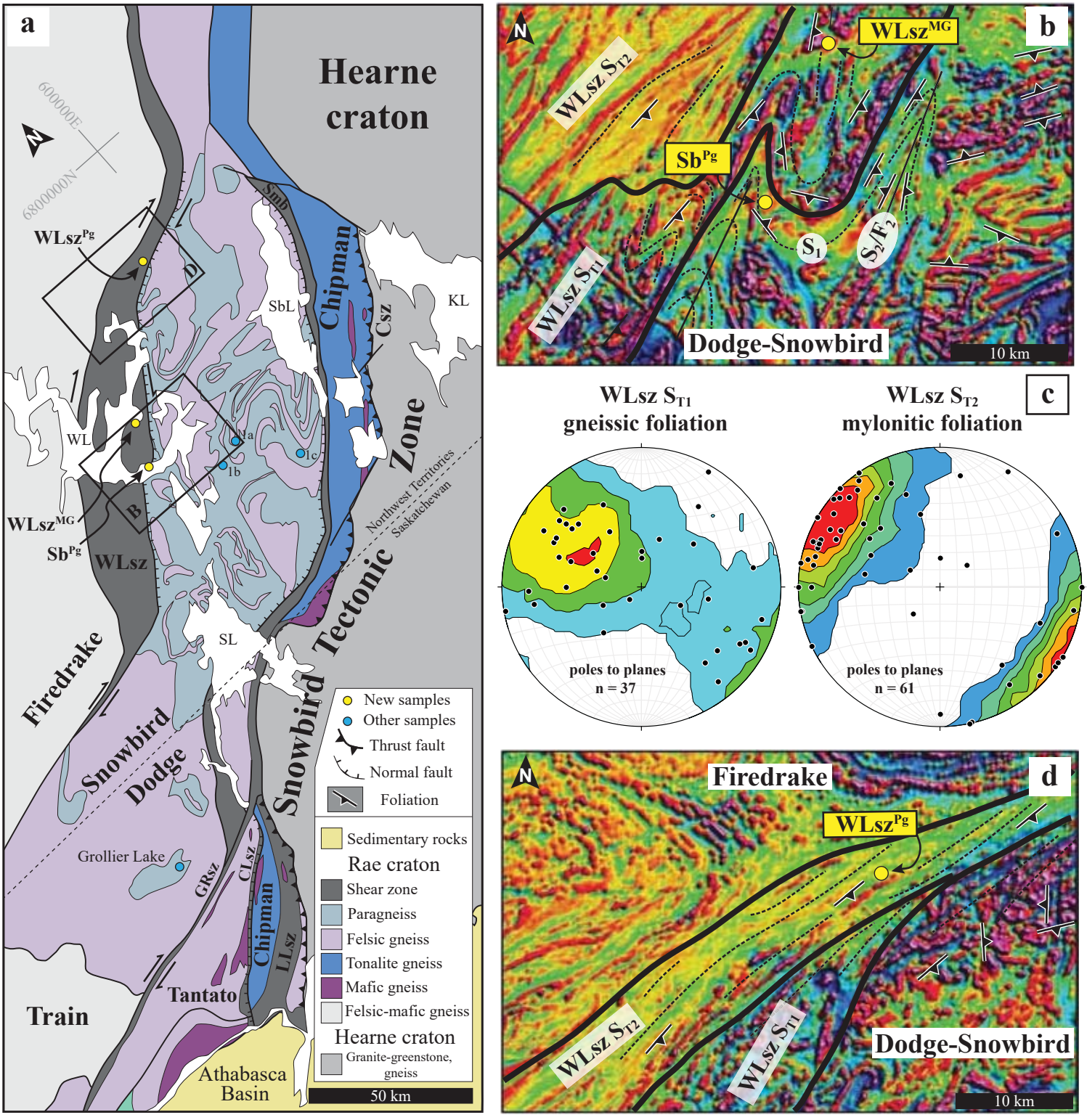
a
Hearne craton
600000E
6800000N
N
WLsz^Pg
D
SmbL
Chipman
SbL
Csz
KL
WL
Na
Ic
Ib
Zone
Northwest Territories
Saskatchewan
WLsz^MG
Sb^Pg
B
WLsz
Tectonic
Firedrake
SL
Snowbird
Dodge
Snowbird
Grollier Lake
GRsz
CLsz
Chipman
LLsz
Tantato
Train
Athabasca Basin
New samples
Other samples
Thrust fault
Normal fault
Foliation
Sedimentary rocks
Rae craton
Shear zone
Paragneiss
Felsic gneiss
Tonalite gneiss
Mafic gneiss
Felsic-mafic gneiss
Hearne craton
Granite-greenstone, gneiss
50 km
b
N
WLsz^MG
WLsz S_T2
Sb^Pg
S1
S2/F2
WLsz S_T1
Dodge-Snowbird
10 km
c
WLsz S_T1
gneissic foliation
WLsz S_T2
mylonitic foliation
poles to planes
n = 37
poles to planes
n = 61
d
N
Firedrake
WLsz^Pg
WLsz S_T2
WLsz S_T1
Dodge-Snowbird
10 km

Figure 2

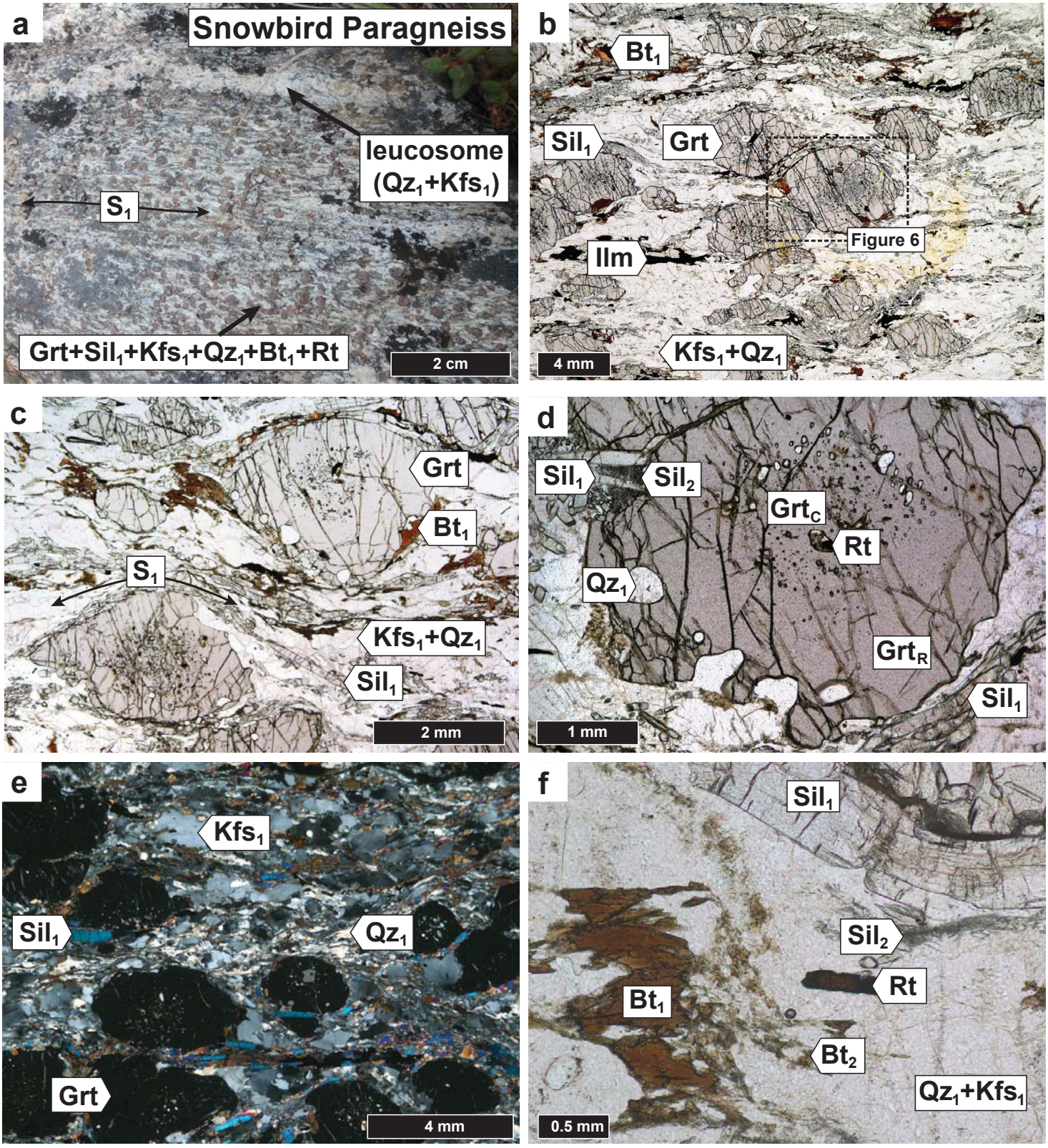
a
Snowbird Paragneiss
leucosome
(Qz1+Kfs1)
S1
Grt+Sil1+Kfs1+Qz1+Bt1+Rt
2 cm
b
Bt1
Sil1
Grt
Figure 6
Ilm
Kfs1+Qz1
4 mm
c
Grt
Bt1
S1
Kfs1+Qz1
Sil1
2 mm
d
Sil1
Sil2
GrtC
Rt
Qz1
GrtR
Sil1
1 mm
e
Kfs1
Sil1
Qz1
Grt
4 mm
f
Sil1
Sil2
Rt
Bt1
Bt2
Qz1+Kfs1
0.5 mm

Figure 3

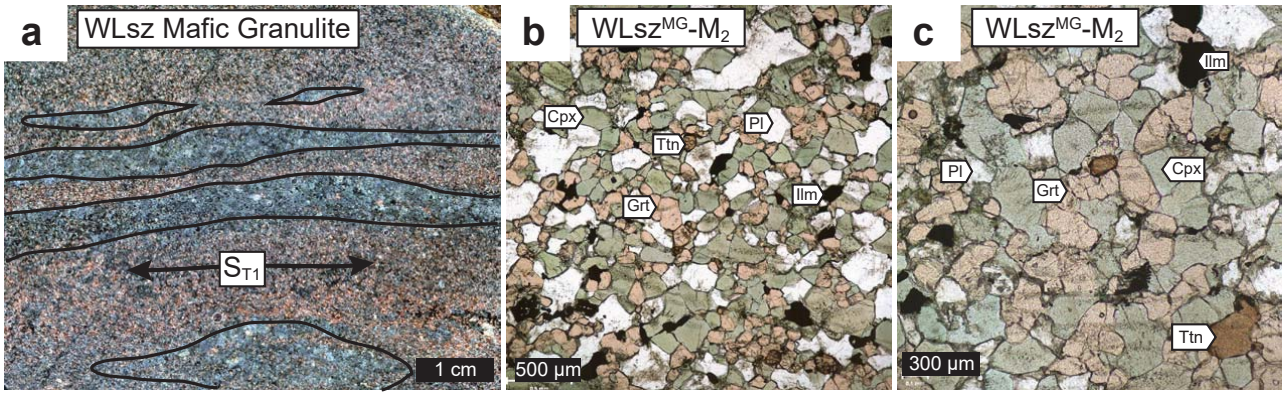
a
WLsz Mafic Granulite
S_{T1}
1 cm
b
WLsz^{MG}-M$_2$
Cpx
Pl
Ttn
Grt
Ilm
500 µm
c
WLsz^{MG}-M$_2$
Ilm
Pl
Cpx
Grt
Ttn
300 µm

Figure 4

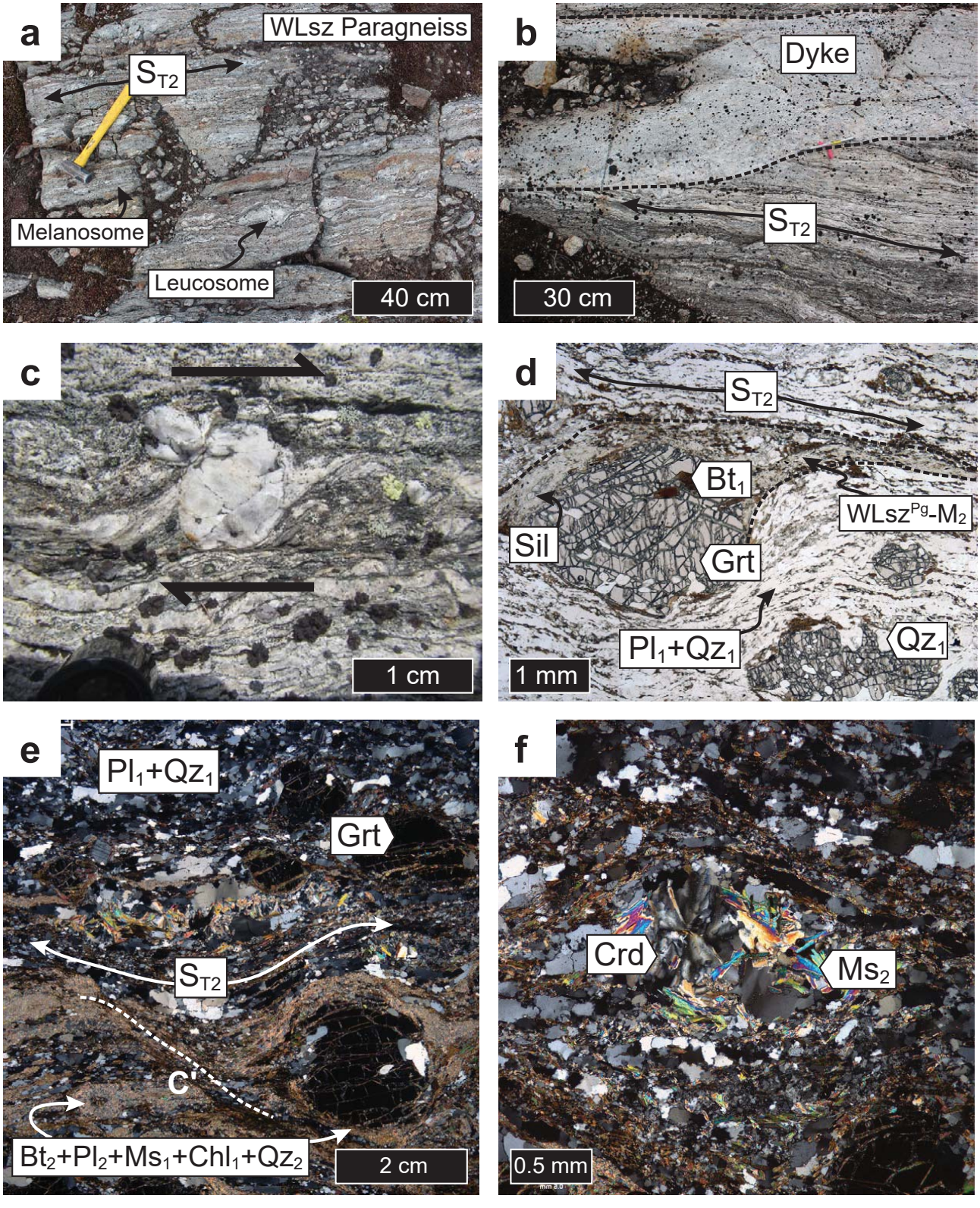
a
WLsz Paragneiss
S_{T2}
Melanosome
Leucosome
40 cm
b
Dyke
S_{T2}
30 cm
c
1 cm
d
S_{T2}
Bt_1
$WLsz^{Pg}$-M_2
Sil
Grt
Pl_1+Qz_1
Qz_1
1 mm
e
Pl_1+Qz_1
Grt
S_{T2}
c'
Bt_2+Pl_2+Ms_1+Chl_1+Qz_2
2 cm
f
Crd
Ms_2
0.5 mm

Figure 5

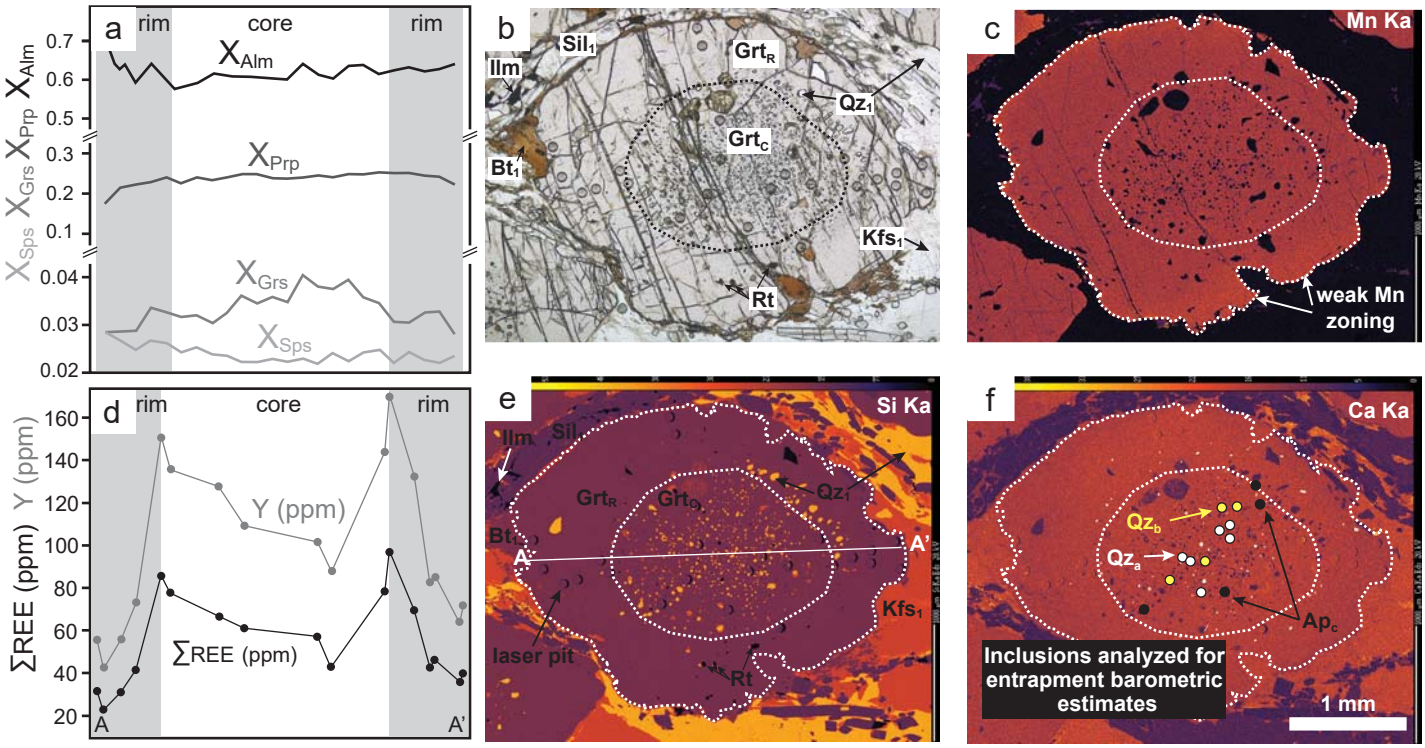
a
rim
core
rim
X_{Alm}
X_{Prp}
X_{Grs}
X_{Sps}
0.7
0.6
0.5
0.3
0.2
0.1
0.04
0.03
0.02
b
Sil_1
Ilm
Grt_R
Qz_1
Grt_C
Bt_1
Kfs_1
Rt
c
Mn Ka
weak Mn zoning
d
rim
core
rim
Y (ppm)
∑REE (ppm)
160
140
120
100
80
60
40
20
A
A'
e
Si Ka
Ilm
Sil
Grt_R
Grt_C
Qz_1
Bt_1
A
A'
Kfs_1
laser pit
Rt
f
Ca Ka
Qz_b
Qz_a
Ap_c
Inclusions analyzed for entrapment barometric estimates
1 mm

Figure 6

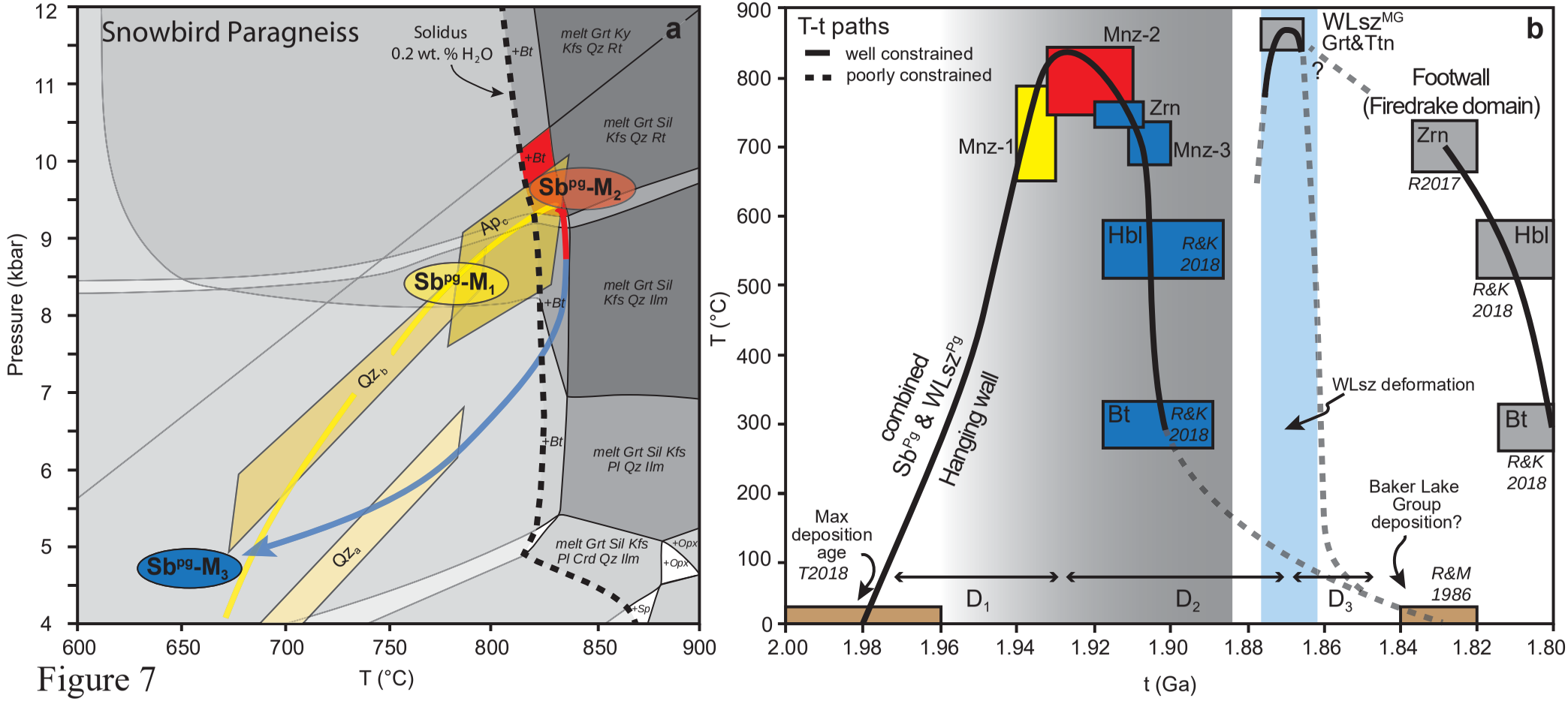
Snowbird Paragneiss
Solidus
0.2 wt. % H2O
+Bt
melt Grt Ky
Kfs Qz Rt
melt Grt Sil
Kfs Qz Rt
melt Grt Sil
Kfs Qz Ilm
melt Grt Sil Kfs
Pl Qz Ilm
melt Grt Sil Kfs
Pl Crd Qz Ilm
+Opx
+Sp
Sbpg-M2
Sbpg-M1
Sbpg-M3
Apc
QZb
QZa
a
Pressure (kbar)
T (°C)
T-t paths
well constrained
poorly constrained
Mnz-1
Mnz-2
Mnz-3
Zrn
Hbl
R&K
2018
Bt
combined
SbPg & WLszPg
Hanging wall
Max
deposition
age
T2018
D1
D2
D3
WLsz deformation
WLszMG
Grt&Ttn
?
Footwall
(Firedrake domain)
R2017
Baker Lake
Group
deposition?
R&M
1986
b
T (°C)
t (Ga)

Figure 7

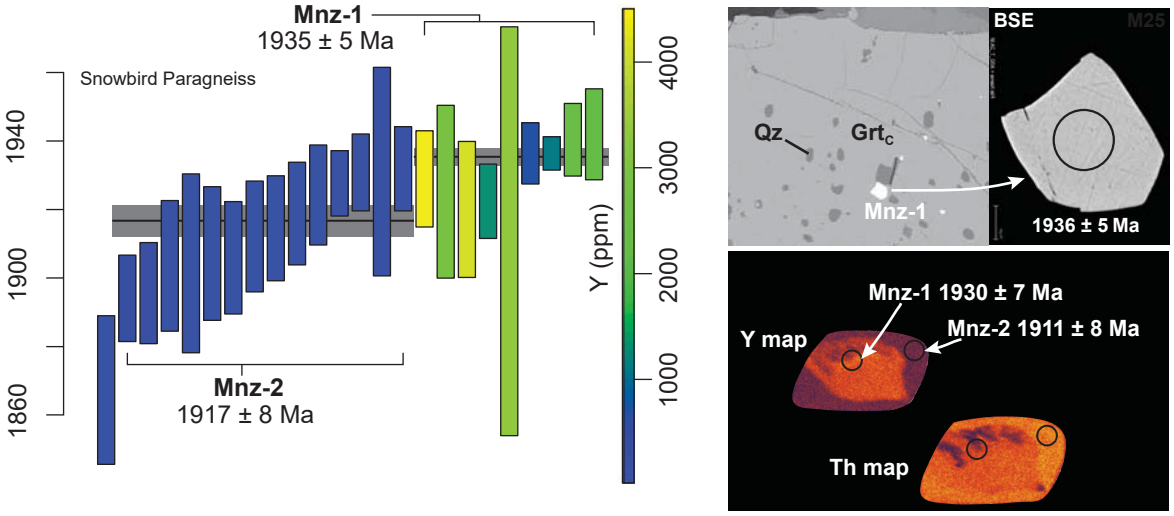
Mnz-1
1935 ± 5 Ma
Snowbird Paragneiss
1940
1900
1860
Mnz-2
1917 ± 8 Ma
Y (ppm)
4000
3000
2000
1000
Qz
Grt$_c$
Mnz-1
BSE
M25
1936 ± 5 Ma
Mnz-1 1930 ± 7 Ma
Mnz-2 1911 ± 8 Ma
Y map
Th map

Figure 8

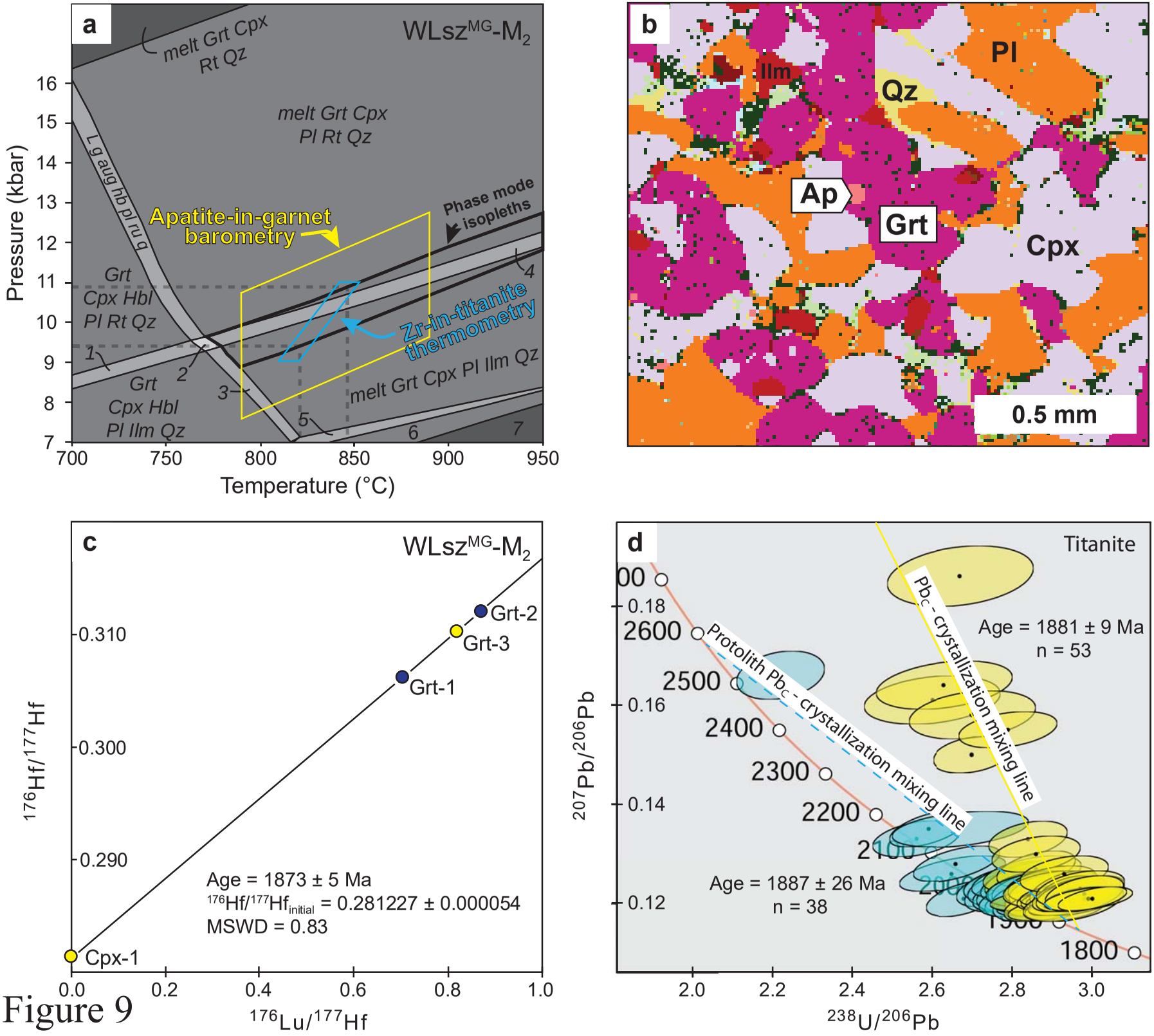
a
WLsz^MG-M2
melt Grt Cpx
Rt Qz
melt Grt Cpx
Pl Rt Qz
L g aug hb pl ru g
Apatite-in-garnet
barometry
Phase mode
isopleths
Zr-in-titanite
thermometry
Grt
Cpx Hbl
Pl Rt Qz
Grt
Cpx Hbl
Pl Ilm Qz
melt Grt Cpx Pl Ilm Qz
1
2
3
4
5
6
7
Pressure (kbar)
Temperature (°C)
b
Ilm
Qz
Pl
Ap
Grt
Cpx
0.5 mm
c
WLsz^MG-M2
Grt-2
Grt-3
Grt-1
Cpx-1
Age = 1873 ± 5 Ma
176Hf/177Hf initial = 0.281227 ± 0.000054
MSWD = 0.83
176Hf/177Hf
176Lu/177Hf
d
Titanite
Pbc - crystallization mixing line
Age = 1881 ± 9 Ma
n = 53
Protolith Pbc - crystallization mixing line
Age = 1887 ± 26 Ma
n = 38
207Pb/206Pb
238U/206Pb

Figure 9

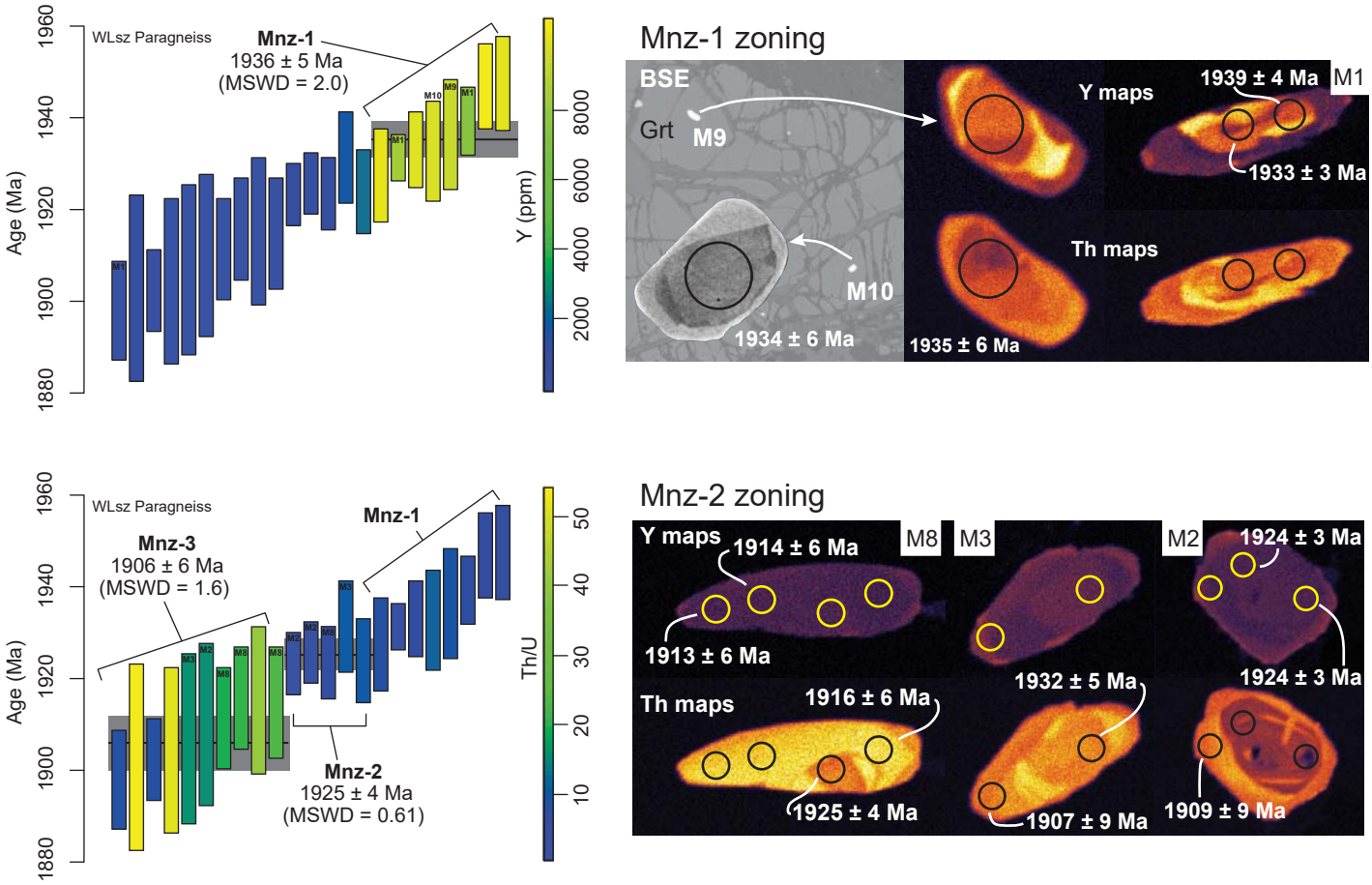
WLsz Paragneiss
Mnz-1
1936 ± 5 Ma
(MSWD = 2.0)
Age (Ma)
1960
1940
1920
1900
1880
Y (ppm)
8000
6000
4000
2000
Mnz-1 zoning
BSE
Grt
M9
M10
1934 ± 6 Ma
Y maps
1939 ± 4 Ma
M1
1933 ± 3 Ma
Th maps
1935 ± 6 Ma
WLsz Paragneiss
Mnz-3
1906 ± 6 Ma
(MSWD = 1.6)
Mnz-1
Mnz-2
1925 ± 4 Ma
(MSWD = 0.61)
Th/U
50
40
30
20
10
Mnz-2 zoning
Y maps
1914 ± 6 Ma
M8
M3
M2
1924 ± 3 Ma
1913 ± 6 Ma
Th maps
1916 ± 6 Ma
1932 ± 5 Ma
1924 ± 3 Ma
1925 ± 4 Ma
1907 ± 9 Ma
1909 ± 9 Ma

Figure 10

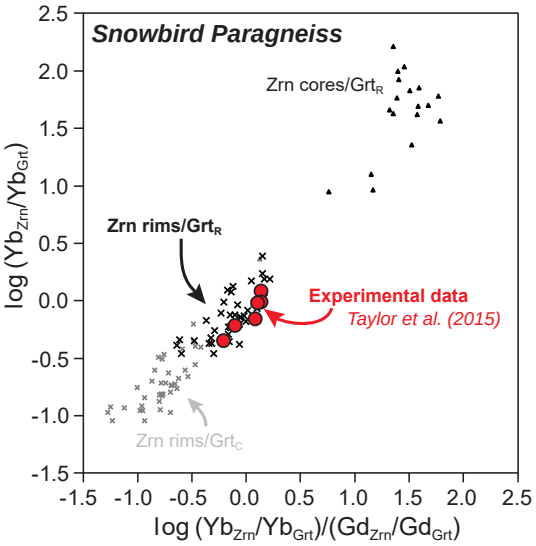
Snowbird Paragneiss
Zrn cores/Grt$_R$
Zrn rims/Grt$_R$
Experimental data
Taylor et al. (2015)
Zrn rims/Grt$_C$
log (Yb$_{Zrn}$/Yb$_{Grt}$)
log (Yb$_{Zrn}$/Yb$_{Grt}$)/(Gd$_{Zrn}$/Gd$_{Grt}$)
2.5
2.0
1.5
1.0
0.5
0.0
-0.5
-1.0
-1.5
-1.5 -1.0 -0.5 0.0 0.5 1.0 1.5 2.0 2.5

Figure 11

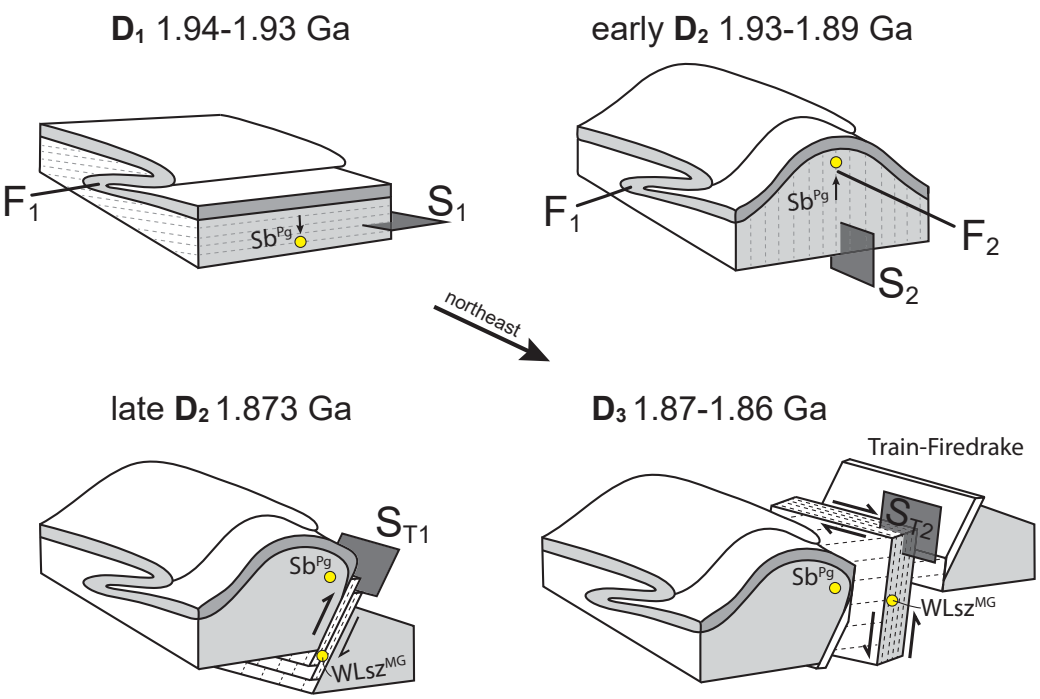
D1 1.94-1.93 Ga
early D2 1.93-1.89 Ga
F1
S1
SbPg
F1
SbPg
F2
S2
northeast
late D2 1.873 Ga
D3 1.87-1.86 Ga
ST1
SbPg
WLszMG
Train-Firedrake
ST2
SbPg
WLszMG

Figure 12

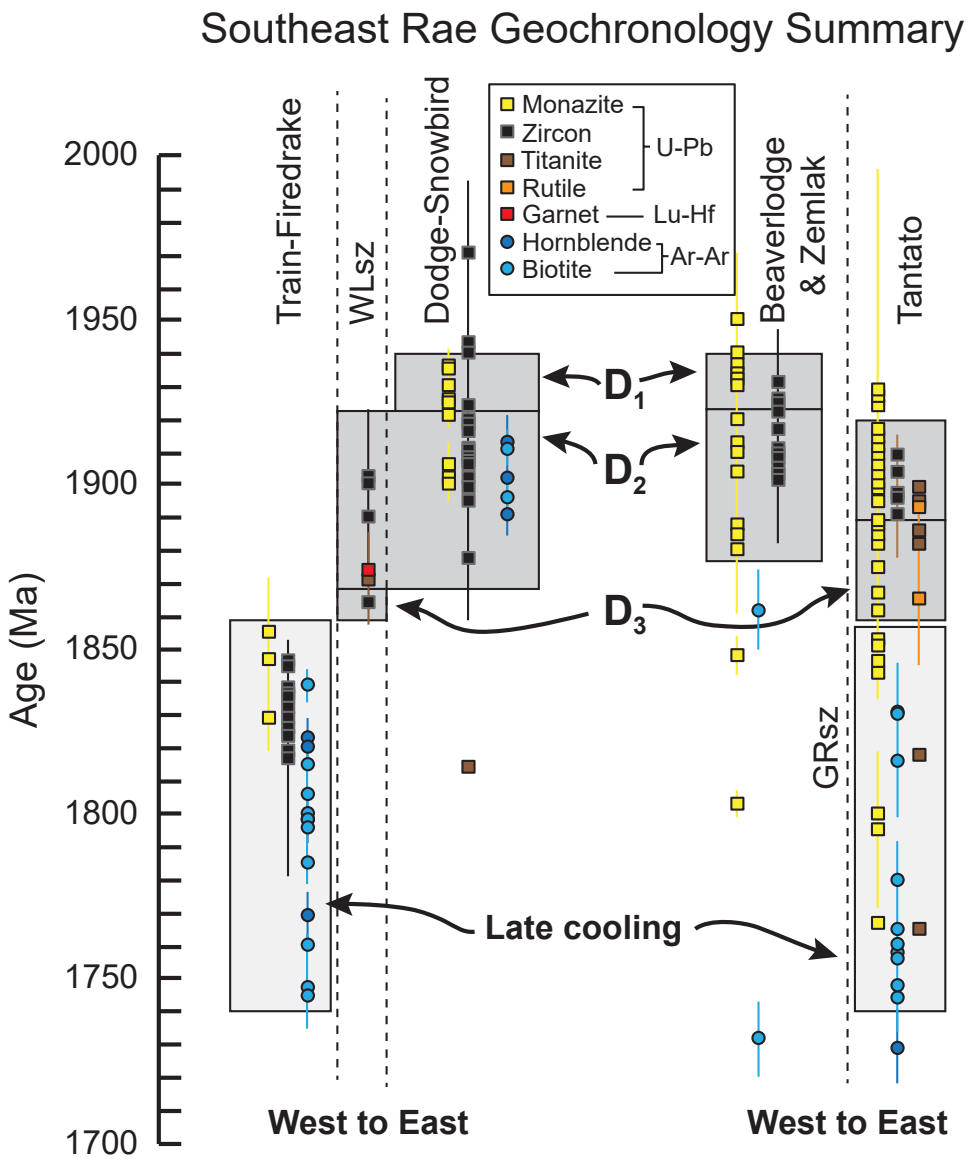
Southeast Rae Geochronology Summary
Age (Ma)
2000
1950
1900
1850
1800
1750
1700
Train-Firedrake
WLsz
Dodge-Snowbird
Beaverlodge & Zemlak
GRsz
Tantato
Monazite
Zircon
Titanite
Rutile
U-Pb
Garnet
Lu-Hf
Hornblende
Biotite
Ar-Ar
D1
D2
D3
Late cooling
West to East
West to East

Figure 13

SUPPORTING FIGURES

Monazite textural locations and elemental maps

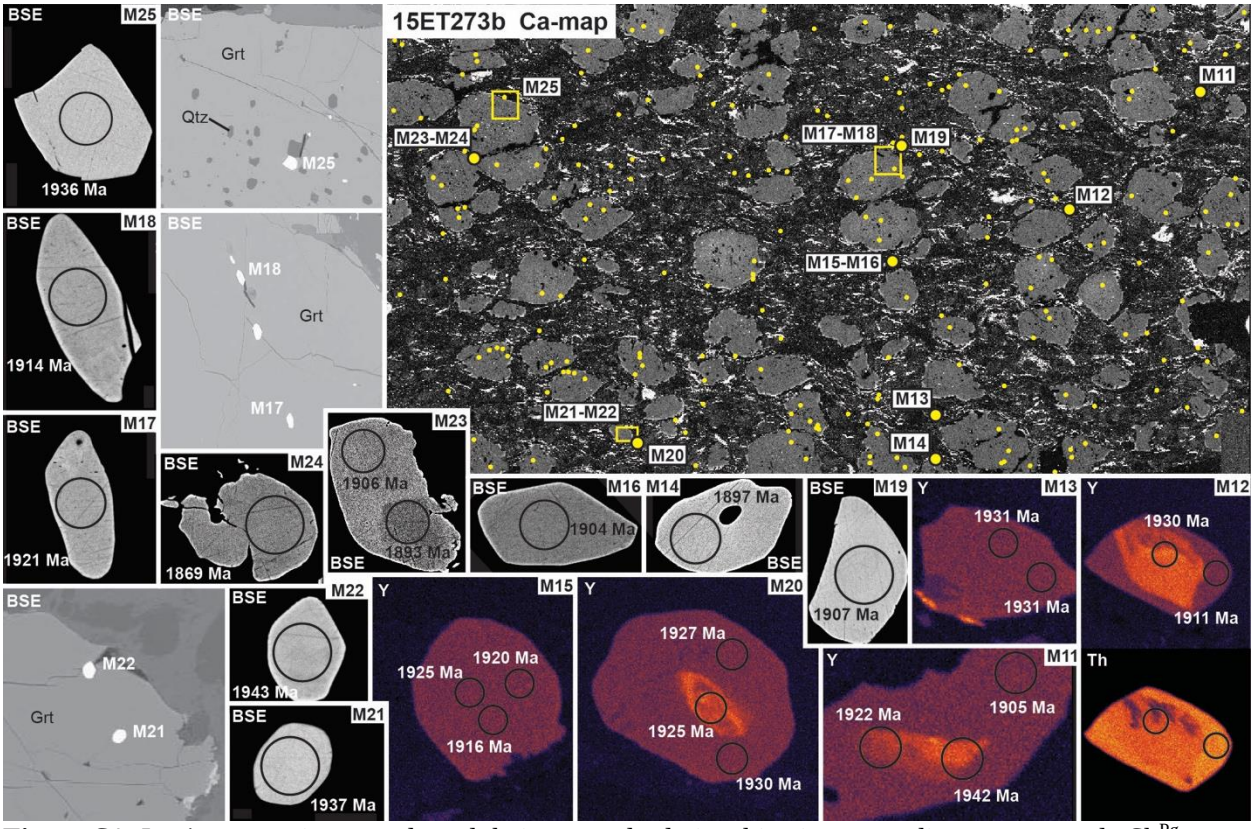

Figure S1. *In-situ* monazite crystals and their textural relationships in metasedimentary sample Sb^{Pg} (15ET273b) analyzed by U-Pb SHRIMP. Calcium elemental base map (upper right) of thin section shows monazite locations (yellow small circles) and analyzed monazite locations (large yellow circles). Yellow boxes outline areas with monazite encased in garnet that are shown on the left as BSE images. BSE and trace element monazite maps show the corresponding dates with textual location. Spot size (black circles) is 10 μm in diameter.

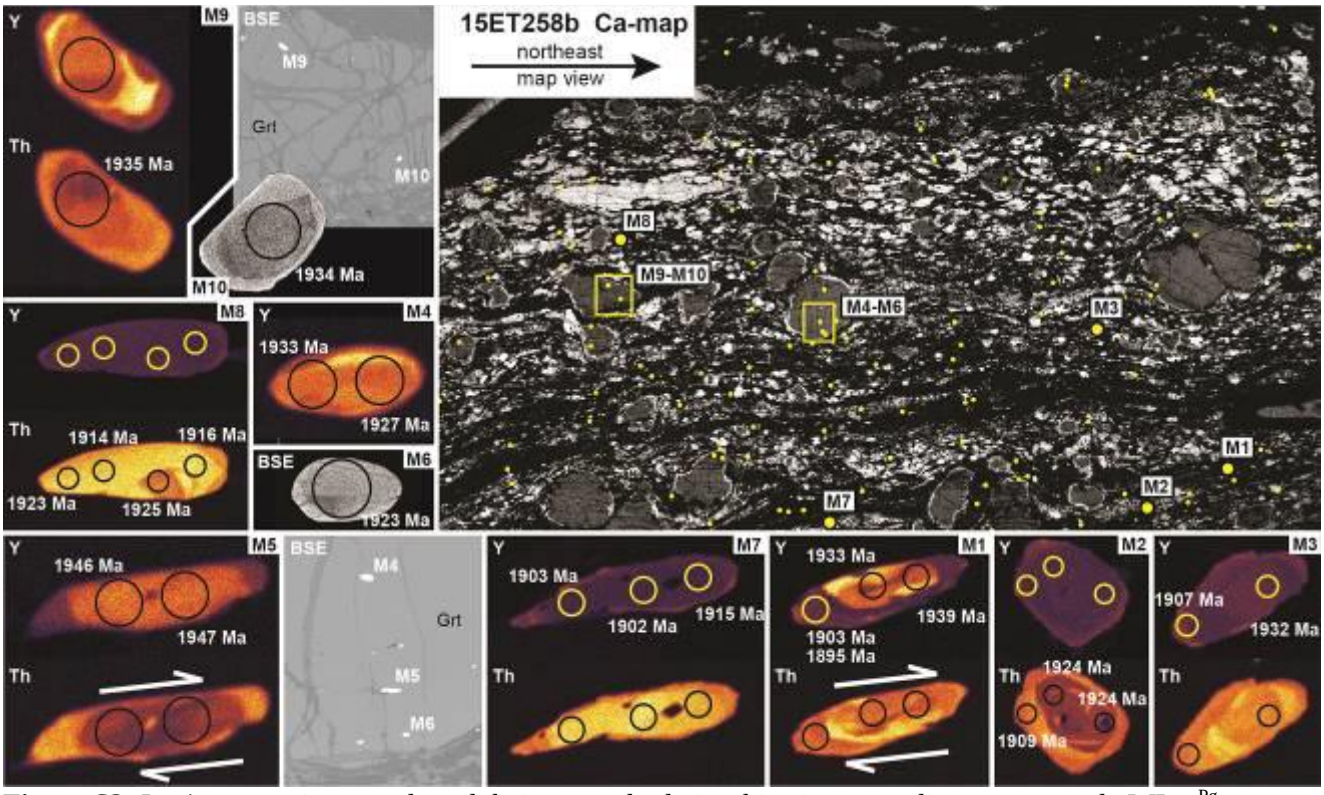

Figure S2. *In-situ* monazite crystals and their textural relationships in metasedimentary sample WLsz^{Pg} (15ET258b) analyzed by U-Pb SHRIMP. Calcium elemental base map (upper right) of thin section shows monazite locations (yellow small circles) and analyzed monazite locations (large yellow circles). Yellow boxes outline areas with monazite encased in garnet that are shown on the left as BSE images. BSE and trace element monazite maps show the corresponding dates with textural location. Spot size (black circles) is 10 μm in diameter. Note that many matrix crystals have elongate morphologies parallel with the primary S_{T2} tectonic foliation in the Wholdaia Lake shear zone and show apparent dextral kinematics, however, these crystals were likely transposed into the S_{T2} foliation (see main text). Therefore, the apparent dextral growth of some rim domains (M1, M5) likely represent modification by a later deformation and do not represent the age for S_{T2}.

Supplementary pseudosection for WLsz^{MG}-M$_2$

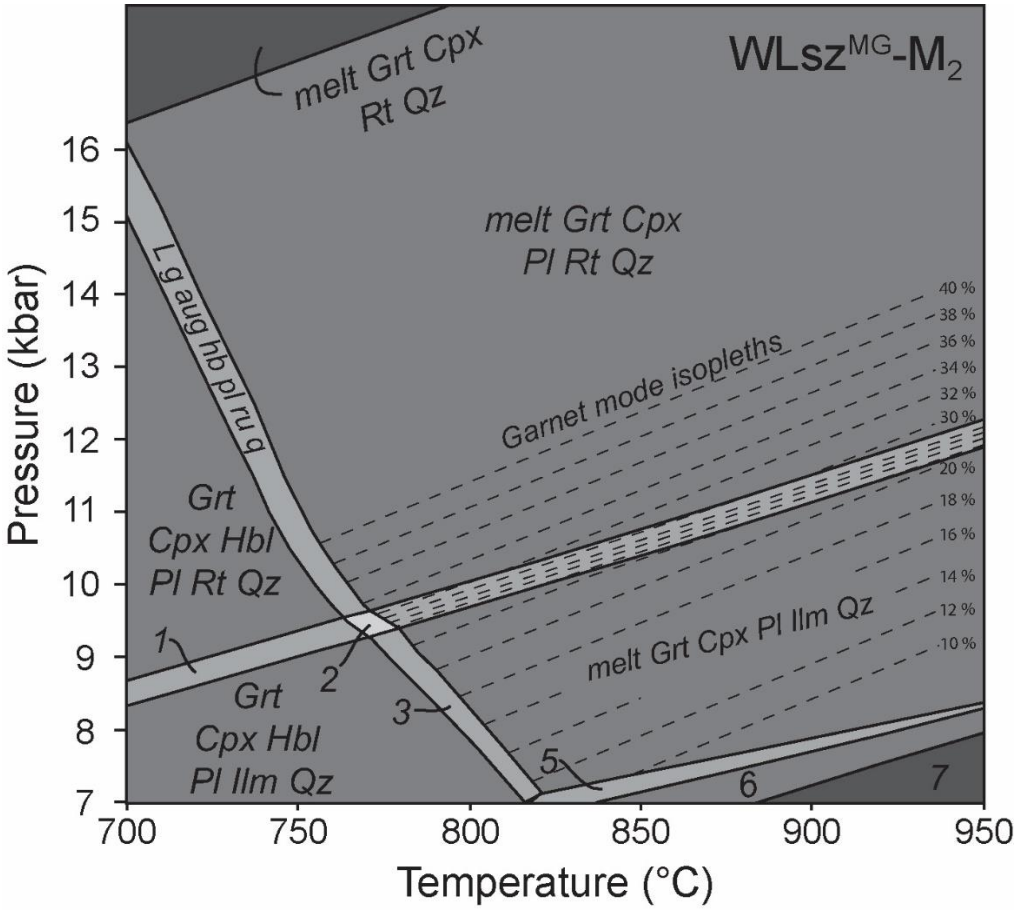

Figure S3. Pseudosection for the WLsz^{MG}-M$_2$ assemblage from Figure 9a. Garnet mode isopleths are plotted to illustrate that an increase in pressure is required to generate additional garnet.

Supplementary Table 1. South Rae Age Compilation

Lat. (N)	Long. (W)	Domain	Sample_ID	Reference	Type	Age	Err
63.34717	-94.73036	Firedrake	15EM71b	Regis and Kellett 2018	Bt Ar-Ar	1839	5
63.89812	-93.13117	Firedrake	PQB-50d-2012	Regis and Kellett 2018	Bt Ar-Ar	1815	6
59.31890	-107.05055	Firedrake	PQB-84-2012	Regis and Kellett 2018	Bt Ar-Ar	1806	5
59.31890	-107.05055	Firedrake	DR1013A	Regis and Kellett 2018	Bt Ar-Ar	1800	0
59.31890	-107.05055	Firedrake	12PQB47	Regis and Kellett 2018	Bt Ar-Ar	1798	7
59.33205	-106.96747	Firedrake	12PQB91	Regis and Kellett 2018	Bt Ar-Ar	1796	7
59.31607	-106.78352	Firedrake	PQB-81B-2012	Regis and Kellett 2018	Bt Ar-Ar	1795	6
59.31620	-106.28110	Firedrake	12PQB41	Regis and Kellett 2018	Bt Ar-Ar	1785	0
59.31620	-106.28110	Firedrake	12PBA63	Regis and Kellett 2018	Bt Ar-Ar	1785	7
59.29360	-106.55153	Firedrake	12PQB40	Regis and Kellett 2018	Bt Ar-Ar	1760	0
59.32019	-105.28170	Firedrake	ET265A	Regis and Kellett 2018	Bt Ar-Ar	1745	7
		Firedrake	03M92	Flowers et al 2006b	Ms Ar-Ar	1747	12
59.44023	-105.15812	Firedrake	12PQB39	Regis and Kellett 2018	Hbl Ar-Ar	1823	6
59.41249	-105.25407	Firedrake	PQB-84-2012	Regis and Kellett 2018	Hbl Ar-Ar	1820	6
59.32500	-105.33000	Firedrake	12PQB47	Regis and Kellett 2018	Hbl Ar-Ar	1798	7
59.42379	-105.19796	Firedrake	ET265A	Regis and Kellett 2018	Hbl Ar-Ar	1769	7
59.31000	-105.39000	Firedrake	J592	Berman et al 2013	Mnz SHRIMP	1855	17
59.33300	-105.98000	Firedrake	T902	Berman et al 2013	Mnz SHRIMP	1847	14
59.40000	-105.39000	Firedrake	J592	Berman et al 2013	Mnz SHRIMP	1829	10
59.41249	-105.25407	Firedrake	10842	Davis et al 2015	Zrn SHRIMP	1838	6
59.41000	-104.94000	Firedrake	10931	Davis et al 2015	Zrn SHRIMP	1837	6
59.55000	-106.03000	Firedrake	10851	Davis et al 2015	Zrn SHRIMP	1836	5
59.40000	-105.12500	Firedrake	10674	Davis et al 2015	Zrn SHRIMP	1832	6
59.40000	-105.39000	Firedrake	10926	Davis et al 2015	Zrn SHRIMP	1829	2
59.43399	-108.10831	Firedrake	10939	Davis et al 2015	Zrn SHRIMP	1829	11
59.39415	-107.80083	Firedrake	10938	Davis et al 2015	Zrn SHRIMP	1819	4
59.39135	-107.45248	Firedrake	10932	Davis et al 2015	Zrn SHRIMP	1817	36
59.39415	-107.80083	Firedrake	15EM81A	Regis et al 2017b OF	Zrn SHRIMP	1846	5
59.39135	-107.45248	Firedrake	15PA320	Thiessen Unpublished	Zrn SHRIMP	1845	5
59.39959	-107.51255	Firedrake	15PA320	Thiessen Unpublished	Zrn SHRIMP	1845	5
59.41527	-107.70855	Firedrake	15EM71A	Regis et al 2017b OF	Zrn SHRIMP	1826	4
59.39135	-107.45248	Firedrake	15EM80B	Regis et al 2017b OF	Zrn SHRIMP	1824	4
60.59615	-104.12553	WLsz	15EM68a	Regis et al 2017b OF	Zrn SHRIMP	1902	10
60.99803	-103.54329	WLsz	15EM68b	Thiessen et al 2018	Zrn SHRIMP	1901	8

60.59615	-104.12553	WLsz	15ET249	Thiessen et al 2018	Zrn SHRIMP	1890	33
60.99803	-103.54329	WLsz	15ET260d	Thiessen et al 2018	Zrn SHRIMP	1871	5
60.59615	-104.12553	WLsz	15ET253a	Thiessen et al 2018	Zrn SHRIMP	1864	2
60.59615	-104.12553	WLsz	15ET249	Thiessen et al 2019	Grt Lu-Hf	1873	5
60.59615	-104.12553	WLsz	15ET249	Thiessen et al 2019	Ttn LAICPMS	1871	14
60.46712	-103.85271	Snowbird	EM264A	Regis and Kellett 2018	Bt Ar-Ar	1911	7
63.85270	-92.68850	Snowbird	DW616A	Regis and Kellett 2018	Bt Ar-Ar	1896	7
63.85270	-92.68850	Snowbird	DW680A	Regis and Kellett 2018	Hbl Ar-Ar	1913	8
63.85970	-92.71670	Snowbird	DW616A	Regis and Kellett 2018	Hbl Ar-Ar	1902	7
63.85970	-92.71670	Snowbird	EM264A	Regis and Kellett 2018	Hbl Ar-Ar	1891	7
59.57302	-105.37583	Snowbird	07w-032	Williams and Jercinovic 2012	Mnz EMP	1930	10
59.41976	-105.47881	Snowbird	07w-032	Williams and Jercinovic 2012	Mnz EMP	1900	5
59.45481	-105.45388	Snowbird	1a	Martel et al 2008	Mnz SHRIMP	1921	4
59.40348	-105.53191	Snowbird	1b	Martel et al 2008	Mnz SHRIMP	1921	4
59.39791	-105.47976	Snowbird	1a	Martel et al 2008	Mnz SHRIMP	1904	9
59.57938	-105.33343	Snowbird	1b	Martel et al 2008	Mnz SHRIMP	1904	9
59.41976	-105.47881	Snowbird	15ET258b	This Study	Mnz SHRIMP	1936	5
59.40348	-105.53191	Snowbird	15ET273b	This Study	Mnz SHRIMP	1935	5
59.57938	-105.33343	Snowbird	15ET273b	This Study	Mnz SHRIMP	1926	5
59.45481	-105.45388	Snowbird	15ET258b	This Study	Mnz SHRIMP	1925	4
59.55666	-105.81615	Snowbird	15ET258b	This Study	Mnz SHRIMP	1906	4
59.56359	-105.81588	Snowbird	15ET273b	This Study	Mnz SHRIMP	1902	6
59.48810	-105.96008	Snowbird	8	Martel et al 2008	Zrn SHRIMP	1918	5
59.48810	-105.96008	Snowbird	6	Martel et al 2008	Zrn SHRIMP	1911	12
59.48810	-105.96008	Snowbird	1c	Martel et al 2008	Zrn SHRIMP	1910	7
59.48810	-105.96008	Snowbird	11592	Regis et al 2017a	Zrn SHRIMP	1943	7
59.48810	-105.96008	Snowbird	11591	Regis et al 2017a	Zrn SHRIMP	1907	9
59.48810	-105.96008	Snowbird	15ET273b	This Study	Zrn SHRIMP	1920	6
59.48391	-108.39644	Dodge	13R-005	Regan et al 2017a rae-hearne	Zrn LAICPMS	1916	4
59.45728	-108.07198	Dodge	13R-029	Regan et al 2017a rae-hearne	Zrn LAICPMS	1902	14
59.49062	-108.25612	Dodge	11BK-098	Ashton et al 2017a	Zrn SHRIMP	1970	22
59.35167	-106.01861	Dodge	11BK-098	Ashton et al 2017a	Zrn SHRIMP	1940	12
60.66920	-106.61841	Dodge	09BK-352	Ashton et al 2017a	Zrn SHRIMP	1924	11
60.94539	-104.08156	Dodge	11BK-097	Ashton et al 2017a	Zrn SHRIMP	1908	5
60.31409	-106.93676	Dodge	BK10-481	Ashton et al 2017a	Zrn SHRIMP	1906	21
62.38610	-102.68900	Dodge	09BK-491	Ashton et al 2017a	Zrn SHRIMP	1899	6

60.89195	-104.90661	Dodge	09BK-352	Ashton et al 2017a	Zrn SHRIMP	1878	19
61.13922	-104.78131	Dodge	10309	Regis et al 2017a	Zrn SHRIMP	1906	21
61.19469	-104.25813	Dodge	10311	Regis et al 2017a	Zrn SHRIMP	1895	7
61.19193	-105.53528	Dodge	BK10-008	Regis et al., 2017 (OF8254)	Zrn SHRIMP	1895	7
63.93580	-93.89082	Dodge	10311	Regis et al., 2017 (OF8254)	Zrn SHRIMP	1895	7
59.89705	-104.98107	Beaverlodge	96W-19b	Williams et al 1999	Mnz EMP	1880	20
59.78657	-105.18726	Beaverlodge	99W-19bM15	Williams and Jercinovic 2002	Mnz EMP	1910	10
59.89057	-105.12555	Beaverlodge	99W-19bM20	Williams and Jercinovic 2002	Mnz EMP	1888	4
59.37544	-105.91059	Beaverlodge	99W-19bM15	Williams and Jercinovic 2002	Mnz EMP	1848	6
59.37000	-105.94000	Beaverlodge	99W-19bM15	Williams and Jercinovic 2002	Mnz EMP	1803	4
59.37544	-105.91059	Beaverlodge	B063	Bethune et al 2013	Mnz SHRIMP	1939	6
59.37544	-105.91059	Beaverlodge	B079d	Bethune et al 2013	Mnz SHRIMP	1938	8
62.34687	-99.77054	Beaverlodge	B016	Bethune et al 2013	Mnz SHRIMP	1936	10
64.14866	-88.89973	Beaverlodge	B010ab	Bethune et al 2013	Mnz SHRIMP	1933	8
63.94008	-90.86219	Beaverlodge	B016	Bethune et al 2013	Mnz SHRIMP	1932	16
63.56371	-92.33042	Beaverlodge	B002e	Bethune et al 2013	Mnz SHRIMP	1931	11
63.32900	-92.57965	Beaverlodge	B079d	Bethune et al 2013	Mnz SHRIMP	1913	14
63.65072	-91.32785	Beaverlodge	B010ab	Bethune et al 2013	Mnz SHRIMP	1904	8
63.33433	-95.13834	Beaverlodge	RH98-542	Hartlaub et al 2004	Mnz TIMS	1950	20
63.46265	-94.25241	Beaverlodge	4706-0569	Ashton et al 2007b	Zrn SHRIMP	1909	16
63.10719	-91.23984	Beaverlodge	4706-0644	Ashton et al 2007b	Zrn SHRIMP	1907	5
63.02474	-90.96851	Beaverlodge	4700-4541	Ashton et al 2009b	Zrn SHRIMP	1911	10
63.97676	-93.73140	Beaverlodge	RH98-521	Ashton et al 2009b	Zrn SHRIMP	1905	3
59.43262	-108.10986	Beaverlodge	RH98-780	Ashton et al 2009b	Zrn SHRIMP	1903	2
59.45728	-108.07198	Beaverlodge	4707-0210	Ashton et al 2009c	Zrn SHRIMP	1902	20
59.48130	-108.29540	Beaverlodge	4706-0327	Ashton et al 2014	Zrn SHRIMP	1924	23
59.49062	-108.25612	Beaverlodge	4706-7015	Ashton et al 2014	Zrn SHRIMP	1905	8
		Beaverlodge	96W23E	Flowers et al 2006b	Bt Ar-Ar	1862	12
		Beaverlodge	99B-87	Flowers et al 2006b	Ms Ar-Ar	1732	12
59.39727	-107.60288	Zemlak	4701-8025	Ashton 2009 map	Mnz SHRIMP	1940	20
59.39727	-107.60288	Zemlak	4705-0016d	Ashton 2009 map	Mnz SHRIMP	1930	7
60.33860	-103.42886	Zemlak	4704-0647	Ashton 2009 map	Mnz SHRIMP	1920	11
60.33860	-103.42886	Zemlak	4705-0016d	Ashton 2009 map	Mnz SHRIMP	1920	11
59.42258	-107.60354	Zemlak	4704-0647	Ashton 2009 map	Mnz SHRIMP	1885	14
59.42258	-107.60354	Zemlak	4705-0556	Ashton et al 2007a	Zrn SHRIMP	1925	10
59.42259	-107.62174	Zemlak	4703-0007	Ashton et al 2007a	Zrn SHRIMP	1922	16

59.42259	-107.62174	Zemlak	4700-0320	Ashton et al 2009b	Zrn SHRIMP	1908	1
59.42259	-107.62174	Zemlak	4704-0716	Ashton et al 2009c	Zrn SHRIMP	1931	10
59.42259	-107.62174	Zemlak	14KA-095	Shiels et al 2016	Zrn LA-ICPMS	1917	15
60.52687	-103.25429	Tantato	04G-019b	Dumond et al 2008	Mnz EMP	1910	10
60.89809	-103.34229	Tantato	04G-019b	Dumond et al 2008	Mnz EMP	1846	8
60.46122	-103.72407	Tantato	04G-019b	Dumond et al 2008	Mnz EMP	1800	0
60.46122	-103.72407	Tantato	04G-050b	Dumond et al 2010	Mnz EMP	1906	8
60.89809	-103.34229	Tantato	04G-067	Dumond et al 2010	Mnz EMP	1897	9
61.25853	-105.66877	Tantato	05g-026b	Dumond et al 2015	Mnz EMP	1924	72
61.04085	-105.32686	Tantato	05g-019b	Dumond et al 2015	Mnz EMP	1913	25
60.53435	-105.75241	Tantato	04g-097	Dumond et al 2015	Mnz EMP	1897	11
61.32986	-102.04646	Chipman domain	03M166B	Mahan et al 2006a	Mnz EMP	1915	25
61.25853	-105.66877	Chipman domain	02M129E	Mahan et al 2006a	Mnz EMP	1909	24
61.15312	-104.69874	Chipman domain	S32D	Mahan et al 2006a	Mnz EMP	1900	15
60.31397	-106.93577	Chipman domain	S32D	Mahan et al 2006a	Mnz EMP	1853	15
60.70231	-106.29242	Chipman domain	03M166B	Mahan et al 2006a	Mnz EMP	1851	9
60.31397	-106.93577	Chipman domain	02M194B	Mahan et al 2006b	Mnz EMP	1929	32
61.78757	-105.30954	Chipman domain	01M171D	Mahan et al 2006b	Mnz EMP	1902	23
60.18471	-105.25899	Chipman domain	02M66G	Mahan et al 2006b	Mnz EMP	1889	14
60.18471	-105.25899	Chipman domain	01M171D	Mahan et al 2006b	Mnz EMP	1843	10
60.49656	-106.28057	Chipman domain	01M171D	Mahan et al 2006b	Mnz EMP	1795	14
61.12377	-105.62723	Chipman domain	02M194B	Mahan et al 2006b	Mnz EMP	1795	24
60.98518	-104.95314	Chipman domain	01M127B	Mahan et al 2006b	Mnz EMP	1767	2
60.59805	-104.75682	Tantato	12R-054	Regan et al 2014	Mnz EMP	1917	12
60.09587	-105.75462	Tantato	10W-098a	Regan et al 2014	Mnz EMP	1916	12
61.13908	-104.78042	Tantato	11R-028b	Regan et al 2014	Mnz EMP	1906	7
60.09587	-105.75462	Tantato	10W-110	Regan et al 2014	Mnz EMP	1903	3
60.25561	-104.48777	Tantato	10W-094g	Regan et al 2014	Mnz EMP	1899	4
60.25763	-104.52558	Tantato	12R-057c	Regan et al 2014	Mnz EMP	1895	3
59.89708	-104.96640	Tantato	10W-098a	Regan et al 2014	Mnz EMP	1888	6
59.93486	-105.03815	Tantato	10W-110	Regan et al 2014	Mnz EMP	1885	11
60.39023	-104.63506	Tantato	12R-057c	Regan et al 2014	Mnz EMP	1882	5
60.07154	-107.25414	Tantato	11R-028b	Regan et al 2014	Mnz EMP	1875	6
60.71545	-106.09108	Tantato	11G020	Regan et al 2017b	Mnz EMP	1929	8
60.71545	-106.09108	Tantato	11G020	Regan et al 2017b	Mnz EMP	1927	5
60.53367	-105.75435	Tantato	11G020	Regan et al 2017b	Mnz EMP	1900	24

60.86391	-104.86457	Tantato	11G020	Regan et al 2017b	Mnz EMP	1899	4
63.72964	-93.97218	Tantato	11G020	Regan et al 2017b	Mnz EMP	1867	10
63.68117	-93.85529	Tantato	11G020	Regan et al 2017b	Mnz EMP	1862	7
63.67452	-94.10499	Tantato	PCA-S207	Bracciali et al., 2013	Rt TIMS	1865	8
63.72964	-93.97218	Tantato	01SZ40B	Baldwin et al 2004	Rt TIMS	1865	20
63.63832	-94.10489	Tantato	02-281	Flowers et al 2006b	Rt TIMS	1893	8
63.97534	-93.96426	Tantato	SZ00-188c	Baldwin et al 2003	Ttn TIMS	1899	2
59.93487	-105.03815	Chipman domain	SZ00-196c	Flowers et al 2006b	Ttn TIMS	1895	4
59.93486	-105.03815	Chipman domain	02-M133A	Flowers et al 2006b	Ttn TIMS	1886	2
64.11000	-93.89000	Chipman domain	03-52	Flowers et al 2006b	Ttn TIMS	1882	2
64.00000	-93.80000	Chipman domain	02M45	Flowers et al 2006b	Ttn TIMS	1818	3
		Tantato	SZ00-118c	Flowers et al 2006b	Ttn TIMS	1899	
64.20000	-94.50000	Dodge	99B-74	Flowers et al 2006b	Ttn TIMS	1814	3
64.20000	-94.50000	LLsz	M144	Flowers et al 2006b	Ttn TIMS	1765	25
64.11000	-93.89000	Tantato	01SZ41A	Baldwin et al 2003	Zr TIMS	1904	1
59.50440	-108.76951	Tantato	01SZ40B	Baldwin et al 2004	Zr TIMS	1909	6
60.39023	-104.63506	Chipman domain	02-97	Flowers et al 2006a	Zr TIMS	1897	1
60.72260	-104.01793	Chipman domain	02-58	Flowers et al 2006a	Zr TIMS	1896	1
60.87748	-103.98060	Chipman domain	03-52	Flowers et al 2006a	Zr TIMS	1896	1
60.72661	-104.18307	Chipman domain	02-88	Flowers et al 2006a	Zr TIMS	1896	1
60.99803	-103.54329	Chipman domain	02-76B	Flowers et al 2006a	Zr TIMS	1891	1
60.59615	-104.12553	Chipman domain	02-M133A	Flowers et al 2008	Zr TIMS	1896	18
		Tantato	03-196A	Flowers et al 2006b	Bt Ar-Ar	1760	12
		Tantato	03-109A	Flowers et al 2006b	Bt Ar-Ar	1756	12
		Tantato	01SZ122B	Flowers et al 2006b	Bt Ar-Ar	1816	17
		Tantato	01SZ78	Flowers et al 2006b	Bt Ar-Ar	1831	15
59.48130	-108.29540	Chipman domain	PQB-22B-2012	Regis and Kellett 2018	Bt Ar-Ar	1830	6
		Chipman domain	0276B	Flowers et al 2006b	Bt Ar-Ar	1780	12
		Chipman domain	03-169E	Flowers et al 2006b	Bt Ar-Ar	1765	12
		Chipman domain	02-77B	Flowers et al 2006b	Bt Ar-Ar	1748	12
		Chipman domain	02-108B	Flowers et al 2006b	Bt Ar-Ar	1744	12
		Chipman domain	02-183D	Flowers et al 2006b	Ms Ar-Ar	1758	12
		Chipman domain	01M123C	Flowers et al 2006b	Hbl Ar-Ar	1729	11